Jet quenching in Quark Gluon Plasma: flavor tomography at RHIC and LHC by the CUJET model

Alessandro Buzzatti

Submitted in partial fulfillment of the
requirements for the degree of
Doctor of Philosophy
in the Graduate School of Arts and Sciences

Columbia University

2013

Abstract

Jet quenching in Quark Gluon Plasma: flavor tomography at RHIC and LHC by the CUJET model

Alessandro Buzzatti

A new jet tomographic model and numerical code, CUJET, is developed in this thesis and applied to the phenomenological study of the Quark Gluon Plasma produced in Heavy Ion Collisions.

Contents

List of Figures

Acknowledgments

I would like to thank my advisor, Prof. Miklos Gyulassy, for the support, advice and encouragement that I received during these long and exciting years of doctoral research at Columbia University. Your teaching and experience were invaluable: the path from student to scientist, although strenuous and far from complete, would have been impracticable without your guidance and help.

This work would have not been possible without the support of the DOE Grant No. DE-FG02-93ER40764 and of the Jet Collaboration: thank you to Xin-Nian Wang as director of the project.

Also thank you to all the members of the nuclear theory group at Columbia, starting from Jorge Noronha, Barbara Betz, Giorgio Torrieri, Mohammed Mia and William Horowitz, for your friendship and helpful physics discussions.

Finally, thank you to John Harris (Yale University), Bill Zajc and Brian Cole (Columbia University), for your help and recommendations.

My nearly five years of doctorate at Columbia University, however, would have been rather insignificant if I did not have a chance to live New York City at its fullest, or without the company of some of my best friends: Andrej Ficnar, Chris Gutiérrez, Nikiforos Nikiforou. Knowing someone to have fun with is relatively easy, but meeting friends who one can count on 'no-matter-what' is a rare event. I was triply lucky, and for this you guys deserve all my gratitude, especially you, Andrej.

My sister and my parents merit a special mention. It is surprising how I unconsciously rely on their teachings (Mamma e Papà), example (Giulia), and judgment (all): thank you for pointing me always in the right direction. And thank you also for your total, unconditional support received throughout these years, accompanied by full trust and firm belief in all my choices.

At last, Kate. You supported me, helped me, and tolerated me during the arguably most crucial phase of my doctorate. One of the reasons I am still here, and I am happy, is you.

Al Nonno e New York, who never met.

Outline

This work was performed at Columbia University as part of a five year DOE Topical Collaboration Project [30] on jet and electromagnetic tomography of extreme phases of matter in heavy-ion collisions.

A new jet tomographic model and numerical code, CUJET, is developed in this thesis and applied to the phenomenological study of the Quark Gluon Plasma (QGP) produced in Heavy Ion Collisions.

The new CUJET code features:

- jet interaction potentials that can interpolate between the dynamical and static limits;
- the ability to calculate high order in opacity corrections to interpolate numerically between the 'thin' and 'thick' plasma approximations;
- full jet path proper time integration over longitudinally expanding and transverse diffuse QGP geometries;

- the ability to evaluate systematic theoretical uncertainties such as sensitivity to formation and decoupling phases of the QGP evolution, local running coupling and screening scale variations, and other effects out of reach with analytic approximations;

- the inclusion of elastic, in addition to radiative, fluctuating energy loss distributions;

- convolution over collision energy and flavor dependent invariant jet spectral densities;

- convolution over final fragmentation functions.

In Chapter 1, we present an introduction to the subject of Quark Gluon Plasma, explaining its evolution from creation to hadronization, with particular attention to the underlying fundamental theory of Quantum Chromo-Dynamics.

In Chapter 2, we review some of the approximate jet energy loss models, with particular attention to the opacity series expansion of (D)GLV.

In Chapter 3, we show the first results of our CUJET Monte Carlo algorithm, applied to the study of the induced radiation spectrum.

In Chapter 4, further improvements over the DGLV energy loss model are introduced, such as the inclusion of (1) dynamical magnetic effects, (2) elastic energy loss, (3) full jet path integration, and especially (4) running of the QCD coupling constant.

In Chapter 5, the CUJET model is constructed, paying attention to all the stages of jet quenching (initial conditions, plasma evolution, energy loss, fragmentation), as well as the systematic uncertainties that affect the model.

In Chapter 6[1], results published in [31, 32, 33, 34] are reported: the CUJET predictions of the nuclear modification factor are compared to recent data obtained at the Relativistic Heavy Ion Collider (RHIC) and the Large Hadron Collider (LHC).

We summarize the work of this thesis in the Conclusions.

[1]The results are presented in a self-consistent fashion, and do not require the reading of any previous Chapter.

Chapter 1

Introduction

1.1 Quantum ChromoDynamics

1.1.1 History

Our thesis begins with a plot, the QCD phase diagram of Fig. 1.1.

The search for the quark gluon plasma and the ongoing effort to characterize its properties, after all, constitute only one part in a broader and more ambitious attempt to understand how nuclear matter behaves at the level of its most fundamental constituents.

This investigation started nearly sixty years ago, with the development of the bubble chamber [35] and the discovery of a vast population of hadrons which soon suggested the presence of a more fundamental constituent of ordinary matter. The first attempts to categorize and find a logic in the observed spectrum of new particles led to the elaboration, in the early 60's,

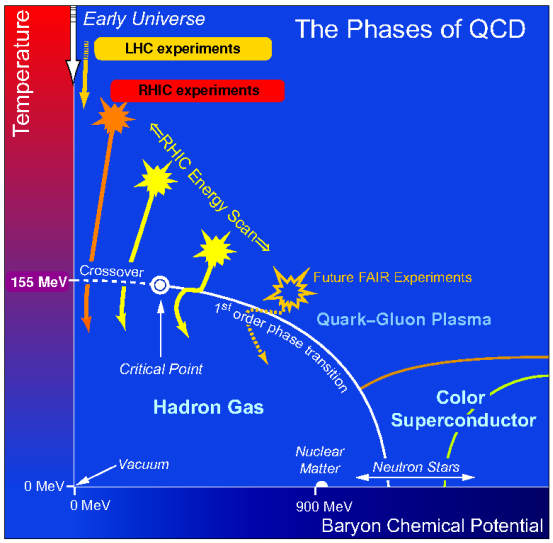

Figure 1.1: Phase diagram of QCD, represented in the baryochemical potential and temperature plane. Heavy ion collision experiments at RHIC and LHC are shown to probe the crossover and near critical-point region of the transition between a hadron gas and quark gluon plasma. Taken from NSAC report, 2007.

of the *eightfold way* [36, 37].

Proposing a symmetry scheme analogous to the then-known isospin symmetry, Gell-Mann and Ne'eman associated the hadrons with specific representations of the group $SU(3)$: baryons were octets and decouples, mesons were octets and singlets. The prediction and subsequent observation, in 1964, of the Ω^- baryon [38] gave great credence to the proposed scheme of particles.

In the same year, following the success of the model, Gell-Mann and Feynman's PhD student Zweig postulated that all hadrons were made up of more fundamental constituents with fractional electric charge and spin 1/2,

called quarks, and organized to form a $SU(3)$ triplet: the up, down and strange [39, 40]. In particular, mesons were composed of a quark-antiquark pair and baryons of three quarks.

Problems arose, however, with the discovery of the Ω^- itself. In order to obtain the total spin 3/2, the three constituent quarks were supposed to be aligned, forming – combined with the symmetrical ground-state space wavefunction – a symmetrical state under interchange of two quarks, in violation of the Pauli exclusion principle.

The first ones to propose the existence of more than three quarks were Han and Nambu, who introduced an additional $SU(3)$ gauge degree of freedom and noted that quarks might interact via an octet of gauge vector bosons [41]. In their model, the $SU(3) \times SU(3)$ symmetry was strongly broken.

It is a few years later, in 1971, that Fritzsch and Gell-Mann postulated that the three quarks were characterized by a new conserved quantum number – the color – and the additional color symmetry $SU(3)$ was exact [42]. The baryon wavefunction was antisymmetric in the color index, and all hadron assumed to be singlet of the color group. The same authors, in 1972, made the correct interpretation of the color group as a gauge group, where the interaction among quarks was mediated by an octet of massless bosons – the gluons [43].

The failure in the search for the existence of free quarks, in the meantime, led a whole community of physicists to consider the quark as a mere mathematical tool with loose connection to reality, and suggested Fritzsch

and Gell-Mann to develop the light-cone current algebra [42].

It was Feynman, during his repeated visits to SLAC in the late 60's, to insist on the existence of point-like constituents of hadrons, leading to the development of the parton model [44, 45]. The idea of partons, applied to the then-recent deep inelastic scattering experiments performed at SLAC, could brilliantly explain the scaling behavior proposed [46], and observed, by Bjorken in 1968-1969.

The theory of quantum chromodynamics was about to be born: first mentioned by name by Fritzsch and Gell-Mann in [47], it is with the discovery of the asymptotic freedom in 1972 by 't Hooft (unpublished) and in 1973 by Gross, Politzer and Wilczek [48, 49] that precise predictions were allowed to be made in the asymptotic perturbative high energy regime.

The theory has since received extensive experimental validation at colliders such as SLAC, PETRA, LEP, mostly through deep inelastic scatterings and Drell-Yan processes. The running of the coupling constant was confirmed by numerous measurements, evidence was gathered of scaling violation, and gluon production was observed in three-jet events.

1.1.2 Asymptotic freedom and confinement

The richness of QCD phenomenology, in retrospect, is due to its intrinsic non-abelian nature, which is revealed through the self-coupling of the gauge boson, the gluon.

The classical Lagrangian density of QCD takes the form

$$\mathcal{L} = \sum_{flavor} \bar{q}_f^{\alpha}(i\ \gamma^{\mu} D_{\mu} - m_f)_{\alpha\beta}\ q_f^{\beta} - \frac{1}{4} F^a_{\mu\nu} F_a^{\mu\nu} \quad , \tag{1.1}$$

with the covariant derivative $(D_\mu)_{\alpha\beta}$, the mass term $(m_f)_{\alpha\beta}$ and the field strength tensor $F^a_{\alpha\beta}$ defined as

$$\begin{aligned} (D_\mu)_{\alpha\beta} &\equiv \partial_\mu \delta_{\alpha\beta} + ig(t_a)_{\alpha\beta} A^a_\mu \\ (m_f)_{\alpha\beta} &\equiv m_f \delta_{\alpha\beta} \\ F^a_{\mu\nu} &= \partial_\mu A^a_\nu - \partial_\nu A^a_\mu - g f_{abc} A^b_\mu A^c_\nu \ . \end{aligned} \tag{1.2}$$

The quark field, represented by q^α, belongs to the $SU(3)$ fundamental (triplet) representation, and the index α runs from 1 to 3; on the contrary, the gluon field A^a_μ belongs to the adjoint (octet) representation and $a \leq 8$. The 8 Gell-Mann 3x3 matrices $(t_a)_{\alpha\beta}$, generators of $SU(3)$ in the matrix fundamental representation, satisfy the relation $[t_a, t_b] = i f_{abc} t^c$. Finally, the gauge coupling strength is governed by the coupling constant g.

Departing from QED, where photons don't carry electric charge, in QCD a gluon is characterized by its own color-charge quantum number. This determines, in a perturbative expansion of the theory, the existence of only-gluon interaction vertices. As a consequence of the inclusion of quantum corrections, the strong coupling constant $\alpha_s = g^2/4\pi$ "runs" with the four-momentum Q^2 exchanged in the interaction and decreases for increasing val-

ues of Q^2. At first-loop order,

$$\alpha_s(Q^2) = \frac{4\pi}{(11 - \frac{2}{3}n_f)\log(Q^2/\Lambda^2_{QCD})} \quad , \tag{1.3}$$

where n_f represents the number of quark flavors. The introduction of a mass scale Λ_{QCD}, which is experimentally fixed to ≈ 200 MeV, sets a parameter used to determine the validity of the perturbative expansion and logarithmically breaks the scaling of the theory at large $Q \gg m_f$. In the high energy regime, the theory is expected to be *asymptotically free* and the quarks are treated equivalently to a weakly-coupled gas of particles.

At the other end of the energy spectrum and below the Λ_{QCD} scale, QCD is instead highly non-perturbative, and *confinement* takes place. No isolated colored charges can exist as free particles and quarks are organized into color-singlet hadrons. The potential between two color charges, for instance a quark and an antiquark, has a Coulomb-like part at short distances but a linearly rising term at long distances:

$$V_{q\bar{q}}(r) \approx -\frac{4\alpha_s}{3}\frac{1}{r} + K\ r \quad . \tag{1.4}$$

The parameter K is called string tension and represents the strength of the quark confinement force, experimentally estimated near $K \approx 0.9$ GeVfm^{-1} [2].

The description of QCD bound states via a phenomenological potential

has a limited range of applicability, mostly restricted to heavy quarkonia. The masses of charm and bottom quarks are in fact much larger than the QCD scale and the non-relativistic Schrodinger equation can be applied.

Light quarkonia, which are mostly made of u and d quarks whose mass is much smaller than Λ_{QCD}, cannot be described by this simple approach due to the importance assumed by non-perturbative corrections. At the same time though, the same application of the model to the prediction of light hadron mass-spectra has gained remarkable success [50]. This result is obtained by assigning a constituent mass to the quarks which encloses any dominant non-perturbative QCD correction.

1.1.3 Screening mass

It is legitimate to ask what happens when a system transitions from a confined state to a deconfined one, and in particular how such transformation can be achieved.

Ideally, one could imagine of compressing baryonic matter keeping the temperature constant, until a critical density is obtained and matter dissolves into a deconfined state of quarks and gluons. This is the case, for instance, of compact neutron stars. Alternatively, one could instead "heat up" the QCD vacuum in a confined volume. Above a certain critical temperature, thermal excitations would start overlapping, creating a highly-dense yet baryon-neutral system. This is generally referred to as a deconfined plasma of quarks and gluons, and can be recreated in laboratory colliding ultrarela-

tivistic heavy nuclei against each other.

Several effective models attempt to describe quantitatively the phase transition from a confined to a deconfined state of matter, as we will see in the following Sections. Let us here introduce a concept common to any high-density system of charged particles, such as the one presumably obtained when the QCD deconfined state is reached: the *Debye screening*.

In a QED plasma, the field induced by an external charge is intuitively screened by the presence of the medium which polarizes around the charge. Similarly, color charge is screened in a QCD plasma, effectively reducing the range of the force between quanta.

The (color) screening radius $\lambda_D(T)$ is inversely proportional to the temperature, or density, of the plasma, and the Debye mass is defined as $\mu_D = 1/\lambda_D$. The screening has the effect of shortening the range of the binding potential:

$$V_{q\bar{q}}(r) \approx -\frac{4\alpha_s}{3}\frac{\mathrm{e}^{-\mu_D r}}{r} + K\ r\left(\frac{1-\mathrm{e}^{-\mu_D r}}{\mu_D r}\right) \quad . \tag{1.5}$$

The resulting exponential damping of the binding force removes all long-range effects of the color charge and, at sufficiently high temperatures, it is responsible for the melting of heavy hadrons [51].

1.1.4 Bag model

The previous example of quarkonium potential has exemplified how complicated it is to provide a quantitative QCD description of hadronic physics. Several effective approaches have been developed to analyze the non perturbative regime of the theory, among which the Nambu–Jona-Lasinio model [52, 53, 54], Chiral perturbation theory [55, 56, 57], QCD sum rules [58, 59] or Lattice QCD [60].

Another powerful method that clearly shows the different behavior of the theory in its confined and asymptotically free region is the Bag model [61, 62, 63]. Citing the authors, a "strongly interacting hadron consists of fields confined to a finite region of space, which is called bag. The confinement is accomplished in a Lorentz-invariant way by assuming that the bag possesses a constant, positive energy per unit volume, B" (the bag constant). Color is confined inside the bag and quarks and gluons are treated perturbatively.

For instance, the mass of the proton is parametrized as

$$M_p \approx 3\frac{a}{r_B} + \frac{4\pi}{3} B\, r_B^3 \quad , \tag{1.6}$$

where r_B is the radius of the bag and a/r_B is the kinetic energy of each quark confined inside the volume. The second term represents the volume energy necessary to create a perturbative cavity inside a non-perturbative QCD vacuum. Further contributions to the total mass, such as the ones deriving from spin-spin interactions and virtual quark and gluons, are here

neglected. The fit to the masses of light hadrons fixes the bag constant to the empirical value $B^{1/4} \sim 125 - 145$ MeV [62], however the difference between the vacuum and QCD ground energy is constrained by other models to much larger values, of the order $B^{1/4} \sim 250$ MeV (see [64] for a more detailed discussion).

Using the bag constant, we can write the bag equation of state for the two limits $T \ll \Lambda_{QCD}$ and $T \gg \Lambda_{QCD}$. In the low temperature hadronic phase, and in the limit of $m_f = 0$ (massless quarks), the dominant excitation is the massless pion. This phase is characterized by the spontaneous breaking of chiral symmetry and the appearance of $d_\pi = (n_f^2 - 1)$ Goldstone bosons, identified with the pseudoscalar meson octet and here generically referred as pions. If we ignore further interactions among particles, we can determine pressure, energy density and entropy density using Bose-Einstein statistics:

$$\begin{aligned} p_\pi &= d_\pi \frac{\pi^2}{90} T^4 + B \\ \epsilon_\pi &= 3 d_\pi \frac{\pi^2}{90} T^4 - B \\ s_\pi &= 4 d_\pi \frac{\pi^2}{90} T^3 \ . \end{aligned} \tag{1.7}$$

The bag constant ensures that the energy density of the QCD vacuum at $T = 0$ is equal to $(-B)$.

In the high temperature, asymptotically free limit, the system can be described as a non interacting gas of quarks and gluons, governed by Fermi-

Dirac and Bose-Einstein statistics:

$$\begin{aligned} p_{qg} &= d_{qg}\frac{\pi^2}{90}T^4 \\ \epsilon_{qg} &= 3d_{qg}\frac{\pi^2}{90}T^4 \\ s_{qg} &= 4d_{qg}\frac{\pi^2}{90}T^3 \ , \end{aligned} \tag{1.8}$$

with

$$\begin{aligned} d_{qg} &= d_g + \frac{7}{8}d_q \\ d_g &= 2_{spin} \times (3^2_{color} - 1) \\ d_q &= 2_{spin} \times 2_{q\bar{q}} \times 3_{color} \times n_f \ . \end{aligned} \tag{1.9}$$

The equations of state for the hadronic and asymptotically free limit are plotted in Fig. 1.2 as a function of the temperature T. At low temperature,

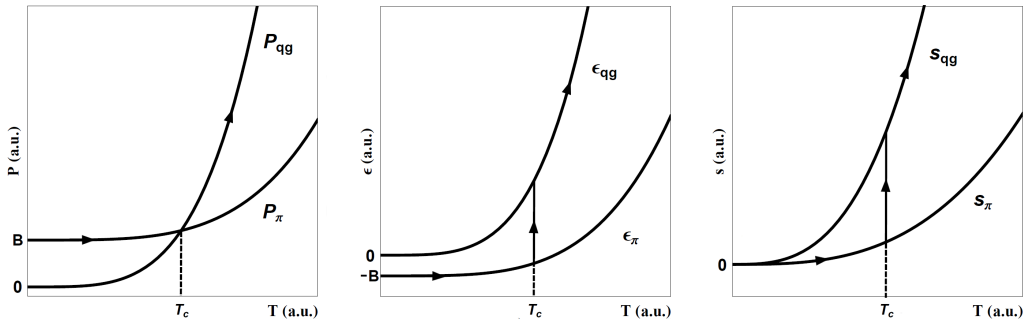

Figure 1.2: The equations of state in the bag model at finite T with zero chemical potential: pressure (*left*), energy density (*center*) and entropy density (*right*). The arrows show how the system evolves as an adiabatic increase of T.

the bag constant favors the hadronic state, while at high T the large number of degrees of freedom ($d_{qg} = 47.5$ for $n_f = 3$) promotes the free quark limit. This constitutes the evidence of a phase transition which occurs at $p_\pi(T_c) =$

$p_{qg}(T_c)$, or

$$T_c = \left(\frac{90}{\pi^2} \frac{B}{d_{qg} - d_\pi} \right)^{\frac{1}{4}} \quad . \tag{1.10}$$

Using $n_f = 3$ and $B^{1/4} = 250$ MeV, we obtain $T_c \sim 175$ MeV. We can also estimate the critical energy density required to realize a "plasma" of quarks and gluons, equal to

$$\epsilon_{crit} = \epsilon_{qg}(T_c) \sim 4B \sim 1.95 \text{ GeV fm}^{-3} \quad .$$

The density of normal nuclear matter, for reference, is approximately $\epsilon \sim 0.15$ GeV fm^3, one order of magnitude less than ϵ_{crit}.

Fig. 1.2 also gives us indication that we are dealing with a first order phase transition, since the energy and entropy densities are not continuous at T_c. However, the bag model completely neglects particle interactions on top of non-perturbative effects that acquire even more importance near the critical temperature, quickly becoming unsuitable for a quantitative description of the transition phase.

1.1.5 Chiral symmetry breaking

In the previous Section, we qualitatively identified the existence of a phase transition as the temperature grows, responsible for (1) deconfinement and (2) chiral symmetry restoration. In reality, it is not at all clear whether the two transitions coincide or not, and discussion can be found in [65] and [66].

A better description of deconfinement than the bag model is provided by the hadronic-string excitation process. In this picture, a $q\bar{q}$ meson corresponds to an open string with tension K (cf. Equation (1.4)), while a bound state of gluons corresponds to a closed string. If we compute the free energy of such string with length L in a three-dimensional square lattice with spacing a, we obtain $F = (E - TS) = (LKa - TL\log(5))$. A critical temperature is then identified at

$$T_c = \frac{Ka}{log(5)} \quad . \tag{1.11}$$

The value of this Hagedorn temperature corresponds to $T_c \sim 260$ MeV.

Another insightful order parameter of the deconfinement transition is the so called Polyakov line [67], defined as

$$P = \left\langle \mathrm{Tr}\, \mathcal{P} \exp\left(ig \int_0^{1/T} A_0(\tau, \mathbf{x}) d\tau \right) \right\rangle \quad , \tag{1.12}$$

where $\tau = ix_0$, A_0 is the temporal component of the gauge field, and $\mathcal{P}$ indicates a path-ordered exponential. The Polyakov line has zero expectation value for $T < T_c$, and non-zero expectation value otherwise. This can be related, in purely gauge theories ($n_f = 0$), to the spontaneous breaking during the deconfined phase of a discrete symmetry, $Z(N_c)$. This symmetry, however, is badly violated by dynamical quarks when $n_f \neq 0$, in which case the Polyakov line ceases to be an appropriate order parameter of deconfinement. The transition for theories with $n_f \neq 0$ is characterized instead by the

dynamical breaking of chiral symmetry.

Chiral symmetry can be directly observed in the QCD Lagrangian, Eq. (1.1), in the limit $m_f \to 0$. Since the symmetry is related to the quark-flavor degrees of freedom, we can safely ignore the color-gauge couplings, which are left invariant under both isospin and chiral transformations. For simplicity, we will also assume the existence of only two quarks, u and d, paired into an isospin doublet called q. Eq. (1.1), stripped of the quark mass term, is not only invariant under the familiar global flavor-isospin transformation $SU(2)_f$, but also under the global chiral transformation $SU(2)_5$

$$q' = \exp(-i\beta \cdot \frac{\tau}{2}\gamma_5)\ q \quad . \tag{1.13}$$

Often, both isospin and chiral symmetries are paired together and referred to as a $SU(2)_L \times SU(2)_R$ symmetry, under which transformation the kinetic part of the Lagrangian – here rearranged as

$$\mathcal{L} = \bar{q}_R i\partial\!\!\!/ q_R + \bar{q}_L i\partial\!\!\!/ q_L \tag{1.14}$$

– is invariant. The three matrices τ of Eq. (1.13) are the familiar Hermitian Pauli matrices, multiplied by the constants β. The chiral symmetry generates three associated Noether currents, which are axial vectors, and an equal number of 'conserved charge' operators, which are pseudoscalars. These operators behave like the usual flavor-isospin operators, but flip the parity of

the state on which they act.

We then have the first phenomenological evidence of the breaking of the symmetry: the absence of a degenerate quark state $|\tilde{q}\rangle$, in addition to $|q\rangle$, with opposite parity. In reality, small finite quark masses would break the chiral symmetry explicitly (cf. Eq. (1.2) and the mass therm therein) splitting the degeneracy between states, however it seems implausible that they would explain why parity doublet nucleons have never been observed.

Nambu [68] and Nambu and Jona-Lasinio [52, 53] were the first to make the hypothesis that chiral symmetry is spontaneously broken as a dynamical effect, led by the analogy with the BCS theory of superconductivity [69]. According to the Goldstone model [70], we should witness the appearance of a massless boson for every symmetry not respected by the vacuum. In this case ($SU(2)_5$ symmetry and three 'conserved charges'), the Goldstone bosons are identified with three massless pions. Details on the spontaneous breaking of the symmetry can be found in [71] or [72], where an approach based on the Nambu and Jona-Lasinio model is outlined.

Here, on the other hand, we are only interested in how to identify the transition between the two chiral phases, from a broken symmetry at low temperature, to a restored symmetry at high T. Knowing that the mass term in the Lagrangian and the corresponding operator $q\bar{q} = (q_R\bar{q}_L + q_L\bar{q}_R)$ is not invariant under chiral rotation, we can take the quark condensate $\langle q\bar{q}\rangle$

as an order parameter of the transformation:

$$\begin{aligned} \langle q\bar{q}\rangle &\neq 0 \ : \ \text{Hadron gas} \\ \langle q\bar{q}\rangle &= 0 \ : \ \text{Quark Gluon Plasma} \ . \end{aligned}$$

As the temperature increases, the $\langle q\bar{q}\rangle$ condensate is dissociated by thermal fluctuations, and a 'plasma' of quarks and gluons is formed, which will evolve at very high T to an asymptotically free gas. Simulations with three massless dynamical quarks show chiral restoration already at $T_c \sim 150$ MeV, whereas in case the physical mass of the strange quark is taken into account, this value raises to approximately 170 MeV [65].

The inclusion of the physical mass of the u, d, s quarks does not only determine the phase transition point, but also its order, as shown in Fig. 1.3. For three massless quarks, the transformation cannot be second order [73], and the system must then experience a first order chiral restoration transition. For two massless quarks, instead, the transition can be either first or second order, depending on the particular value of the strange quark mass. Finally, when all quarks acquire finite mass, the second order transition is replaced by a crossover.

1.1.6 Lattice QCD

In order to study the system near its critical point, as we saw in Fig. 1.3, we need to resort to effective theories such as the NJL model, since the per-

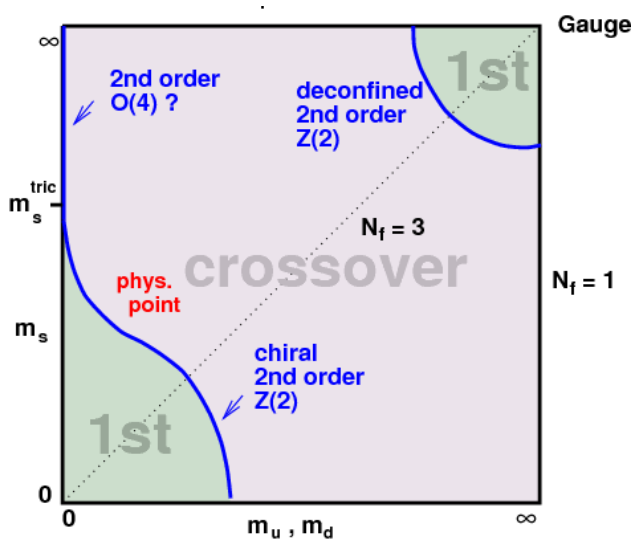

Figure 1.3: "Columbia plot": schematic phase transition behavior of $N_f = 2 + 1$ QCD for different choices of quark masses $((m_{u,d}, m_s))$ at zero baryochemical potential. Two critical lines separate the regions of first-order transitions (light or heavy quarks) from the crossover region in the middle, which includes the physical point. Taken from [1].

turbative expansion is not applicable due to the large value assumed by the coupling constant near $T \sim \Lambda_{QCD}$. This is not, however, the only available alternative: a powerful and precise method to explore the physics near T_c, although not devoid of some limitations, is to perform lattice QCD simulations.

Originally proposed by Wilson [60], this method consists of defining QCD on a space-time lattice. The motivation that first inspired the development of lattice QCD was to find a natural regulation of the ultraviolet divergencies of the theory which was applicable in a non-perturbative regime, i.e. without relying on their appearance in the Feynman graphs of perturbation theory.

The definition of a lattice spacing a, in fact, defined as the minimum distance between two space-time points, automatically sets a maximum allowed momentum $\Lambda = (\pi/a)$.

The theory, formulated in Euclidean space to treat space and time as symmetrically as possible (the connection to the Minkowski framework is provided by a Wick rotation $t \to -i\tau$), conveniently allows the direct connection between quantum field theory and statistical mechanics, and at the same time permits the computation of discreet integrals via powerful Monte Carlo numerical algorithms. Here we present a brief summary of the main results and key problems of the theory: comprehensive reviews on the subject of lattice QCD are widely available, such as in [74].

Once the lattice has been established on a hypercubic grid with spacing a, both gauge and fermion actions have to be defined. It turns out that in order to preserve gauge invariance, the theory needs to be formulated in terms of link variables, or Wilson lines,

$$U(x, x+\mu) \equiv U_\mu(x) = \mathcal{P} \exp\left(ig \int_x^{x+\mu} dz_\nu A_\nu(z) \right) \quad . \tag{1.15}$$

$\mathcal{P}$ indicates a path ordered product along the direction μ that connects two points on the grid (x and $x+\mu$), and it is mathematically analogous to the time-evolution operator in quantum mechanics. The fundamental blocks that form the gluon (S_g) and quark (S_f) actions are, respectively, the Wilson

loop $W(\mathcal{C}) = \mathrm{Tr}\left(U_\mu(x)U_\nu(x+\mu)U_\mu^\dagger(x+\nu)U_\nu^\dagger(x)\right)$ and the quark bilinear $\bar{q}(x)U_\mu(x)q(x+\mu)$:

$$\begin{aligned} S_g &= \frac{6}{g^2}\sum_x \sum_{\mu<\nu} \mathrm{Re\ Tr}\ \frac{1}{3}(1 - U_{\mu\nu}(x)) \\ &\underset{a\to 0}{\longrightarrow} \quad \frac{1}{4}\int d^4x F_{\mu\nu}F^{\mu\nu} \quad , \end{aligned} \tag{1.16}$$

$$\begin{aligned} S_q &= \frac{1}{2a}\sum_x \bar{q}(x)\gamma_\mu \left(U_\mu(x)q(x+\mu) - U_\mu^\dagger(x-\mu)q(x-\mu)\right) \\ &\underset{a\to 0}{\longrightarrow} \quad \bar{q}(\not{\partial} + ig\gamma_\mu A^\mu)q \quad . \end{aligned} \tag{1.17}$$

This naive definition of the quark action, however, leads to a well-known issue called the fermion-doubling problem, which causes the creation of 2^{dim} degenerate fermions. Various solutions have been proposed [60, 75], at the price of breaking chiral symmetry explicitly. A no-go theorem by Nielsen and Ninomiya [76, 77], in fact, states that it is not possible to define a local, translationally invariant, Hermitian lattice action that preserves chiral symmetry and does not have doublers. This problem needs to be carefully addressed when lattice QCD simulations are used to study the transition of the system near the critical point.

The action defined in Eq. (1.16) and Eq. (1.17) is then quantized a la Feynman using the path-integral method. The resulting partition function is given by an integral over only-gauge configurations,

$$Z = \int \mathcal{D}U\ \mathcal{D}\bar{q}\ \mathcal{D}q\ \mathrm{e}^{-S_g(U) - S_q(\bar{q},q,U)} = \int \mathcal{D}U \det M\ \mathrm{e}^{-S_g(U)} \quad , \tag{1.18}$$

with $\mathcal{D}$U the Haar measure and $\det M$ a determinant that contains all the fermionic contributions. A frequently used simplification, the so-called quenched approximation, is obtained by setting $\det M = const$ and neglecting any vacuum polarization effect.

Numerical integrations are often performed in such approximation. Even then, however, the computational expense seems prohibited: the total number of gluon integrations $\int \mathcal{D}U$, in fact, can reach several orders of magnitude already for moderately sized lattices. The solution is to perform the integrations using Monte Carlo methods, paired – whenever possible – by importance sampling (also cf. Section 3.1). Details on some of the algorithms used can be found in [78] and [79].

The first example of a lattice QCD computation is the heavy quark-antiquark potential $V(R)$, Eq. (1.4). The Wilson loop $\langle W(\mathcal{C})\rangle$, in fact, is proportional to $\exp(-V(R)\tau)$, where the area enclosed by the loop $\mathcal{C}$ is equal to $A = (R \times \tau)$. The potential can therefore be extracted as

$$V(R) = -\lim_{\tau\to\infty} \frac{1}{\tau} \log\langle W(\mathcal{C})\rangle \quad . \tag{1.19}$$

In Fig. 1.4, lattice QCD results are shown together with an empirical linear plus Coulomb potential, confirming the qualitative results obtained in the previous Sections: the attractive short-distance potential becomes linearly confining at long distances.

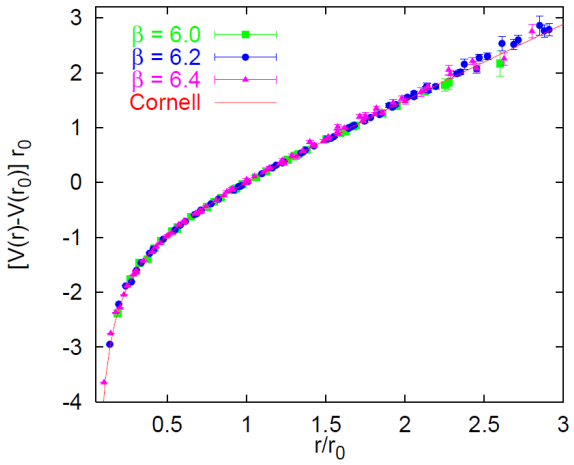

Figure 1.4: The quenched Wilson action $SU(3)$ potential, normalized to $V(r_0) = 0$. Taken from [2].

The second example is the variation of the pressure and energy density with T near the critical point. Before presenting the results, however, we need to provide the link between statistical mechanics and lattice QCD, i.e. we need to define lattice QCD at $T \neq 0$. Let's take a step back then, and look at the path-integral formulation in quantum field theory of the transitional amplitude

$$\langle \phi_a | \mathrm{e}^{-iHt} | \phi_a \rangle = \int \mathcal{D}\pi \, \mathcal{D}\phi \, \exp\left(i \int_0^t dt \int d^3x \left(\pi\dot{\phi} - \mathcal{H} \right) \right) \quad . \tag{1.20}$$

Here π is the conjugate momentum of the field ϕ, and $\mathcal{H}$ represents the Hamiltonian density. In statistical mechanics, on the other hand, the parti-

tion function Z is given by

$$Z = \mathrm{Tr}\ \mathrm{e}^{-(H-\mu N)/T} = \sum_a \int d\phi_a \langle \phi_a | \mathrm{e}^{-(H-\mu N)/T} | \phi_a \rangle \ . \tag{1.21}$$

The similarity between the two expressions is evident, and in fact one can write the partition function as an integral over fields and their conjugate momenta performing the following substitutions:

$$t \to -i\tau \ , \quad \mathcal{H} \to \mathcal{H} - \mu\mathcal{N} \ , \tag{1.22}$$

where $\mathcal{N}$ is the conserved change density, if the system admits one. Then,

$$Z = \int \mathcal{D}\pi\ \mathcal{D}\phi\ \exp\left(\int_0^{1/T} d\tau \int d^3x \left(i\pi\dot{\phi} - \mathcal{H} + \mu\mathcal{N} \right) \right) \ , \tag{1.23}$$

with periodic boundary conditions such that $\phi(\mathbf{x}, 0) = \phi(\mathbf{x}, 1/T)$.

This analogy establishes the first step toward the definition of quantum field theory at finite temperature, as we will see in the following Sections. However, it also allows for a clever definition of temperature in the context of lattice QCD, by simply resizing the temporal dimension of the lattice:

$$T^{-1} = N_t a \ , \quad V = (N_s a)^3 \ . \tag{1.24}$$

Since we are already dealing with an Euclidean space-time framework, only the boundary conditions for the Wilson line and fermion fields need to be

imposed,

$$U_\mu(\mathbf{x}, \tau + N_t a) = U_\mu(\mathbf{x}, \tau) \quad , \quad q(\mathbf{x}, \tau + N_t a) = -q(\mathbf{x}, \tau) \quad . \tag{1.25}$$

The zero temperature limit is obtained when $N_t = N_s \to \infty$, while thermodynamics relations are satisfied in the limit $N_s \gg N_t$.

Applying numerical methods, one can then compute thermodynamic variables such as $p(T)$ (pressure) or $\epsilon(T)$ (energy density), and study the equation of state of the system near the critical point T_c. Results are shown in Fig. 1.5

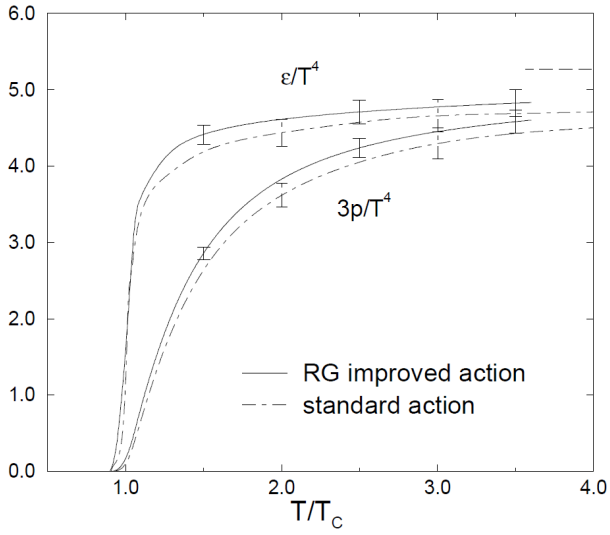

Figure 1.5: Equation of state for the pure Yang-Mills theory in Monte Carlo simulations. The error bars indicate uncertainties from statistical and systematic errors. The dashed horizontal line on the top-right indicates the Stefan-Boltzmann limit of the energy density. Taken from [3].

for a pure gauge theory (quenched action), and in Fig. 1.6 when dynamical quarks are included as well.

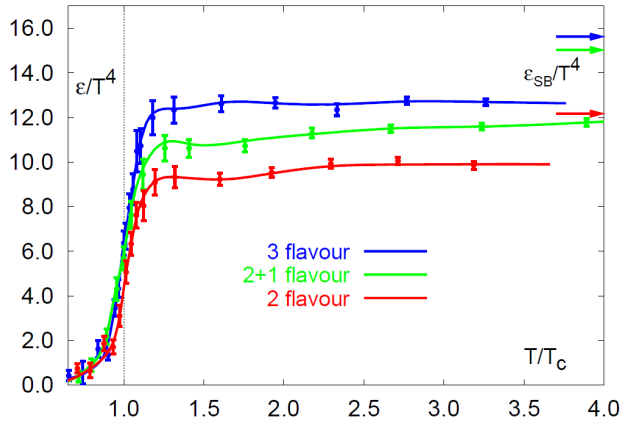

Figure 1.6: The energy density of QCD with dynamical quarks in lattice Monte Carlo simulations. The arrows show the Stefan-Boltzmann limit. Taken from [4].

The numerical results confirm once again our qualitative analysis of Sec. 1.5. The rapid increase of the energy density near the critical temperature is evidence of a phase transition where the system develops a high number of new degrees of freedom. The pressure, on the contrary, increases rather slowly and determines a sudden decrease of the speed of sound $c_s^2 = \partial p/\partial \epsilon$ in a narrow region near T_c. It is not clear from the figures whether the transition order is first (discontinuity in $\epsilon(T)$) or second, although further analysis [80] show that in the pure gauge scenario the transition is indeed first and in agreement with Fig. 1.3. The critical temperature, in the massless limit, can

be extracted as [4] ;

$$\begin{aligned} T_c(N_f = 0) &\approx 273 \text{ MeV} \\ T_c(N_f = 2) &\approx 175 \text{ MeV} \\ T_c(N_f = 3) &\approx 155 \text{ MeV} \quad . \end{aligned}$$

Other estimates [81], which include physical light and strange quark masses, suggest a transition temperature of

$$T_c(N_f = 3, m_f \neq 0) \approx 192 \text{ MeV} \quad .$$

In more recent calculations [8, 82, 83, 84], it was shown that the phase transition occurs over a broader range of temperatures, and the "soft point" where the speed of sound drops near T_c is not so pronounced as originally thought. We report the new results in Fig. 1.11, where the lattice equation of state is used in combination with hydrodynamical models of plasma expansion.

1.1.7 Phase diagram

Quantum chromodynamics, at intermediate energies of the order of Λ_{QCD}, is probed studying a collective system of particles, where thermodynamical quantities can be defined. The most interesting properties of the theory, not surprisingly, happen to manifest themselves in the most challenging region of phase space, near or just above the critical phase transition point.

In our brief summary, we have explored the evolution of the theory from asymptotic freedom down to low temperatures, culminating with a powerful tool, lattice QCD, suitable to test the theory even in its non-perturbative regime. We didn't mention that results are valid only in the limit of vanishing baryochemical potential μ_B, a limit which seems very distant from out seemingly baryon-dominated universe. In reality, as we will see in the following Section, there are plenty of situations where such asymptotic conditions can be achieved, such as in heavy ion collisions.

The best way to characterize the phenomenological implications of QCD it to plot its phase diagram as a function of the temperature T and the baryochemical potential μ_B, which brings us all the way back to Figure 1.1. In this diagram, the lattice QCD results shown so far sit along the ordinate axis, where the transition from a hadron gas to a quark gluon plasma is a smooth crossover once dynamical, massive quarks are properly taken into account. For increasing values of μ_B, the crossover between the two states is replaced by a first order transition. On the verge of the first order transition line sits a critical point whose location on the diagram is currently object of theoretical and experimental research.

Lattice QCD computations at finite values of μ_B are hard to achieve due to a notorious issue called the sign problem [85]. Collision experiments performed at particle accelerators, on the contrary, are good candidates for probing the region around the critical point. For high $\sqrt{s}$ collision energies, in fact, the hot plasma produced during the impact is known to thermalize at

decreasing values of the baryochemical potential. In particular, the regions of phase space probed by the Relativistic Heavy Ion Collider at the Brookhaven National Laboratories, and the Large Hadron Collider at CERN, are shown on the diagram.

Our efforts, in this thesis, will be directed to the construction of a suitable phenomenological model, called CUJET, capable of making accurate predictions of the observations carried out at RHIC and LHC. Nuclear matter, in this region, is supposed to transition to a strongly coupled plasma, known as sQGP. Our model predictions, compared to future and available data, will allow us to test the understanding of the quark gluon plasma in terms of the underlying theory of quantum chromodynamics.

1.2 Quark Gluon Plasma

The physics of high-energy heavy ion collisions can be divided in three phases:

1. Color Glass Condensate and Glasma
2. (strongly coupled) Quark Gluon Plasma
3. Hadron Gas

An illustration of these stages is given in Fig. 1.7.

In the instants preceding the impact, the approaching nuclei are traveling at relativistic speeds and look Lorentz-contracted in the rest frame of the

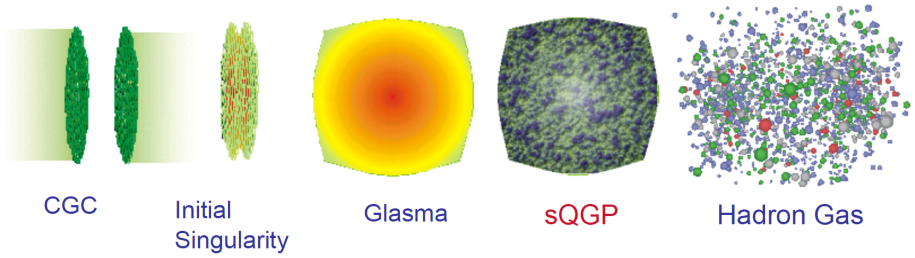

Figure 1.7: A cartoon of the collision of two high-energy hadrons. Taken from [5].

laboratory. A dense cloud of gluons surrounds the valence partons and can be described by a superposition of coherent classical color-electric and color-magnetic fields – the Color Glass Condensate – transverse to the beam axis.

Due to the high energy of the collision, the two nuclei interpenetrate each other mostly unchanged, i.e. they carry the baryonic matter away with them. At the same time, though, they acquire a net color charge and "leave behind" a color-rich and baryon-free region known as Glasma. This region is described by longitudinal color flux-tubes that connect the two receding nuclei and eventually decay into a plasma of $q\bar{q}$ pairs and gluons.

Extremely high densities and temperatures determine the particle thermalization in a time shorter than 1 fm/c: the Quark Gluon Plasma is created. A strongly coupled plasma of deconfined quarks and gluons, at least at the energies accessible at RHIC and LHC, the QGP appears to behave as a fluid whose expansion is governed by the laws of relativistic hydrodynamics.

While the system expands, it inevitably cools down and experiences a second phase transition back to the hadronic state, immediately followed by freeze-out and the formation of a gas of hadrons (Hadronic Gas). These are the final products of the collision which are ultimately revealed by the experiment detectors.

1.2.1 Initial conditions

The hadronic constituents of a nucleon can be divided in valence partons (quarks), and wee partons (sea quarks and gluons), whose nature is highly non-perturbative.

At low fractional momentum x ($x = E_{parton}/E_{Nucleon}$), the parton distribution function is dominated by the gluon component, which grows indefinitely for $x \to 0$, as shown in Fig. 1.8. Furthermore, at small x the

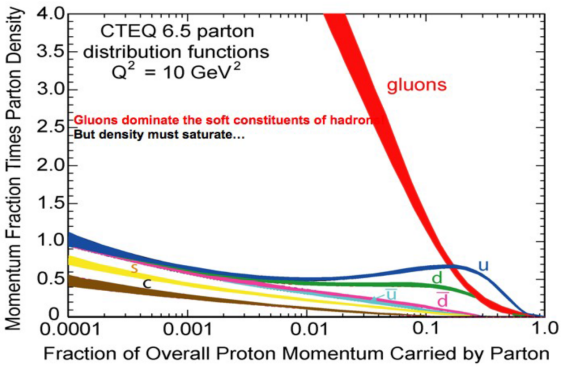

Figure 1.8: A gluon and quark composition of a hadron as a function of the fractional momentum x. Taken from [5].

distribution function itself is seen to rise logarithmically with the exchanged momentum Q^2 [86].

Smaller x and larger Q^2 become increasingly accessible at higher collision energies, since for a typical gluon with momentum p of the order of Λ_{QCD}, x tends to 0 as the energy of the nucleon increases. At the same time, the cross section is known to expand more slowly than the total number of gluons [87]. The combined effect results in the wavefunction of the hadron being strongly dominated by a very high density of small x gluons [88, 89], which are the real protagonists of the inelastic collision.

Because the gluons are so densely packed together, the system is analogous to a plasma at extreme temperatures, and asymptotic freedom guarantees that the interaction strength will be small, $\alpha_s \ll 1$. The rapid increase of the gluon density, however, cannot continue indefinitely, and indeed it will saturate once the gluons start to overlap with each other [90, 91].

The saturation momentum scale $Q_s(x, A)$ is defined such that for gluons with transverse momentum $p_\perp > Q_s$ the phase-space density grows quickly, whereas for gluons with $p_\perp \leq Q_s$ the phase-space density saturates at $\sim 1/\alpha_s(Q_s)$ and grows only logarithmically thereafter.

Given $\alpha_s \ll 1$, the occupation number is large and the system can be treated classically, with the gluons represented by classical coherent fields (Color Condensate) [92, 93].

If the small x gluons can be described by classical fields, on the contrary large x gluons can be treated as their sources, which evolve slowly in time due to relativistic dilation effects (Glass). The distinction between the two scales is entirely arbitrary, and a correct description of the small x physics is achieved only after applying renormalization group analysis [94]. It turns out that the evolution equations are diffusive and have universal solutions: the color glass condensate represents indeed the universal form of high-energy QCD wavefunctions at small x.

The colliding nuclei, depicted in the laboratory frame by two sheets of CGC [95], pass through one another during the impact nearly unchanged, although they acquire color-electric and color-magnetic charge. As mentioned earlier, the baryonic matter identified by the large x valence quarks almost doesn't take part in the interaction, leaving a baryon-free region behind. However, longitudinal color-electric and color-magnetic coherent fields are formed between the receding sheets.

This intermediate state, called glasma [96], dilutes as the system expands and eventually decays into a plasma of quarks and gluons. These particles are formed in their rest frame (*inside-outside cascade*, cf. Section 5.1 for more details) in a formation time scale of the order of $1/Q_s \sim 0.2 - 0.3$ fm/c at RHIC [7].

Experimental evidence of CGC

Our understanding of the initial conditions in terms of classical, coherent, color fields needs to be validated experimentally before a successful theory of color glass condensate can be established. A growing body of evidence resides in a variety of measurements carried out in several experiments at different accelerators.

In particular, the CGC hypothesis is largely supported by electron-proton scattering measurements, which can easily probe the physics of small $x \leq 10^{-2}$ [97, 98, 99].

In heavy ion collisions, evidence can be found in several observables, for instance: (1) particle multiplicity in A+A collisions [100, 6, 101]; (2) forward, intermediate $p_\perp$ hadron-spectrum suppression in d+A collisions [102, 103, 104]; (3) suppression of forward azimuthal back-to-back correlations in d+A [105, 106]; (4) long-range rapidity correlations in A+A, a phenomenon known as the 'ridge' [107].

An example of (1) is shown in Fig. 1.9, where the initial pseudorapidity density of charged particles predicted by CGC models is in agreement with data from lead-lead (Pb+Pb) collisions at RHIC.

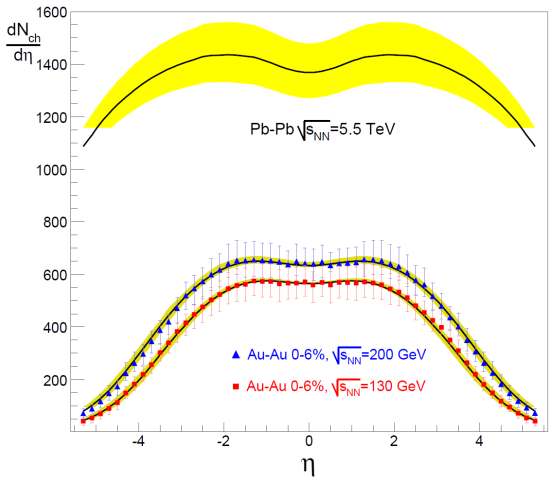

Figure 1.9: Pseudo-rapidity density of charged particles produced at RHIC at different center-of-mass energies. The upper band represents the prediction of Pb-Pb collisions at LHC. Taken from [6].

1.2.2 Thermalized plasma

The quark gluon plasma, created in the first instants after the collision, is the decay product of the intermediate glasma state. Its very same existence and the possibility to be produced as a result of heavy ion collisions were first theorized nearly forty years ago at a workshop at Bear Mountain, New York [108]. At that time, T.D. Lee suggested to "investigate [...] phenomena by distributing high energy or high nucleon density over a relatively large volume" [109]. The restoration of the broken symmetries of the physical vacuum would in fact make ultra-dense states of nuclear matter experimentally accessible [110, 111]. An insightful summary of the exciting path that led to the draft of the 1983 DOE/NSAC Long Range Plan and the following construction of the Relativistic Heavy Ion Collider can be found in [112].

The discovery of the quark gluon plasma as a new form of QCD matter was announced soon after the first results from RHIC were made widely available in four comprehensive papers by the BRAHMS [113], PHENIX [11], PHOBOS [114] and STAR [115] collaborations. This ultra-dense, strongly-coupled, deconfined form of matter is supposed to form at energy densities of approximately 2 GeV/fm^3, evolving from an initial state of even higher $\epsilon \sim 20 - 30$ GeV/fm^3 to a mixed gluonic and hadronic plasma after a time of about 3 fm/c [7]. Decoupling and full hadronization take place at later times $\sim$ 10 fm/c, as shown in the diagram of Fig. 1.10.

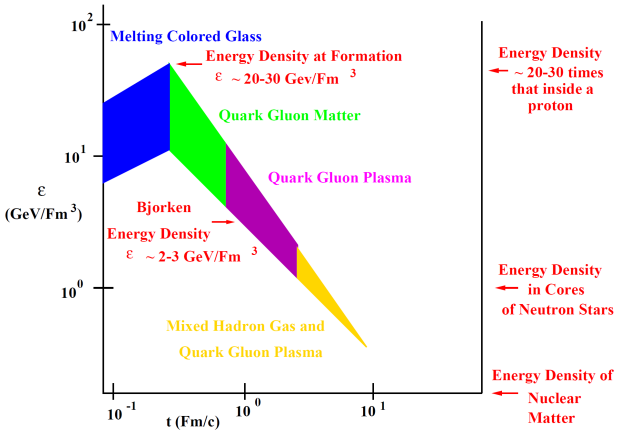

Figure 1.10: Bounds on the energy density as a function of time in heavy ion collisions. Taken from [7].

The properties and dynamics of the QGP can be described by a collective, macroscopic theory such as relativistic hydrodynamics. This assumption holds for locally equilibrated systems, where the mean free path of the plasma

constituents is much smaller than the size of the system. In the specific case of the QGP, this is especially true for the "bulk" matter composed by low momentum particles, or $p_\perp \lesssim 2$ GeV.

The characteristics of this "fluid" and the phenomenological consequences in terms of experimental measurements will be detailed in the next Section. Our first step into the analysis of the plasma, in fact, starts from the description of the fundamental interactions among its constituents at the microscopic level of QCD at finite temperature.

1.2.3 Finite temperature QFT

The key concept that allows the definition of a quantum field theory at $T \neq 0$ was already introduced at the end of Section 1.1.6. Switching to Euclidean metric with a rotation in the complex temporal plane, $t \to -i\tau$, we were in fact able to redefine the grand-canonical partition function Z as a path-integral over the fields and their conjugate momenta (cf. Eq. (1.23)). The inverse temperature is defined as the temporal size of the integration ($\tau_f = 1/T$), while periodicity conditions imposed on the fields ensures that initial and final states coincide ($\phi(1/T, \mathbf{x}) = \phi(0, \mathbf{x})$).

The expression of the partition function can be further simplified if one

integrates over the conjugate momenta[1], leading to the form

$$Z = \int \mathcal{D}\phi \, \exp\left(- \int_0^{1/T} d\tau \int d^3x \, \mathcal{L}(\phi(\tau, \mathbf{x}), \partial\phi(\tau, \mathbf{x})) \right) \quad , \tag{1.26}$$

where the Lagrangian density along with all the fields and variables have been defined in Euclidean space-time.

The most remarkable consequence of dealing with a finite temporal size and periodic boundary conditions is the discretization of the temporal component of the four-momentum (Matsubara frequencies), when the fields are expanded in terms of Fourier components:

$$\phi(\tau, \mathbf{x}) = T \sum_n \int \frac{d^3k}{(2\pi)^3} \mathrm{e}^{i(\omega_n \tau + \mathbf{k}\cdot\mathbf{x})} \phi(\omega_n, \mathbf{k}) \quad , \tag{1.27}$$

$$\omega_n = \begin{cases} 2n\pi T & \text{for gluons} \\ (2n+1)\pi T & \text{for quarks} \quad . \end{cases} \tag{1.28}$$

In a free theory, this is sufficient to compute explicitly the partition function, from which the desired thermodynamic quantities can be extracted. If interactions are turned on, instead, one needs to apply the same familiar stratagems used in perturbation theory. The Lagrangian can be split into a

[1]The momentum integrals generally appear as simple products of Gaussian integrals.

free and interaction part,

$$S = S_0 + S_I \equiv \int_0^{1/T} d\tau \int d^3x \ (\mathcal{L}_0 + \mathcal{L}_I) \quad , \tag{1.29}$$

and the partition function written as

$$Z = \sum_n \frac{1}{n!} \int \mathcal{D}\phi \ (-S_I)^n \mathrm{e}^{-S_0} \quad . \tag{1.30}$$

Expressions for the Feynman vertices can be read off the interaction Lagrangian, while free propagators are obtained as functional derivatives of Z_0. For reference, the gluon propagator in the covariant gauge becomes

$$\Delta_{\mu\nu}(Q) = \frac{1}{Q^2}(\delta_{\mu\nu} - (1-\xi)\frac{Q_\mu Q_\nu}{Q^2}) \quad , \tag{1.31}$$

with $Q_\mu = (\omega_n, \mathbf{q})$.

The interaction theory, defined in Euclidean space, is useful to compute static properties of the system such as thermodynamic potentials. For dynamical quantities, however, real-time green functions are required. These can be extracted as real continuations of their imaginary time counterparts [116], or formulated directly by choosing an appropriate path for the temporal integration on the complex plane $(\mathrm{Re}\, t, \mathrm{Re}\, \tau)$ [117].

As an application of thermal perturbation theory, we will show the results relative to the gluon propagator at finite T. The changes induced by the

presence of a thermal medium, in fact, explain the origin of some of the properties of the QGP, such as the Debye screening mass already mentioned in Section 1.1.3.

The self-energy of the gluon, Π, is computed in the Hard Thermal Loop (HTL) approximation, in which the temperature is assumed to dominate over all the other scales in the loop diagrams. This implies that only the contributions proportional to g^2T^2 are considered. Contrary to the vacuum theory, where the unphysical polarizations that appear in the covariant gauge are canceled by the ghost loops, here the gluon propagator develops a longitudinal polarization in addition to the transverse one. After analytically continuing the Green's function to real time and Minkowski metric, the propagator in the HTL approximation reads

$$\Delta_{\mu\nu} = \frac{(P_L)_{\mu\nu}}{Q^2 - \Pi_L} + \frac{(P_T)_{\mu\nu}}{Q^2 - \Pi_T} + \xi \frac{Q_\mu Q_\nu}{Q^2} \quad . \tag{1.32}$$

The four-momentum Q_μ is now continuous with $Q_\mu = (\omega, \mathbf{q})$ and $(P_T)_{\mu\nu}$, while $(P_L)_{\mu\nu}$ represent the usual transverse and longitudinal projector operators. The transverse and longitudinal self-energies are expressed as

$$\begin{aligned} \Pi_L(x \equiv \frac{\omega}{q}) &= \mu_D^2 \left(1 - x^2 - \frac{x(1-x^2)}{2}\left(\log\left(\frac{x+1}{x-1}\right) - i\pi\theta(1-|x|)\right)\right) \\ \Pi_T(x \equiv \frac{\omega}{q}) &= \mu_D^2 \left(\frac{x^2}{2} + \frac{x(1-x^2)}{4}\left(\log\left(\frac{x+1}{x-1}\right) - i\pi\theta(1-|x|)\right)\right) \quad , \end{aligned} \tag{1.33}$$

with $q \equiv |\mathbf{q}|\mu_D$ the Debye screening mass defined as

$$\mu_D = gT\sqrt{1 + \frac{N_f}{6}} \quad . \tag{1.34}$$

Let's now look at the following limits, starting from the time-like region $\omega > q$ and in particular the case with $q = 0$. In this situation, both the longitudinal and transverse propagators develop a pole for

$$\omega^2 = \frac{\mu_D^2}{3} \equiv \omega_{pl}^2 \quad . \tag{1.35}$$

The characteristic frequency of the plasma is then identified with ω_{pl}. For collective modes with soft momenta $q \neq 0$, $q \ll \mu_D$, the above relation becomes

$$\begin{aligned} \omega^2 &\simeq \omega_{pl}^2 + \frac{3}{5}q^2 \qquad \text{for longitudinal modes} \\ \omega^2 &\simeq \omega_{pl}^2 + \frac{6}{5}q^2 \qquad \text{for transverse modes} \quad . \end{aligned} \tag{1.36}$$

For hard momenta, $q \gg \mu_D$, we have instead

$$\begin{aligned} \omega^2 &\simeq q^2\left(1 + 4\exp\left(\frac{2q^2}{3\omega_{pl}^2} - 2\right)\right) \qquad \text{longitudinal} \\ \omega^2 &\simeq q^2 + \frac{3}{2}\omega_{pl}^2 \qquad\qquad\qquad\qquad\quad \text{transverse} \quad . \end{aligned} \tag{1.37}$$

We immediately see that the term ω_{pl} acts as an effective mass for a gluon propagating in the plasma. These plasma oscillations, or quasi-particles, are called plasmons.

If we switch to the space-like region $\omega < q$, we notice that the self-energies

Eq. (1.33) develop an imaginary part responsible for what is called Landau damping, which is an effect associated with the energy transfer from the collective modes to the plasma constituents. Near the static limit $\omega \ll q$ (static meaning that the field configuration can be represented by time-independent gauge potentials), the longitudinal and transverse gluon propagators can be written as

$$\begin{aligned} \Delta_L(\omega, q) &= \left(q^2 + \mu_D^2 + i\frac{\pi\mu_D^2}{2}\frac{\omega}{q} \right)^{-1} \\ \Delta_T(\omega, q) &= \left(q^2 - i\frac{\pi\mu_D^2}{2}\frac{\omega}{q} \right)^{-1} \end{aligned} \tag{1.38}$$

For $\omega = 0$ (purely static fields), the longitudinal gluon propagator develops an effective mass term equal to μ_D.

This is precisely the Debye mass responsible for the screening of the color-electric field in the plasma, which leads to the Yukawa potential between a heavy $q\bar{q}$ pair seen in Eq. (1.5). In this limit, the transverse gluon is massless and magnetic interactions are long-ranged, or unscreened. Due to Landau damping, however, also magnetic interactions become dynamically screened for finite values of ω. The transverse propagator squared that appears in the computation of the cross section, in fact, takes the form

$$|\Delta_T(\omega, q)|^2 \simeq \left(q^4 - \left(\frac{\pi\mu_D^2\omega}{4q} \right)^2 \right)^{-1} , \tag{1.39}$$

which shows that the imaginary part of the propagator acts as a frequency-dependent infrared cutoff at momenta $p \sim (\omega\mu_D^2)^{1/3}$. The dynamical screening of the soft momenta plays an important role in taming the singularities

in the scattering processes with the exchange of transverse gluons.

An equivalent approach to the derivation of the HTL gluon self-energy using the perturbative expansion is given by kinetic theory and the solution of the coupled set of Vlasov equations. In this semi-classical approach, one considers a relativistic plasma composed of charged particles whose space-time-dependent density distribution function is given by $n_{\pm}(\mathbf{p}, x)$. The system is subject to the effects of an external source and an induced electromagnetic field:

$$\partial_{\mu} F^{\mu\nu}(x) = j^{\nu}_{ind}(x) + j^{\nu}_{ext}(x) \ , \tag{1.40}$$

$$j^{\mu}_{ind}(\mathbf{x}, t) = 2e \int \frac{d^3p}{(2\pi)^3} v^{\mu} \left(n_{+}(\mathbf{p}, \mathbf{x}, t) - n_{-}(\mathbf{p}, \mathbf{x}, t) \right) \ , \tag{1.41}$$

$$\left(\frac{\partial}{\partial t} + \mathbf{v} \cdot \frac{\partial}{\partial \mathbf{x}} \pm \left(\mathbf{E}(\mathbf{x}, t) + \mathbf{v} \times \mathbf{B}(\mathbf{x}, t) \right) \cdot \frac{\partial}{\partial \mathbf{p}} \right) n_{\pm}(\mathbf{p}, \mathbf{x}, t) = 0 \ , \tag{1.42}$$

with $x = (t, \mathbf{x})$, $v^{\mu} = (1, \mathbf{v})$ and the last equation representing the time-evolution of the distribution $n_{\pm}(\mathbf{p}, x)$. By linearizing

$$n_{\pm}(\mathbf{p}, \mathbf{x}, t) = n_0(\mathbf{p}) + \delta n(\mathbf{p}, \mathbf{x}, t) \ , \tag{1.43}$$

where $n_0(\mathbf{p})$ is the density distribution in the absence of an induced field, and further writing

$$j^{\mu}_{ind}(\mathbf{x}, t) = \int d^4y \, \Pi^{\mu\nu}(x - y) A_{\nu}(y) \ , \tag{1.44}$$

one can derive the same expressions for the self-energy of Eq. (1.33) after solving explicitly for $j^{\mu}_{ind}(\mathbf{x}, t)$. More details on this approach can be found in [118].

1.2.4 Hydrodynamics and collective flow

The underlying microscopic theory of quark gluon plasma is QCD at finite temperature. At the macroscopic level, however, the thermalized plasma should behave as a fluid and as such it is expected to obey to the laws of hydrodynamics.

The connection between finite temperature QCD and hydrodynamics is given by the possibility to compute from the microscopic theory quantities such as transport coefficients, using Kubo formulae [119, 120], or the equations of state, often derived from lattice QCD simulations. An example of the latter is given in Fig. 1.11. In addition to the pressure and energy density as already shown in Fig. 1.5 and Fig. 1.6, here we also report the speed of sound and the trace anomaly. In particular, the trace anomaly Tr $T^{\mu\nu} = (\epsilon - 3p)$ indicates the deviation from a purely conformal theory [121], a limit reached in QCD for $T \gg \Lambda_{QCD}$.

The knowledge of the equation of state and the plasma initial conditions at thermalization (either determined by CGC or by the Glauber model [122] described later in Section 5.1.1) are the necessary inputs to calculate the evolution of the system in a relativistic hydrodynamical framework. A review on the application of hydrodynamics to heavy ion collisions can be found in

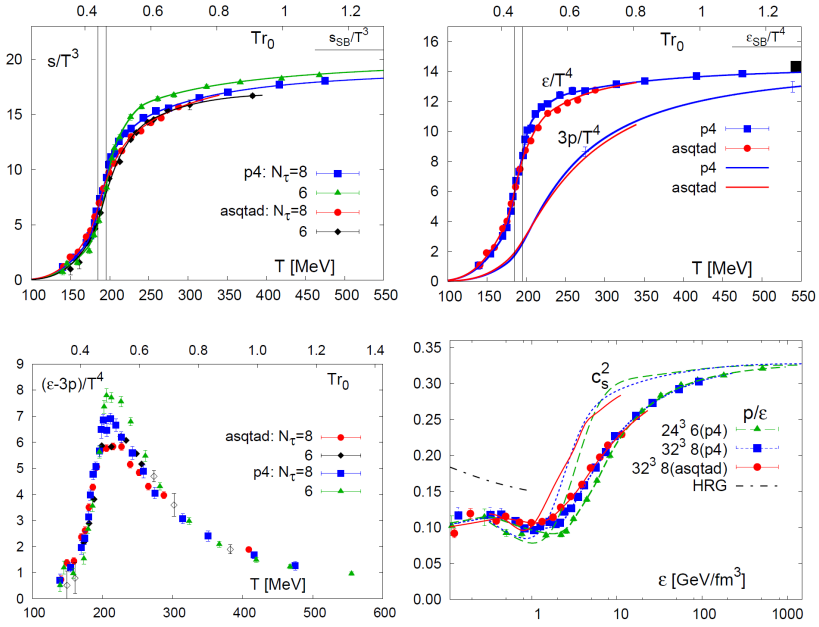

Figure 1.11: Recent calculations of the equations of state of QCD with physical quarks in lattice Monte Carlo simulations. From the top-left, clockwise: the entropy density, the energy density and pressure, the speed of sound and the trace anomaly. Taken from [8].

[123].

The hydrodynamical picture is expected to hold only at early times after the collision, when the plasma is sufficiently hot and before a mixed gluonic-hadronic state is formed: $0.3 \sim 1$ fm/c $\gtrsim \tau_{hydro} \gtrsim 3$ fm/c. The validity of this assertion, far from being granted, needs to be checked experimentally and indeed it constitutes one of the strongest signatures of QGP.

A possible observable directly related to the formation of a strongly coupled plasma is the measurement of the anisotropic elliptic flow in non-central collisions [124]. By centrality, it is intended a class of A+A events charac-

terized by a specific impact parameter: for larger impact parameters, the collision is said to be more peripheral, i.e. non-central, and the interested region assumes an increasingly more elliptical shape. In a strongly coupled medium, the pressure gradients due to this initial azimuthal anisotropy are efficiently transferred into the collective flow of its components. The different types of collective flows, in turn, are quantified in terms of the first Fourier components of the azimuthal angle distribution [125]:

$$\frac{dN_h}{dydp_\perp d\phi} = \frac{dN_h}{dydp_\perp}\frac{1}{2\pi}\left(1 + 2v_1\cos\phi + 2v_2\cos 2\phi + \cdots\right) \quad . \tag{1.45}$$

Here $dN_h/dydp_\perp d\phi$ represents the number of hadrons of species h observed at rapidity y, with transverse momentum $p_\perp$ and azimuthal angle ϕ. Both $dN_h/dydp_\perp d\phi$ and the Fourier coefficients $v_i(y, p_\perp, h)$ depend on the initial rapidity density dN_i/dy. dN_i/dy, needless to say, is function of the energy and centrality of the collision.

The remarkable agreement, shown in Fig. 1.12, between the elliptic flow v_2 predicted by hydrodynamical models and measured at RHIC is one of the most convincing evidences of QGP formation. Several conclusions can be drawn at this point:

- The QGP at RHIC behaves similarly to a *perfect fluid* [126, 127, 128]: the theoretical curves of Fig. 1.12 are in fact obtained using perfect (Euler) hydrodynamics equations, starting from a lattice equation of state that encloses all the features of a phase transition, including the

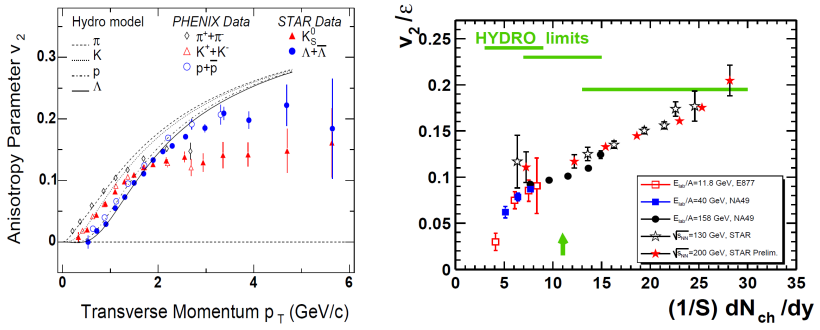

Figure 1.12: Bulk collective flow is the barometric signature of QGP production. *left* RHIC measurements of the azimuthal elliptic flow $v_2(p_\perp)$ are shown to agree with the predicted perfect fluid hydrodynamical flow in the bulk $p_\perp \lesssim 1$ GeV domain. *right* $v_2(p_\perp)$ as a function of the charged particle rapidity density. When dN/dy drops below the values achieved at RHIC, the elliptic flow falls below the perfect fluid hydrodynamic predictions. Taken from [7].

drop of the speed of sound near T_c. The perfect fluidity during the early deconfined phase is determined by a low value of the viscosity to entropy density ratio η/s [129], which is in turn caused by a spiked increase of the number of degrees of freedom during the deconfined phase.

- The collective flow breaks down at high values of transverse momentum $p_\perp \gtrsim 2$ GeV. For such short wavelength components of the QGP, local equilibrium simply cannot be maintained due the fundamental asymptotic freedom property of QCD: the coupling strength becomes too weak.

- The collective flow breaks down at small values of the initial rapidity

density dN_i/dy, where a substantial deviation from the hydrodynamical limit is observed. We remind that lower densities, i.e. lower temperatures, are achieved in small energy or peripheral collisions, as well as at high rapidity $|y|$. This effect is due to the dominant role that hadronic dissipation assumes during the mixed gluonic-hadronic phase, characteristic of temperatures approaching T_c [130].

Initial conditions (from CGC or Glauber models), the equation of state (from lattice computations), the nearly perfect hydrodynamical evolution of the hot and strongly coupled plasma, the diffusive evolution of its late-time hadronic components (from hadronic transport theory), all blend together into powerful numerical codes that can test the validity of any theoretical assumption.

The development of increasingly more complex hydrodynamical models has a story of its own. The simplest versions assume a so called average 1D+1 evolution, where the perfect plasma expands only longitudinally (along the beam axis) and results are computed only in the mid-rapidity region. Initial conditions are smooth as if averaged over multiple collision events, while hadronization, chemical and thermal freeze-out take place at the same time. A more detailed description of this scenario, along with the derivation of the relevant hydrodynamic equations, will be given in Section 5.1.2.

Improvements over this simplistic – yet effective – approach include fluctuation of the initial conditions [131], the calculation of the transverse plasma

expansion, the substitution of perfect hydrodynamics with a real viscous framework, the incorporation of hadronic diffusion processes. These models are called 2D+1 or 3D+1 if they also include rapidity dependence of the collective flow outside the central boost-invariant region [132, 133, 134, 135].

1.2.5 Hadronization and freeze-out

The last stage of quark gluon plasma evolution occurs after the system has cooled down to sufficiently low temperatures for hadronic bound states to form, typically for $\tau \gtrsim 3$ fm/c. It involves two steps:

1. *Hadronization*: the deconfined plasma experiences a phase transition where bound states are formed starting from the outer and colder region of the plasma, known as the corona. This mixed gluonic and hadronic phase coexists while the system continues to expand and until matter has fully hadronized. Two kinds of phenomena take place, recombination and fragmentation, which will be outlined below.

2. *Freeze-out*: elastic and inelastic interactions within the hadronic plasma maintain kinetic equilibrium while attempting to restore chemical one. When the temperature drops below the chemical freeze-out point, the abundance of hadronic species is frozen and chemical interactions are no longer allowed. This picture finds experimental confirmation in the hadron abundance ratio observations [136, 137]. A second freeze-out, kinetical, occurs when the mean free path becomes larger than the

system size and a non-interacting hadron gas is finally formed.

A common way to describe the freeze-out process is given by the Cooper-Frye formalism [138]: the transition from perfect local thermal equilibrium to free streaming of all particles happens along a space-time hypersurface $\Sigma(x)$. The observed momentum distribution is then given by

$$E\frac{dN}{d^3p} \propto \int_\Sigma f(x,p)p\cdot d\Sigma \ , \tag{1.46}$$

where $f(x,p)p\cdot d\Sigma$ represents the local flux of particles with momentum p through the infinitesimal surface $d\Sigma$. The distribution $f(x,p)$ is given by equilibrium Maxwell-Boltzmann statistics with the momentum shifted by the local fluid velocity $u_\mu(x)$.

Recombination

In the low and intermediate $p_\perp$ range, hadrons are mostly formed by recombination/coalescence mechanisms [139, 140, 141]. In this picture, thermal quarks and anti-quarks combine to form mesons and baryons, whose production spectra can be written as

$$E\frac{dN_h}{d^3p} \propto \int_\Sigma p\cdot d\Sigma \int \prod_{i=1}^{n} \left(d^3x_i d^3p_i f(x_i,p_i)\right) W_n(p,x) \ , \tag{1.47}$$

with $f(x_i,p_i)$ representing the phase-space distribution of the constituent q_i or $\bar{q}_i$ and $W_i(p,x)$ representing the Wigner function of the recombined meson ($n=2$) or baryon ($n=3$). Recombination takes place on the hypersurface

Σ_f.

Considering the steep fall off of the momentum distribution function, it is not a surprise that only a limited portion of the constituent phase-space (low $p_\perp$) is densely enough populated to permit any coalescence process to occur. Furthermore, in this scenario, the yield ratio of baryons to mesons observed at a given $p_\perp$ is expected to be enhanced by the lower average momentum that each constituent is required to carry, i.e. $p_\perp/3$ for baryons compared to $p_\perp/2$ for mesons. Confirmation of this effect is found, for instance, in the measurement of the elliptic flow $v_2(p_\perp)$ scaled by the number of quark constituents [142], as reported in Fig 1.13. In fact, it can be shown that

$$\begin{aligned} v_{2,M}(p_\perp) &\simeq 2v_{2,q}(p_\perp/2) \\ v_{2,B}(p_\perp) &\simeq 3v_{2,q}(p_\perp/3) \ . \end{aligned} \tag{1.48}$$

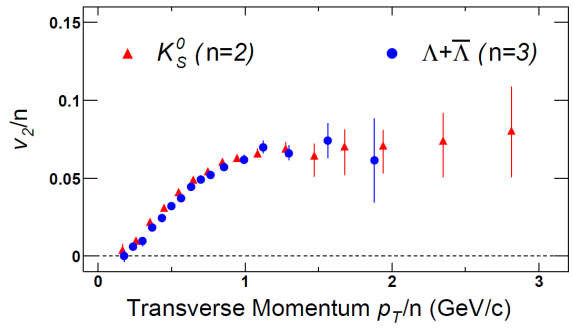

Figure 1.13: The elliptic flow v_2 for K mesons and Λ baryons scaled by the number of constituent quarks n. Taken from [9].

Fragmentation

High $p_\perp$ particles, approximately above 5 GeV, hadronize mostly by fragmentation processes [143, 144]. In this scenario, the parent parton i with momentum p_i fragments into a hadron h with momentum $p_h = zp_i$, $z < 1$:

$$E\frac{d\sigma^h}{d^3p}(p) = \sum_i \int_0^1 \frac{dz}{z^2}\; E_i\frac{d\sigma^{q_i}}{d^3p}\; D^{q_i\to h}(z,Q) \;\;, \tag{1.49}$$

where $E_i d\sigma_i/d^3p_i$ is the production cross-section for the parton i. The fragmentation function $D^{q_i\to h}(z;Q)$ can be interpreted as the probability for the partons i, either quarks or gluons with virtuality Q, to fragment into a hadron h which carries a fraction z of the parton energy. Owing to the factorization theorem in QCD, the soft hadronization mechanism is factorized from the hard scattering process, and is parametrized by the so-called fragmentation functions (FF). The FFs $D^{i\to h}$ are universal, i.e. once derived they are applicable to any process, and they have been studied in detail in e^+e^-, $p\bar{p}$ and pp collisions.

Reflecting the fact that $E_i d\sigma_i/d^3p_i$ has a power-law fall off for high $p_\perp$, the high $p_\perp$ hadron spectrum exhibits a power-law behavior as well.

Melting of Quarkonium

Not all bound states melt as soon as the plasma reaches the critical temperature T_c: whereas the physics of light (u, d, s) quarks is described by the chiral phase transition presented in Section 1.13, the mechanics of heavy

quarks can be approximated by the effective potential model, Eq. (1.5).

When a heavy quark bound state, known as quarkonium, is placed into a hot plasma of deconfined quarks and gluons, color Debye screening will eventually dissolve the binding for sufficiently high temperatures. This transition, however, doesn't need to occur at T_c, and several $c\bar{c}$ and $b\bar{b}$ resonances are known to survive up to two or three times the critical temperature.

A particularly notable consequence of this mechanism is the suppression of the J/Ψ meson, observed at RHIC [145]. From lattice computations [146], the charmonium state is expected to melt only above $T \approx 2\ T_c$ [147]. When the plasma subsequently cools down, the c and $\bar{c}$ quarks are too far apart, on average, to see each other. Unless very high energy densities are achieved, as expected for instance at the LHC, charm thermal production is suppressed by its heavy mass and the contribution to J/Ψ production will be limited or negligible. The charm quarks will instead pair with a light quark to form a D or $\bar{D}$ meson.

A similar pattern holds for other resonances of charmonium, as well as bottomonium states, each of them characterized by a different "melting" temperature. The observation of the suppression, or possibly enhancement, of $c\bar{c}$ and $b\bar{b}$ states serves as a thermometer for the medium.

In turn, heavy-light mesons such as D or B mesons are shown by lattice computations to melt in the plasma already at temperatures above $\approx 1.2\ T_c$ [148, 149]. The survivability of these states at high temperature is therefore compromised and phenomenological effects due to recombination above T_c

expected to be negligible.

1.3 Hard probes

In the previous Section we have studied the formation and evolution of the quark gluon plasma, without explaining in details how its properties can be experimentally verified and measured. If, on one side, we are limited to the observation of final hadronic products, since no direct access to the earlier stages of the plasma is possible, on the other side the possibility to conduct measurements over a broad range of parameters allows us to cross-check theoretical models and checkmate any invalid assumption.

For instance, higher temperatures and energy densities can be achieved by increasing the center-of-mass energy of the collision, asymmetric plasma expansion is obtained in peripheral events, baryon-rich matter is studied at forward rapidities, temperatures are probed by measuring different hadronic species, etc. etc. In particular, during our discussion, we mentioned how lattice QCD predictions and the assumption of a thermalized medium can be confirmed by measuring the flow of bulk particles and comparing with numerical hydrodynamical models. We learned that the measurement of low $p_\perp$ thermal particles gives an insight on the dynamics of the thermalized deconfined plasma.

On the other hand, the measurement of high $p_\perp$, hard particles offers the possibility to probe the plasma using "external" sources, opening the way to

the study of jet-medium interactions and subsequently the indirect verification of several plasma properties. The hard probes that travels through the plasma, in fact, interact with the thermal particles and lose energy through scattering processes that are computable in perturbative QCD [150]. By studying the modification of the high $p_\perp$ hadron spectra attributable to the presence of the medium, it is possible to infer properties such as the coupling strength, screening mass, energy density or transport coefficients of the quark gluon plasma, just to mention a few.

Hard partons are produced during the early stages of the collisions, as a result of hard scattering processes between the colliding nuclei. They travel through the medium interacting weakly with the thermal quarks and gluons, and finally fragment into a stream of hadrons known as jets. The QCD computation of hard scattering processes rely on the factorization theorem [151] to separate the soft non-perturbative scales of the problem (parton distribution functions, fragmentation functions) from the hard perturbative ones (scattering cross sections).

The parton distribution functions (PDF), $f_{i,n}(x_i, Q^2)$, are defined as the probability that a nucleon n with momentum p contains a parton i which is carrying the fractional momentum $x_i p$, $0 \leq x_i \leq 1$. Similarly to the fragmentation functions introduced earlier in Section 1.2.5, the PDFs are considered universal and determined experimentally in deep inelastic lepton-nucleon scattering events. The method of extracting the PDFs from experi-

mental data is well established in the case of the proton: the non-perturbative distributions are parametrized at some Q^2 initial scale and evolved to higher scales according to the Dokshitzer-Gribov-Lipatov-Altarelli-Parisi (DGLAP) equations [152, 153, 154].

The dependence of the hadronic PDFs on x and Q^2 was shown earlier in Fig. 1.8: for $x \to 0$, the PDFs are increasingly dominated by sea-quarks and gluons. On the contrary, the Q^2 dependence is almost flat at fixed x (scaling), except for very small values of x, when the PDFs develop a logarithmic Q^2 dependence (scaling violation).

In high energy nuclear collisions, high $p_\perp$ particles are produced as a result of hard (large Q^2) scatterings between the colliding nucleons' constituents. The accurate parametrization of the PDFs is therefore essential in order to calculate the momentum distribution of the hard partons. The common assumption is to approximate the incoming nuclei as incoherent superpositions of constituent nucleons, and consider in turn the collision as an incoherent superposition of nucleon-nucleon (p+p) impacts.

1.3.1 Nuclear effects

Hard partons produced in heavy ion (A+A) collisions are subject to nuclear effects which can be divided in two categories:

- *Initial or cold state effects*: effects that act on the initial momentum

distribution of partons, which is modified with respect to the same rescaled distribution obtained in p+p collisions. These effects are due to the modification of the PDFs inside the nucleus, and are visible in nucleus-nucleon (p+A) events.

- *Final or hot state effects*: effects directly ascribable to the presence of a hot deconfined medium such as the quark gluon plasma, only visible in A+A reactions. Modifications to the observed hadronic distribution due to hot state effects can be used to determine several properties of the QGP, provided that initial state effects have been correctly singled out and the initial hard parton distributions are accurately known.

Shadowing

The difference between free and bound nucleon PDFs can be measured by defining the nuclear ratio

$$R^A_{F_2}(x,Q^2) = \frac{F_2^A(x,Q^2)}{A\ F_2^{nucleon}(x,Q^2)}\ , \tag{1.50}$$

where $F_2(x,Q^2)$ are called structure functions and A, as usual, indicates the nuclear mass number. Since the structure functions are function of the PDFs, visible nuclear effects in the ratio $R^A_{F_2}$ directly apply to the parton distributions. The results shown in Fig. 1.14 identify four separate regions where these effects take place:

- *shadowing*: $R^A_{F_2} < 1$ for $x \lesssim 0.1$

- *antishadowing*: $R_{F_2}^A > 1$ for $0.1 \lesssim x \lesssim 0.3$
- *EMC*: $R_{F_2}^A < 1$ for $0.3 \lesssim x \lesssim 0.8$
- *Fermi motion*: $R_{F_2}^A > 1$ for $x \gtrsim 0.8$

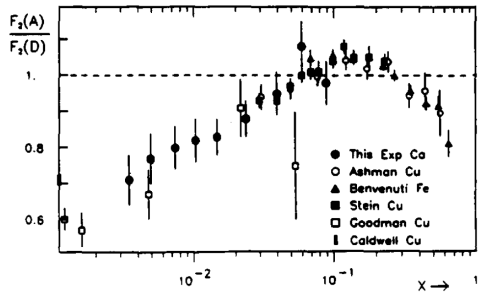

Figure 1.14: Results for $R_{F_2}^A$ for different nuclear species, taken from [10].

A unique theoretical description of these effect is missing, and several mechanisms are instead believed to be responsible. The depletion of partons (shadowing) in the low x kinematic region is particularly relevant to our case since experiments at RHIC and LHC probe the physics of nuclear collisions at increasingly higher energies and smaller x. Such depletion, in turn, leads to an observable reduction of the hadron yield in the high $p_\perp$ region.

Known features of the shadowing effect [155] comprise: (i) an increase of shadowing with decreasing x, although at very small x experimental data is compatible with either saturation or even a mild decrease; (ii) an increase of shadowing with A; (iii) a decrease of shadowing with increasing Q^2.

Several phenomenological explanations of shadowing have been proposed [156, 157, 158, 159]. Underlying is the concept of gluon fusion and gluon

saturation which occurs at very low x for very dense systems [160], a phenomenon addressed theoretically in the CGC framework presented in Section 1.2.1.

Cronin

The Cronin effect [161] refers to the enhancement of the production cross section of hadrons in p+A compared to p+p collisions, experimentally observed in the transverse momentum range $1 < p_\perp < 7$.

This effect can be studied in a model of multiple parton scattering [162], where the incident partons undergo multiple soft scatterings prior to the hard one, while passing through the target nucleus A. Each of the subsequent scatterings provide a transverse momentum $k_\perp$ kick which broadens the $k_\perp$ gaussian distribution of the beam partons by a factor $\langle \Delta k_\perp^2 \rangle_A$:

$$g_A(k_\perp) = \frac{1}{\pi \langle k_\perp^2 \rangle_A} \mathrm{e}^{-k_\perp^2 / \langle k_\perp^2 \rangle_A} \quad , \tag{1.51}$$

with width $\langle k_\perp^2 \rangle_A = \langle k_\perp^2 \rangle + \langle \Delta k_\perp^2 \rangle_A$. The broadening is assumed to be proportional to the number of scatterings the projectile suffers inside the nucleus. Contrasting the $k_\perp$ broadening is interference absorption between successive scatterings. The two effects combined lead to an enhancement of the hadron yield in a specific region of the transverse momentum $p_\perp$ space.

The Cronin effect is visible also in A+A collisions, as will be shown later in Chapter 6.

Energy loss

Energy loss is a final state effect, and is experienced by hard partons (jets) that interact weakly with the thermal particles [150, 163]. Both elastic and inelastic collisions take place [164, 165], leading to gluon radiation as the equivalent form of bremsstrahlung in a color plasma.

The knowledge of how the hadron distribution would look like *if* there were no interactions between the probe and the hot deconfined medium allows us to measure the properties of the quark gluon plasma by observing the modified hadron distribution in A+A reactions.

This approach, often referred to as *jet tomography*, relies upon the correct understanding of the interaction mechanism(s) between the jets and the plasma. Our work expands upon one of the most well-known theoretical frameworks, the Gylassu-Levai-Vitev opacity expansion [164, 166], and attempts to build a solid phenomenological, numerical model, CUJET, which will allow accurate comparison between theoretical predictions and experimental data.

The results are presented in a self-consistent fashion in Chapter 6. In the next Chapters 2 and 3 we introduce the GLV energy loss model, while Chapters 4 and 5 focus on the development of CUJET.

Chapter 2

Energy loss

Assuming factorization of scales, the interactions between the jet and the plasma can be isolated from the initial and final states of the collisions and treated perturbatively. In the past decade, several models of jet quenching have been formulated in the framework of pQCD and applied to explain or predict high $p_\perp$ measurements at RHIC and LHC, regardless of whether the thermal properties of the medium can be treated in the same perturbative way.

Jet quenching is referred to as the collisional process between hard partons and thermal quanta that results into a loss of energy of the original parton, either by elastic or inelastic (radiative) mechanisms.

Purely elastic collisions in a color medium, originally described in [150], were subsequently found to play a relevant role especially in the case of heavy quark jet quenching [167, 168, 169]. An in-depth analysis of the elastic

contribution to the energy loss was performed by Wicks in [170], and the implementation into our CUJET model will be descried in Chapter 4. In the present Chapter, we will instead focus on the inelastic processes that give origin to gluon radiation.

2.1 Radiative energy loss models

Even though all proposed radiative models share the same pQCD framework, differences arise in the basic underlying assumptions about the medium and its interaction with the hard partons. Four distinct models can be identified in the literature:

- *Multiple soft scattering (BDMPS-Z and ASW)* [171, 172, 173, 174, 175, 176, 177, 178, 179, 180, 165] and [181, 182, 183]: The plasma is modeled by a series of static colored scattering centers, whose density decreases while the plasma expands. The incoming parton is subject to Brownian motion in the transverse plane due to multiple soft scatterings with the medium. The plasma is fully characterized by the transport coefficient $\hat{q}$, which is the mean of the squared transverse momentum exchanged per unit path length.

- *Opacity expansion (GLV)* [184, 185, 186, 166, 187, 188, 164, 189]: Similarly to BDMPS-Z, the plasma is modeled by a series of static (or dynamic, cf. Chapter 4) scattering centers. The energy loss is formulated as an expansion in the number of parton-medium scatterings

(opacity expansion), dominated by the first hard contribution. In contrast to the previous model, the GLV also includes the power-law tail of the scattering cross section. The plasma is described by the density of scattering centers ρ and a Debye screening mass μ_D, which can in turn be expressed as a function of the temperature $T(\rho)$ (cf. Eq. (1.34)).

- *Higher twist (HT)* [190, 191, 192]: The medium is formulated in terms of matrix elements of gauge field operators, and the properties of the plasma are specified by the entropy density s.

- *Finite temperature field theory (AMY)* [193, 194, 120, 195, 196, 197, 198]: The medium, characterized as a thermally equilibrated plasma, is described in the context of finite temperature field theory using the Hard Thermal Loop approximation. All properties of the plasma are specified by its temperature T and baryochemical potential μ_B.

Comprehensive reviews on the subject of Jet Quenching exist, such as [199, 200, 201], as well as detailed quantitative comparisons among the four energy loss models [202, 19].

It should be noted that the differences among these models are not limited to the medium assumptions, but extend to the inclusion of specific features of gluon induced radiation. In particular, it is shown in [202] that the largest quantitative discrepancies arise from the way approximations are carried out throughout the calculations and, most importantly, how specific kinematic limits are enforced.

We present first a list of the most notable features of gluon radiation:

Vacuum radiation

A high $p_\perp$ parton produced in a hard collision is generally characterized by high virtuality. Even in the vacuum, it will radiate gluons in order to reduce its "off-shellness", a process known as vacuum splitting. The question naturally arises whether this spectrum is altered by induced radiation once medium effects are taken into consideration.

In hadron-hadron collisions, the gluon radiation spectrum obtained from the interaction between the jet and the plasma is asymptotically described by the Gunion-Bertsch incoherent limit [163], presented later in Section 2.2.

It turns out, however, that interference effects between production, or vertex, radiation and induced radiation play a dominant role, as clearly demonstrated in the context of the opacity expansion and as explicitly shown in the next Chapter.

LPM effect

A gluon radiated by a quark takes a finite amount of time to be "resolved", called formation time τ_f. Especially for gluons emitted longitudinally along the path of the parent parton (small angle scattering), τ_f can reach significant values often larger than the mean free path λ.

When this occurs, interference takes place among successive scatterings in

the medium, suppressing the overall induced spectrum. This effect, referred to as the Landau-Pomeranchuck-Migdal (LPM) effect [184, 203], plays a crucial role in the computation of the energy loss, which then grows quadratically with the size of the plasma L, rather than linearly as in the case of incoherent scatterings.

Kinematic limits

Common kinematic approximations made by all energy loss models include:

- Eikonal approximation: both the parton energy E and the emitted gluon energy ω are much larger than the transverse momentum exchanged with the medium $q_\perp \equiv |\mathbf{q}|$[1]: $E \gg q_\perp$ and $\omega \gg q_\perp$. Most of the models also assume $E \ll \omega$ (soft approximation).

- Collinear radiation: Gluons are emitted at small angles with respect to the parent parton: $\omega \gg k_\perp$, where $k_\perp \equiv |\mathbf{k}|$ represents the transverse[2] momentum of the gluon.

- Discrete scattering centers: the mean free path λ is much larger than the Debye screening length $1/\mu_D$, $\lambda \gg 1/\mu_D$.

---

[1] In our notation, $\mathbf{q}$ represents the transverse momentum components of the three dimensional vector $\vec{\mathbf{q}}$

[2] $k_\perp$ indicates the plane transverse to the parent parton's momentum, which is itself transverse to the beam axis.

Even though the results are strictly valid only within the range of approximations specified above, the common way to proceed is to extrapolate the computation to the forbidden regions, for instance by integrating the radiation spectrum up to large angles $k_\perp \sim \omega$, or by letting $\omega \sim E$ [204].

This procedure inevitably leads to unphysical results that must be interpreted and possibly corrected. In the next Chapter we will numerically address most of these issues.

Multiple gluon emission

On average, more than one gluon is emitted as the result of the interaction between the jet and the medium.

The simplest procedure, implemented by the opacity expansion model, is to sum the emissions incoherently assuming the number of radiated gluons follows a Poisson distribution [188].

2.2 Gunion-Bertsch incoherent radiation

The reference for any medium-induced radiative jet energy loss computation is the incoherent asymptotic Bertsch-Gunion spectrum [163], which represents the non-abelian (QCD) equivalent of the Bethe-Heitler formula in QED [205]. It assumes no interference effects among successive scatterings of the light parton traveling through the plasma (incoherent), and considers the incoming jet on-shell (asymptotic), thus neglecting further interference

between the vertex and induced radiation.

In this limit, the radiated gluon multiplicity distribution, differential in x and $\mathbf{k}$ (respectively fractional energy carried away by the radiated gluon, $x = \omega/E$, and gluon transverse momentum), is given by

$$\frac{dN_g}{dxd\mathbf{k}} \cong \frac{C_A\alpha_s}{\pi^2}\frac{1}{x}\frac{\mathbf{q}^2}{\mathbf{k}^2(\mathbf{q}-\mathbf{k})^2} \quad , \tag{2.1}$$

with C_A the quadratic Casimir operator in the adjoint representation. Eq. 2.1 shows the existence of a central region uniform in rapidity[3], i.e. a plateau, and a spectrum that falls as $1/k_\perp^4$ at large $k_\perp$.

The integration over $\mathbf{q}$ is performed after choosing a parametrization for the distribution of medium-induced transferred momenta. Here we will use the normalized distribution derived from the Gyulassy-Wang model (cf. Section 2.3.1)

$$\frac{d\sigma}{d\mathbf{q}} = \frac{1}{\pi}\frac{\mu^2}{(\mathbf{q}^2+\mu^2)^2} \quad . \tag{2.2}$$

As usual, the bold vectors $\mathbf{q}$ and $\mathbf{k}$ represent 2D vectors in the plane transverse to the jet direction, while $\mu \equiv \mu_D$ is the Debye screening mass of the plasma.

In order to screen the $\mathbf{k} \to \mathbf{q}$ and $\mathbf{k} \to 0$ infrared divergences, a physical soft $\mathbf{k}$ scale χ needs to be determined, which is related to the dynamically

[3]After performing the transformation $x\frac{d}{dx} = \frac{d}{d\eta}$, where η is the rapidity of the gluon

generated mass that the gluon acquires in a thermal plasma (see Chapter 1 for more details). The incoherent asymptotic radiation spectrum for a given plasma length L and mean free path λ is then given by

$$\frac{dN_g}{dxd\mathbf{k}} = \frac{C_A\alpha_s}{\pi^2}\frac{1}{x}\frac{L}{\lambda}\int d\mathbf{q}\frac{\mu^2}{\pi(\mathbf{q}^2+\mu^2)^2}\frac{\mathbf{q}^2}{(\mathbf{k}^2+\chi^2)((\mathbf{q}-\mathbf{k})^2+\chi^2)} \quad . \tag{2.3}$$

2.3 Opacity order expansion

The opacity order expansion is a formalism developed by Gyulassy, Levai and Vitev (GLV) [185, 166], based on an earlier work of Gyulassy and Wang [184]. The expression of the partonic energy loss is expanded in powers of the opacity L/λ, where L indicates the size of the plasma and λ the mean free path of the parton.

In practice, this means to consider only one scattering between the parton and the medium at first order, two scatterings at second order and so forth. This is often referred to as a thin plasma approximation, valid for small values of the opacity, as opposed to the thick plasma approximation characteristic of the multiple soft scattering limit. The interaction is modeled according to a Debye screened potential with screening mass μ, which is considered a fundamental property of the plasma along with the density ρ. Since the GLV includes the power-law tail of the scattering cross section, large momentum transfer (hard) scatterings are taken into account as well.

The kinematic assumptions made in the GLV model are listed in Section

2.1 and consist of the soft eikonal approximation. Namely, this means that the parent parton has sufficiently high energy such that its path is approximately straight. The gluon, which is radiated at small angles, doesn't carry away a significant portion of the original parton energy, with the consequence that the latter is not dynamically updated during the multiple scattering process.

Several aspects of gluon radiation mentioned above are included in the opacity order expansion, most notably the interference effects between vertex and induced radiation, as well as gluon rescattering in the plasma. All combined, these effects lead to an expression for the double-differential gluon multiplicity distribution in x (fractional gluon energy) and $k_\perp$ (gluon transverse momentum), which is later integrated to give the energy loss of the parent parton. The last passage is strictly valid only if one assumes that no further exchange of energy with the medium takes place.

2.3.1 Gyulassy-Wang model

In [184], the authors introduce a color screened potential $V_i^a(\vec{\mathbf{q}})$ to model the interaction with a static target parton (scattering center) localized at $\vec{\mathbf{x}}_i$ and carrying color c:

$$V_i^a(\vec{\mathbf{q}}) = g(T_i^a)_{c,c'} \frac{\mathrm{e}^{-i\vec{\mathbf{q}}\cdot\vec{\mathbf{x}}_i}}{(\vec{\mathbf{q}}^2 + \mu^2)} \quad , \tag{2.4}$$

where T_i^a is a generator of $SU(3)$ corresponding to the representation of the target parton i. In the high temperature static approximation, the average energy loss $q_0 \sim q_z \sim g^2 T$ can be neglected compared to the average transverse momentum transfer $q_\perp \sim \mu \sim gT$. Also, at high T the mean free path $\lambda \sim 1/g^2 T$ is much larger than the screening length $1/\mu \sim 1/gT$ and the scattering centers are assumed well separated.

The amplitude for an incoming jet with four momentum p_{i-1}^μ to scatter to p_i^μ, in the potential centered at $\vec{\mathbf{x}}_i$, is then proportional to

$$M_i(p_i, p_{i-1}) \propto \delta(p_i^0 - p_{i-1}^0) g T^a V_i^a(\vec{\mathbf{p}}_i - \vec{\mathbf{p}}_{i-1}) \ , \tag{2.5}$$

where T^a is a generator corresponding to the representation of the incoming parton.

If we denote an intermediate jet parton propagator by $\Delta(p)$, the amplitude for multiple elastic collisions takes the form

$$\begin{aligned} M_{ji}(p_j, p_{i-1}) \propto \int d^4 p_{j-1} d^4 p_i \ M_j(p_j, p_{j-1}) \\ \times \Delta(p_{j-1}) \cdots \Delta(p_i) M_i(p_i, p_{i-1}) \ , \end{aligned} \tag{2.6}$$

whereas the amplitude for radiating a gluon with four momentum k, polarization vector ϵ_μ and color c, at the mth intermediate jet line, becomes

$$\begin{aligned} M^c_{ji;m}(p_j, p_{i-1}; k) \propto \int d^4 p_m \ M_{j,m+1}(p_j, p_m - k) \\ \times \{\Delta(p_m - k)(g \epsilon_\mu p_j^\mu T^c) \Delta(p_m)\} M_{m,i}(p_m, p_{i-1}) \ . \end{aligned} \tag{2.7}$$

The latter expression represents a jet which undergoes multiple scatterings in the medium and radiates a gluon (radiation from internal jet lines). However, it is also possible for the radiated gluon to scatter multiple times with the medium (radiation from internal gluon lines), adding another set of amplitudes that include three gluon vertices and correspond to multiple final state interactions of the emitted gluon (cascading). If the intermediate gluon lines are set on shell, the cascading becomes classical and the only effect is the broadening of the final $k_\perp$ radiation distribution.

In the eikonal limit, we report the total radiation amplitude for n scatterings, Eq. (57-59) of [184]:

$$\begin{aligned} M_n^c(p_n, p_0; k) \propto & (g)^n \int \prod_{m=1}^{n} \left[d\mathbf{q}_m \, \mathrm{e}^{-ik\mathbf{q}_m \cdot \mathbf{x}_m} V_m^{a_m}(\mathbf{q}_m) \right] \\ & \times \left(\epsilon \cdot \mathbf{J}^c_{a_1 \cdots a_n}(\mathbf{q}_1 \cdots \mathbf{q}_n; k) \right) \quad , \end{aligned} \tag{2.8}$$

where the effective color current is

$$\begin{aligned} \mathbf{J}^c_{a_1 \cdots a_n}(\mathbf{q}_1 \cdots \mathbf{q}_n; k) = & 2ig \sum_{i=1}^{n} \mathrm{e}^{ikx_i} \left(\frac{\mathbf{k}}{\mathbf{k}^2} + \frac{\mathbf{q}_i - \mathbf{k}}{(\mathbf{q} - \mathbf{k})^2} \right) \\ & \times (T^{a_n} \cdots [c, T^{a_i}] \cdots T^{a_1}) \quad . \end{aligned} \tag{2.9}$$

From this expression, one can obtain the spectrum of soft induced gluon bremsstrahlung as the modulus square of the amplitude averaged over initial and summed over final colors and polarizations. The result is the coherent analogous of Eq. 2.3, which is recovered in the limit $m = 1$.

The interference LPM effect among subsequent scatterings makes its appearance in the phase factors of Eq. 2.9: when squared, $|J|^2$ gives rise to m diagonal terms where the phase factors drop out, and $m(m-1)$ off-diagonal terms where the phase factors take the form $\exp\left(ik(x_i - x_j)\right)$. Three limiting regions can be identified:

- Incoherent limit, $k(x_i - x_j) \gg 1$: the off-diagonal phase factors average to zero and the incoherent Gunion Bertsch limit is recovered.

- Factorization limit, $k(x_i - x_j) \ll 1$: the phase factors are approximately unity, adjacent terms in the sum cancel out and only radiation from the initial and final lines contribute.

- LPM limit: the parameters controlling interference effects are the gluon formation time τ_f and the mean free path λ, i.e. average distance between scattering centers:

$$\begin{aligned} k \cdot (x_i - x_j) &= \omega(x_i^0 - x_j^0) - k_z(z_i - z_j) - \mathbf{k}(\mathbf{x}_i - \mathbf{x}_j) \\ &\approx (\omega - k_z)(z_i - z_j) \equiv \frac{1}{\tau_f(k)}\lambda \ . \end{aligned} \tag{2.10}$$

  In the collinear approximation, $\mathbf{k} \ll \omega$, k_z, and

$$(\omega - k_z) \simeq \frac{k_\perp^2}{2\omega} \equiv \frac{1}{\tau_f(k)} \ . \tag{2.11}$$

  If $L \ll \lambda$ is the size of the medium, we can immediately see that interference effects are dominant in the region $\lambda < \tau_f < L$, whereas

the incoherent and factorization limits are obtained in the regions $\tau_f < \lambda < L$ and $\lambda < L < \tau_f$ respectively.

2.3.2 GLV

Built upon the foundations of the Gyulassy-Wang potential, the GLV opacity expansion model includes interference effects with the vertex radiation and among subsequent scatterings of the radiated gluon (quantum cascade). The model is derived as a series expansion in the opacity L/λ, which provides an expression of the all-orders result in closed form. While the analytical evaluation of the integrals is possible only at first order in opacity, the numerical evaluation is performed iterating from order to order.

An extension of the GLV model which includes massive quarks kinematic effects as well as plasmon mass for the gluons was developed by Djordjevic and Gyulassy in [187] (DGLV). The full derivations are found in the original papers [185, 166, 187]. Here we will only report the main results and provide their physical interpretation.

In the soft eikonal kinematics used to derive DGLV, the incoming jet, gluon and exchanged four momenta read

$$\begin{aligned} p &= (E, E, 0) = [2E, 0, 0] \\ k &= (\omega = x_E E, \sqrt{(x_E E)^2 - \mathbf{k}}, \mathbf{k}) = [x_+ E^+, \tfrac{\mathbf{k}^2}{x_+ E^+}, \mathbf{k}] \\ q &= (q_0, q_z, \mathbf{q}) \ , \end{aligned} \tag{2.12}$$

where parenthesis and square brackets respectively denote Minkowski and light-cone coordinates. In the pure eikonal limit, the gluon fractional energy x_E and fractional plus-momentum x_+ coincide, and corrections need to be made for finite emission angles (see Section 3.3.1 in the next Chapter for more details). Also, in the static scattering center approximation $q_0 \sim q_z \ll \mathbf{q}$. In the above expressions we suppressed the effective gluon plasmon mass, denoted by $m_g = \mu/\sqrt{2}$, and the parton mass M.

The double-differential gluon multiplicity distribution in x and $k_\perp$, for $n = 1$ single scattering in the medium, is then given by

$$\begin{aligned}\frac{dN_g^{n=1}}{dxd\mathbf{k}} = \frac{C_R\alpha_s}{\pi^2}\frac{1}{x}\left(\frac{L}{\lambda_g}\right)\int d\mathbf{q}\frac{\mu^2}{\pi(\mathbf{q}^2+\mu^2)^2} \\ \times\ \frac{-2(\mathbf{k}-\mathbf{q})}{(\mathbf{k}-\mathbf{q})^2+\chi^2}\left(\frac{\mathbf{k}}{\mathbf{k}^2+\chi^2}-\frac{(\mathbf{k}-\mathbf{q})}{(\mathbf{k}-\mathbf{q})^2+\chi^2}\right) \\ \times\ \left(1-\cos\left(\frac{(\mathbf{k}-\mathbf{q})^2+\chi^2}{2xE}\Delta z_1\right)\right)\ .\end{aligned} \tag{2.13}$$

Here $\chi^2 = M^2x^2 + m_g^2(1-x)$, $\Delta z_1 = z_1 - z_0$ and represents the distance between the scattering points z_1 and z_0 (production vertex), C_R is the quadratic Casimir of the jet ($C_F = 4/3$ for quark jets, $C_A = 3$ for gluon jets), and $\alpha_s = g^2/4\pi$. Note that the opacity is written in terms of the gluon rather than the jet mean free path, λ_g, thanks to a simplification in the color algebra known as 'color triviality'.

The extension to multiple scatterings, instead, is formulated as

$$\begin{aligned}\frac{dN_g^n}{dxd\mathbf{k}} = \frac{C_R\alpha_s}{\pi^2}\frac{1}{x}\frac{1}{n!}\left(\frac{L}{\lambda_g}\right)^n \int\prod_{i=1}^{n}\left(d\mathbf{q}_i\left(\frac{\mu^2}{\pi(\mathbf{q}_i^2+\mu^2)^2}-\delta^2(\mathbf{q}_i)\right)\right) \\ \times\ -2\,\mathbf{C}_{(1\cdots n)}\cdot\sum_{m=1}^{n}\mathbf{B}_{(m+1\cdots n)(m\cdots n)} \\ \times\ \left(\cos\left(\sum_{k=2}^{m}\Omega_{(k\cdots n)}\Delta z_k\right)-\cos\left(\sum_{k=1}^{m}\Omega_{(k\cdots n)}\Delta z_k\right)\right)\ .\end{aligned} \tag{2.14}$$

The radiated spectrum is expressed in terms of 'Cascade', 'Hard' and 'Gunion-Bertsch' terms:

$$\begin{aligned}\mathbf{C}_{(1\cdots n)} &= \frac{\mathbf{k}-\mathbf{q}_1-\cdots-\mathbf{q}_n}{(\mathbf{k}-\mathbf{q}_1-\cdots-\mathbf{q}_n)+\chi^2} \\ \mathbf{H} &= \frac{\mathbf{k}}{\mathbf{k}^2+\chi^2} \\ \mathbf{B}_{(i)} &= \mathbf{H}-\mathbf{C}_{(i)} \\ \mathbf{B}_{(1\cdots m)(1\cdots n)} &= \mathbf{C}_{(1\cdots m)}-\mathbf{C}_{(1\cdots n)}\ ,\end{aligned} \tag{2.15}$$

where $\sum_2^1 \equiv 0$ and $\mathbf{B}_{(n+1\cdots n)(n)} \equiv \mathbf{B}_{(n)}$ is understood. The inverse of formation time Ω is given by

$$\Omega_{m\cdots n} = \frac{(\mathbf{k}-\mathbf{q}_m-\cdots-\mathbf{q}_n)+\chi^2}{2xE}\ , \tag{2.16}$$

and regulates the LPM interferences seen in the phases of Eq. 2.9, here written in cosine form.

The relevant terms in (2.14) are: (1) the opacity $\frac{1}{n!}\left(\frac{L}{\lambda_g}\right)^n$; (2) the effective interaction potential $\left(\frac{\mu^2}{\pi(\mathbf{q}_i^2+\mu^2)^2}-\delta^2(\mathbf{q}_i)\right)$; (3) the radiation antenna

$\left(\mathbf{C}_{(1\cdots n)} \cdot \sum_{m=1}^{n} \mathbf{B}_{(m+1\cdots n)(m\cdots n)}\right)$; (4) the LPM phases $\left(\cos\left(\sum_{k}^{m} \Omega_{(k\cdots n)} \Delta z_k\right)\right)$.

The opacity term takes into account the combinatorial probability of hitting n different centers in the plasma,

$$\frac{N!}{n!(N-n)!} \approx \frac{N^n}{n!} \quad . \tag{2.17}$$

The interaction potential has the form of the Debye screened Gyulassy-Wang potential, Eq. (2.4), minus a forward scattering unitarity correction $\delta^2(\mathbf{q})$. The antenna terms determine the shape of the transverse radiation distribution, but it is from the LPM phases that we draw the most interesting conclusions. Depending on the magnitude of the phases, one can observe a more oscillatory behavior corresponding to the incoherent limit (large phases), or an approximate cancellation leading to coherence LPM effects (small phases). This result becomes obvious in the $n = 1$ case, where the LPM term $(1 - \cos(\Delta z/\tau_f))$ contains information on the phases of the production vertex and of the scattering point.

The total energy ΔE carried away by the emitted gluons is obtained by integrating the radiation spectrum, Eq. (2.14). Assuming no further interaction of the jet in the medium, this is readily interpreted as the energy quenching that the jet suffers propagating through a hot deconfined plasma.

$$\frac{\Delta E}{E} = \int dx \int d\mathbf{k}\; x \frac{dN_g^n}{dx d\mathbf{k}} \quad . \tag{2.18}$$

A straightforward analytic computation, in first order in opacity and assuming no kinematic boundaries on the $d\mathbf{q}$ and $d\mathbf{k}$ integrations, leads to the asymptotic result

$$\frac{\Delta E}{E} = \frac{C_R \alpha_s}{4} \frac{L^2 \mu^2}{\lambda_g} \frac{1}{E} \log \frac{E}{\mu} \quad . \tag{2.19}$$

We immediately notice the quadratic dependence of the energy loss on the size of the medium L, characteristic of the LPM regime as opposed to the linear dependence of incoherent emission.

2.3.3 Multiple gluon emission

The DGLV integral, Eq. (2.14), is constructed starting from diagrams with only one external gluon line; multiple gluon emission can be calculated by repeating the single gluon emission kernel in a incoherent fashion.

The simplest procedure for multiple gluon emission is the Poisson ansatz, where the number of emitted gluons follows a Poisson distribution, with the mean number $\overline{N}$ given by the integral of the gluon emission spectrum $\overline{N} = \int dx \frac{dN_g}{dx}(x)$. After all, gluon radiation can be thought of as a stochastic event, and it makes sense to speak of a probability distribution $P(\epsilon)$ of radiating a certain amount of energy $\epsilon \equiv \Delta E/E$:

$$P(\epsilon) = P_0 \delta(\epsilon) + \tilde{P}(\epsilon)|_0^1 + P_1 \delta(1-\epsilon) \tag{2.20}$$

The probability distribution is split in three components: the first term corresponds to the probability of zero radiation, $P_0 = \mathrm{e}^{-\overline{N}}$. The second term is given by

$$\tilde{P}(\epsilon) = \sum_{n=1}^{\infty} P_n(\epsilon) \ , \tag{2.21}$$

with

$$\begin{aligned} P_1(\epsilon) &= P_0 \frac{dN_g}{dx}(\epsilon \equiv x) \\ P_{n+1}(\epsilon) &= \frac{1}{n+1} \int_0^1 dx_n P_n(\epsilon - x_n) \frac{dN_g}{dx}(x_n) \end{aligned} \tag{2.22}$$

The third and last term represents instead the probability of total quenching. In the soft approximation, the radiated energy ω is assumed much smaller than the initial jet energy E, and $x \ll 1$. Consequently, the energy of the outgoing parton E' is approximately equal to E. When the $\{x_n\}$ are integrated up to the kinematic limit $x_n = 1$, a "leakage" error into the unphysical region $\tilde{P}(\epsilon > 1) \neq 0$ occurs, and this error is calculated in $P_1 = \int_1^{\infty} d\epsilon \ \tilde{P}(\epsilon)$.

2.3.4 Multiple soft scattering

One of the main motivations that led to the development of the full opacity series (D)GLV was to interpolate between the 'thin' ($n = 1$) and 'thick' ($n = \infty$) plasma approximations, the former obtained assuming a single hard parton scattering and the latter obtained assuming an infinite number of soft scatterings in the medium.

The authors of BDMPS [172, 173] were the first to study the induced

radiation x-spectrum in the multiple soft scattering (MSS) approximation. Assuming the medium is thick enough, $L \gg \lambda$, the parton is expected to perform a Gaussian diffusion in the transverse momentum space.

An alternative way to derive the BDMPS result is to use the path integral formalism for jet energy loss, originally developed by Zakharov in [176, 177] and later cast in a numerically more pragmatic form in [181]. In this formalism, the radiated gluon x- and $k_\perp$-spectrum are expressed as a path integral over the transverse deviation $\mathbf{r}$ from a straight-line propagation, and the MSS limit can be achieved making a dipole approximation. The product of the density of scattering centers and the dipole cross section is approximated by $n(z)\sigma(\mathbf{r}) \approx \frac{1}{2}\hat{q}(z)\mathbf{r}^2$, introducing the transport coefficient $\hat{q}$ which is used as a parameter to characterize the medium.

Starting from a Schrodinger equation, Wicks shows in [170] the equivalence of the BDMPS, Zakharov and GLV opacity series approaches as different approximations to the same multiple scattering theory.

In the MSS limit, $\hat{q}$ is a function of the position z, or similarly of time, and controls both the x- and $k_\perp$-distributions of the induced radiation. As a transport coefficient, $\hat{q}$ represents the average transverse momentum squared transferred to the parton per unit path length, and is analogous in the GLV formalism to $\hat{q} \sim \mu^2/\lambda$.

If one ignores finite kinematic bounds on the transverse momentum and integrates the MSS radiated gluon distribution over $k_\perp$, the BDMPS induced

intensity x-spectrum takes the form

$$\omega\frac{d}{d\omega}(I - I_{vacuum}) = \frac{\alpha_s}{\pi}xP_{p\to g}(x)\log\left|\cos\sqrt{-iz}\right| \quad , \tag{2.23}$$

where $P_p \to g(\mathrm{x})$ is the splitting function and z is a function of x and $\hat{q}$, defined as

$$z \equiv |\omega_0^2|L^2 \quad , \quad \omega_0^2 = -i\frac{((1-x)C_A + x^2C_R)\,\hat{q}}{2x(1-x)E} \quad . \tag{2.24}$$

For small x, one has $z \sim \hat{q}L^2/\omega \sim L/\tau_f$. In [206], the author Taylor expands Eq. (2.23) in z and interprets the result as an opacity series:

$$\log\left|\cos\sqrt{-iz}\right| = \frac{1}{12}z^2 - \frac{17}{2520}z^4 + \frac{691}{935550}z^6 - \cdots \quad . \tag{2.25}$$

The scaling with z predicted by (2.23), nevertheless, was shown in [206] and [207] to be violated up to 100%, possibly indicating that the energy loss spectrum at intermediate opacity depends in detail on both the screening mass μ and mean free path λ, rather than just the ratio $\hat{q} \sim \mu^2/\lambda$. The Taylor expansion (2.25), moreover, misses the first order in opacity contribution which is the leading term in the GLV opacity series.

Calculations reported in [208], which include the kinematic limits neglected above, could fit the experimental data only by using a $\hat{q}$ value bigger than the one expected by $\hat{q} \sim \mu^2/\lambda$. As presented in later Chapters, the full GLV solution without the MSS approximation can fit the data with much

more physical opacity parameters.

The necessity to develop a numerical algorithm capable of extending the computation of the GLV series to intermediate opacity is therefore essential in order to draw quantitative conclusions from jet quenching measurements at RHIC and LHC. This will be the main subject of the next Chapter, along with a detailed phenomenological analysis of the features of DGLV.

Chapter 3

Radiated gluon distribution

Despite its seemingly crude approximation, a brick plasma setup – characterized by length L and uniform density and temperature – offers a simple yet effective way to test the mechanics of jet energy loss in a strongly coupled quark gluon plasma. In this Chapter, we will present results relative to radiative losses in such simplistic scenario, with the intent of probing in greater details the main features of the opacity series expansion.

In Section One, we analyze the numerical algorithm that performs the computation of the DGLV series to arbitrary order in opacity. In Section Two and Three we study the induced transverse radiation spectrum in a uniform plasma brick, with particular attention to the quark mass dependence and the convergence of the opacity series.

In section Four we concentrate on the integrated gluon distribution and

the energy loss suffered by different flavor jets in the plasma. The equivalence between light and charm quarks is emphasized.

In addition, we quantify some of the systematic uncertainties that affect our computations, with the intent of identifying the most correct approximations for the CUJET model.

3.1 Monte Carlo

Evaluation of the DGLV integral, Eq. (2.14), at arbitrary order in opacity is a arduous task. The analytically tractable $n = 1$ form requires numerical techniques already at second order, and without sophisticated optimization the computation of higher orders becomes prohibitive. The dimensions of the integral, in fact, grow as $3n$, and if we assume that the probability of jet scattering in the medium is approximately given by the Poisson distribution in opacity, we should, ideally, compute the induced gluon number distribution roughly up to order $n \approx 2\bar{n}$, with $\bar{n} \sim L/\lambda$.

For a typical plasma size of $L = 5$ fm and mean free path $\lambda = 1$ fm, this means $n \approx 10$, or a thirty-dimensional integral. We will see that in most cases, fortunately, the opacity series converges well before that, and an expansion up to third order is generally sufficient.

3.1.1 Importance sampling

When considering the possible algorithms to perform the integration, we need to take into account three requirements: (1) the algorithm must be able to deal with a variable number of dimensions; (2) it must be sufficiently precise, given the highly oscillatory behavior of the integrand; (3) it must be fast and suitable for further implementation into a more complex code. We opted for a Monte Carlo algorithm, refined by importance sampling techniques.

In general, importance sampling is one of the best variance-reduction techniques for estimation of integrals using Monte Carlo integration methods, useful for reducing the number of numerical iterations without affecting the precision of the result. The idea is to sample points according to some probability distribution function $p(x)$, so that the points are concentrated in the regions that make the largest contribution to the integral. In general, we are interested in computing

$$I = \int_D f(x)dx = \int_D \frac{f(x)}{p(x)} p(x)dx \ . \tag{3.1}$$

Here the importance function $p(x)$, or sampling function, is a well behaved function on the domain D. Then, for a sample of size N, the estimator of the integral is given by [209]:

$$\langle I \rangle = \frac{1}{N} \sum_{i=1}^{N} \frac{f(x_i)}{p(x_i)} \ , \tag{3.2}$$

where the $\{x_i\}$ are sampled according to the importance function $p(x)$. The variance of this estimator is given by

$$V[\langle I \rangle] = \frac{1}{N} V_p \left[\frac{f}{p} \right] \quad , \tag{3.3}$$

with V_p taken according to the distribution $p(x)$. By carefully choosing a sampling function such that $V_p[f/p] < V[f]$, we can improve the accuracy of the result or, if we reduce the sample size N, increase the speed of the algorithm. To summarize, we approximate the integral (3.1) by:

$$\int_D f(x)dx \approx \langle f/p \rangle_p \pm \sqrt{\frac{\langle (f/p)^2 \rangle_p - \langle f/p \rangle_p^2}{N}} \quad , \tag{3.4}$$

where, we remind, all the averages are taken over a set of points distributed according to $p(x)$.

The natural choice of the importance function in the DGLV integral is the distribution of transverse momentum transfers $\mathbf{q}_i$,

$$p_i(q_i) = 2 \frac{q_{\perp,i} \mu^2}{(q_{\perp,i}^2 + \mu^2)^2} \quad , \tag{3.5}$$

here normalized to 1. However, as we will see later in Chapter 4, we need a code able to work with a slightly different form of potential interaction, in order to account for dynamical effects. The normalized importance function is then chosen to be:

$$p_i(q_i) = \frac{2}{\pi} \frac{\mu}{(q_{\perp,i}^2 + \mu^2)} \quad . \tag{3.6}$$

We need to compute the cumulative distribution function,

$$CDF_{p_i}(q_i) = \int_0^{q_i} p_i(x)dx = \frac{2}{\pi}\arctan\left(\frac{q_i}{\mu}\right) \quad , \tag{3.7}$$

and then its inverse:

$$CDF_{p_i}^{-1}(y_i) = \mu\tan\left(\frac{\pi y_i}{2}\right) \quad . \tag{3.8}$$

The domain of this function is $y_i \in [0, 1)$, and using a random number generator we obtain the desired distribution of $\{q_i\}$, according to (3.6). These steps are represented in Fig. 3.1.

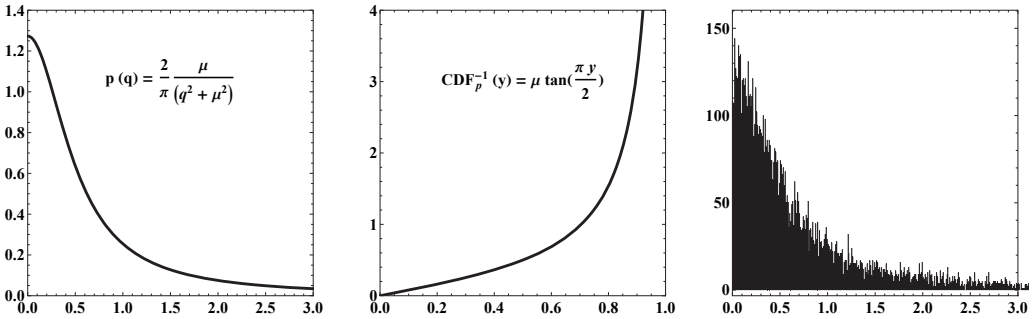

Figure 3.1: *left* Sampling function; *center* Inverse cumulative distribution function; *right* Distribution of q. We used $\mu = 0.5$ and sampled 10000 points.

One important observation to make is that, by sampling the $\{q_i\}$ according to Eq. (3.6), we are neglecting the kinematic limits in the $d\mathbf{q}_i$ integration, i.e. we are integrating the $q_{\perp,i}$'s from 0 to infinity. With the interaction potential peaked around $q \approx \mu$, the sensitivity to this limit is small and the error introduced negligible: an example is shown in Fig. 3.2.

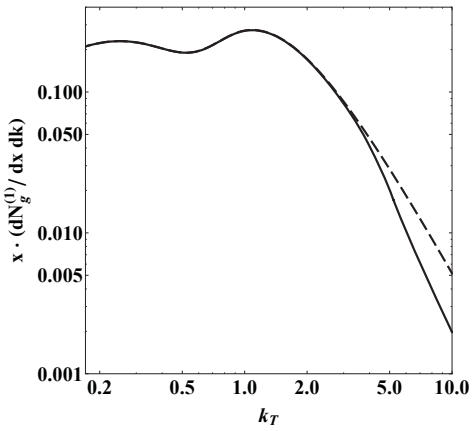

Figure 3.2: Gluon transverse momentum distribution, for a gluon of energy $\omega = 2$ GeV. The two curves represent different choices of the exchanged momentum upper integration limit: $q_{MAX} = 4.5$ GeV (solid line) and $q_{MAX} = \infty$ (dashed line). The difference, although negligible, is appreciable only in the high k_T region, often excluded by kinematic constraints.

3.1.2 Uncorrelated geometry

The DGLV integral is a function, among other variables, of the distance between scattering centers Δz_i. Their distribution is connected to the mean free path λ, which, in case of non uniform plasmas, is itself a function of z, $\lambda(z)$.

In an uncorrelated geometry, however, we do not take into account the connection between the location of the scattering centers and the mean free path, making the choice of geometry an arbitrary and crucial step toward the correct modeling of the plasma.

We start our computations with the simplest model imaginable, a brick

of uniform density, constant temperature and limited length L. For multiple scatterings identified by the set of coordinates $\{z_i\}$, we average the DGLV integral by integrating over the normalized distribution

$$\rho(z_1, \ldots, z_n) = \frac{n!}{L^n}\theta(L - z_n)\theta(z_n - z_{n-1}) \ldots \theta(z_2 - z_1) \ . \tag{3.9}$$

A more realistic model assumes an exponential distribution of scattering centers,

$$\rho(\Delta z) = \prod_{j=1}^{n} \frac{e^{-\Delta z_j/(L/(n+1))}}{(L/(n+1))} \ , \tag{3.10}$$

which has the additional advantage of being more tractable analytically. In fact, the exponential factors converts the LPM oscillating terms in Eq. 2.14 into Lorentzian factors

$$\int d\rho \cos\left(\sum_{k=j}^{m} \omega_{(k,\ldots,n)}\Delta z_k\right) = \mathrm{Re}\prod_{k=j}^{m} \frac{1}{1 + i\omega_{l,\ldots,n}L/(n+1)} \ . \tag{3.11}$$

Reducing the integrated variables by a third from $3n$ to $2n$ (the transverse exchanged momenta $\{\mathbf{q}_i\}$) and eliminating the rapidly oscillating terms, the exponential geometry configuration increases remarkably the speed and precision of our algorithm. Given the performance advantages, we will consistently choose this configuration over the uniform geometry. A comparison between the two is shown in Fig. 3.3.

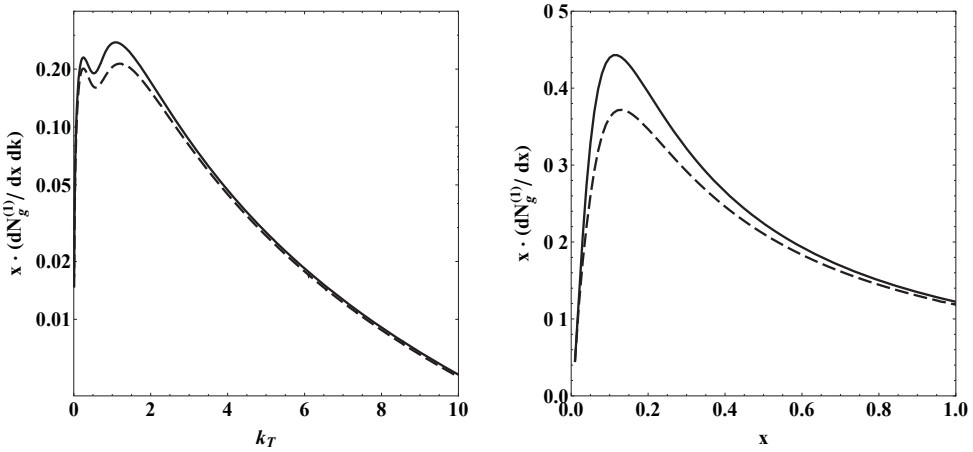

Figure 3.3: Comparison between uniform (solid) and exponential (dashed) brick geometries. *left* The gluon transverse momentum distribution shows a suppression of approximately $15 \sim 20\%$ for the exponential setup. *right* The effect on the integrated spectrum is shown: low x gluons seem more affected by the choice of geometry.

3.1.3 Code implementation

The integration of the DGLV integral, as seen in the previous Sections, is performed using an importance sampling Monte Carlo algorithm, which allows the computation of the gluon number distribution at arbitrary order in opacity. Arbitrary configurations of the plasma geometry can be used, however, to increase the speed and accuracy of the result, an analytic integration in the $\{z_i\}$ variables is often carried out according to (3.11). At the core of the Monte Carlo algorithm lies the ZIGGURAT uniform random number generator [210], here optimized for parallel processing [211].

The physical input parameters of our code are: the energy of the incoming

jet (E), the gluon fractional energy (x) and transverse momentum ($k_\perp$), the mass of the jet (M), the thermal mass of the gluons (m_g), the size of the plasma (L), the gluon mean free path (λ), the Debye screening mass (μ). The numerical parameters are simply the desired order in opacity n and the number of Monte Carlo sampling points N, typically equal to $10^5 \sim 10^6$. The output is the inclusive radiated gluon distribution ($x\frac{dN^{1+\cdots+n}}{dxd\mathbf{k}}$), evaluated for a given $k_\perp$ and x, together with the statistical error computed according to (3.4).

With the described integration method, and the clever exploitation of some of the recurrences in the DGLV series, we constructed a relatively fast algorithm: with $N = 10^6$, the evaluation at each $k_\perp$ and x for a given order n takes roughly $\sim\ 2.5^n$ seconds. It takes slightly longer when also the $\{z_i\}$ integration is performed numerically.

3.2 Convergence of the opacity series

The opacity series approach builds upon the Bertch-Gunion incoherent limit and includes multiple coherent scatterings, interference with the production vertex radiation and gluon cascading. The LPM effect and the interplay between the cosine factors in the DGLV integral determine how fast the series converges to its asymptotic limit.

To recapitulate, the induced radiation spectrum at first order in opacity

takes the form

$$\frac{dN_g^{n=1}}{dxd^2\mathbf{k}} = \frac{C_R\alpha_s}{\pi^2}\frac{1}{x}\frac{L}{\lambda}\int dz\ \bar{\rho}(z)\int d^2\mathbf{q}\frac{\mu^2}{\pi(\mathbf{q}^2+\mu^2)^2} \times \frac{2(\mathbf{k}-\mathbf{q})}{(\mathbf{k}-\mathbf{q})^2+\chi^2}\left(\frac{(\mathbf{k}-\mathbf{q})}{(\mathbf{k}-\mathbf{q})^2+\chi^2}-\frac{\mathbf{k}}{\mathbf{k}^2+\chi^2}\right) \times \left(1-\cos\left(\frac{(\mathbf{k}-\mathbf{q})^2+\chi^2}{2xE}\Delta z\right)\right)\ . \tag{3.12}$$

$\Delta z = z - z_0$ represents the distance from the formation vertex to the first scattering point, and the result is averaged over the normalized distribution $\bar{\rho}(z)$. The relevant terms in (3.12) are: (1) the opacity $\left(\frac{L}{\lambda}\right)$; (2) the effective interaction potential $\left(\frac{\mu^2}{\pi(\mathbf{q}^2+\mu^2)^2}\right)$; (3) the radiation antenna $\left(\frac{\mathbf{k}-\mathbf{q}}{(\mathbf{k}-\mathbf{q})^2+\chi^2}\cdot(...)\right)$; (4) the LPM phases $\left(1-\cos\left(\frac{(\mathbf{k}-\mathbf{q})^2+\chi^2}{2Ex}\Delta z\right)\right)$.

We can study in more details the LPM phases and the interplay between formation time and mean free path: the time it takes for the gluon to become on-shell, τ_f, is approximately equal to

$$\tau_f \approx \frac{\omega}{(\mathbf{k}-\mathbf{q})^2+\chi^2}\ , \tag{3.13}$$

with $\omega = xE$ the energy of the radiated gluon. If there are many momentum kicks from the medium within a coherence length, then $\mathbf{q} \to \sum_i \mathbf{q}_i$; however, for a qualitative estimate, we can assume $\mathbf{k} \gg \mathbf{q}$ and $\tau_f \approx \omega/\mathbf{k}^2$. In reality, the interplay between $\mathbf{k}$ and $\mathbf{q}$ makes the estimation of the real formation time difficult, and once the mass of a heavy quark is taken into account, the $\chi^2 = M^2x^2 + m_g^2(1-x)$ factor starts playing a relevant role by reducing the

formation time and by pushing the radiation back into the incoherent regime.

The other scale to take into consideration while determining the effects of coherence physics is λ. The assumption of uncorrelated geometry, however, makes the relation between the mean free path and the distribution of scattering centers loose, while in reality Δz and λ are strictly connected. We will see in the next Chapter how to set the z distribution proportional to the temperature profile of the plasma and therefore provide a more natural connection between the two.

Coherence effects are dominant when $\lambda \gg \tau_f$, and are analytically determined by the magnitude of the LPM phases: larger phases are responsible for the oscillatory behavior characteristic of the incoherent limit, while smaller phases cause an approximate cancellation among the cosine terms, typical result of coherence physics. For $n = 1$ and large formation times, for instance, the LPM term $\cos(\Delta z/\tau_f)$ approaches unity, giving rise to a neat cancellation.

In order to understand how the convergence of the opacity series is related to the regime – coherent or incoherent – of the radiation mechanism, we first compare the DGLV $n = 1$ result with the Gunion-Bertsch limit (Eq. (2.3)): at first order, the opacity series only includes interference effects between the creation and the induced radiation vertex. By plotting the gluon transverse momentum distribution for different plasma sizes L, we can represent in Fig. 3.4 the suppression of the induced radiation due to such interference

effects.

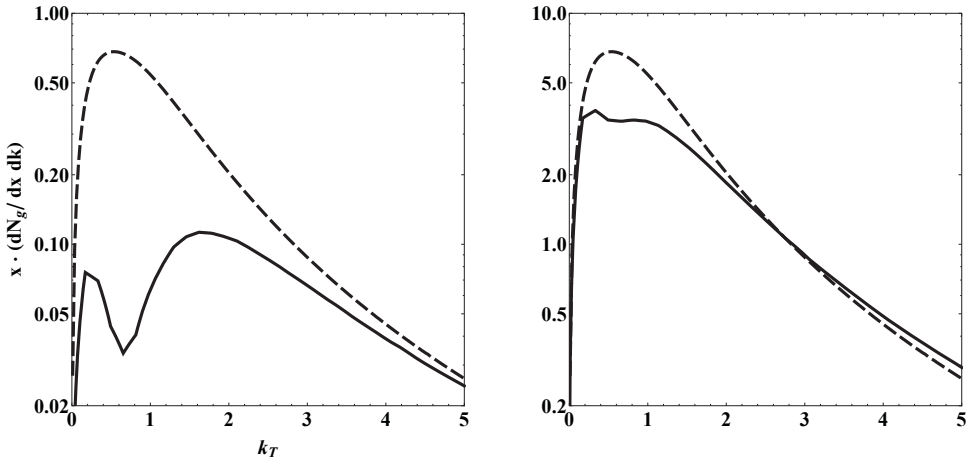

Figure 3.4: Comparison between the DGLV $n = 1$ gluon transverse momentum distribution (solid) and the Gunion-Bertsch incoherent limit (dashed), for different plasma sizes. On the left, we use a brick of size $L = 5$ fm; on the right, the length L is increased to 50 fm. The energy of the incoming light jet is 50 GeV, and the radiated gluon energy ω is equal to 5 GeV. Notice the suppression of the induced radiation due to interference with the creation radiation for short path lengths. Such effect vanishes in the $L \to \infty$ limit, as expected, where the average distance between the creation vertex and the scattering center becomes larger ($\overline{\Delta z} = L/2$).

The next step is to add higher order corrections to the results. This is shown in Fig. 3.5. The dominant contribution to the suppression of the induced radiation still comes from the the $n = 1$ term: assuming that the probability of hitting a given number of scattering centers follows a Poisson distribution whose average equals the opacity, we would expect the GLV series to peak around $n = L/\lambda$. Instead, we observe that at $n = L/\lambda \approx 5$ the opacity series already converges to its asymptotic value, making further cor-

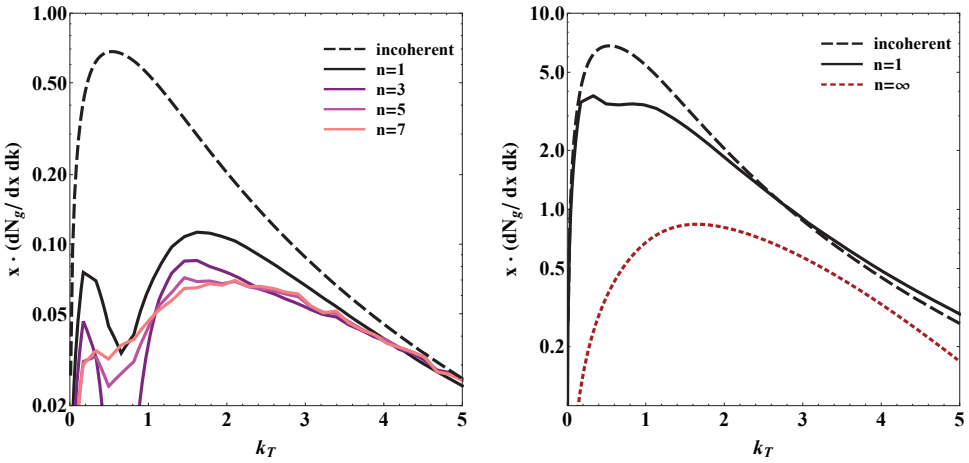

Figure 3.5: Higher order DGLV corrections are added to the $n = 1$ results previously shown in Fig. 3.4. The series is shown to converge already at $n = 5$, with the first order result still giving the biggest contribution to the suppression. The opacity expansion, valid at the intermediate opacities characteristic of nuclear collisions ($L = 5$ fm, *left*), breaks down for plasmas of the size of tens of fermi ($L = 50$ fm, *right*): in this case the radiation spectrum is replaced by the multiple soft scattering approximation (cf. Section 2.3.4).

rections negligible. Why? The reason is the following: for short path lengths, the interference with formation radiation is the dominant effect, on top of which the corrections due to multiple scatterings in the medium are small. As L increases, this is no longer true and the resummed result is expected to asymptotically converge to the multiple soft scattering limit.

We perform a systematic study of the properties of the series by analyzing its convergence for several coherent and incoherent regimes. Our goal is to understand if there is an optimal order at which the series can be truncated

for most of the practical needs, and quantify the error one is eventually making. For different sets of parameters (E, ω and L), we compute in Fig. 3.6 and Fig. 3.7 the radiation spectrum up to ninth order in opacity.

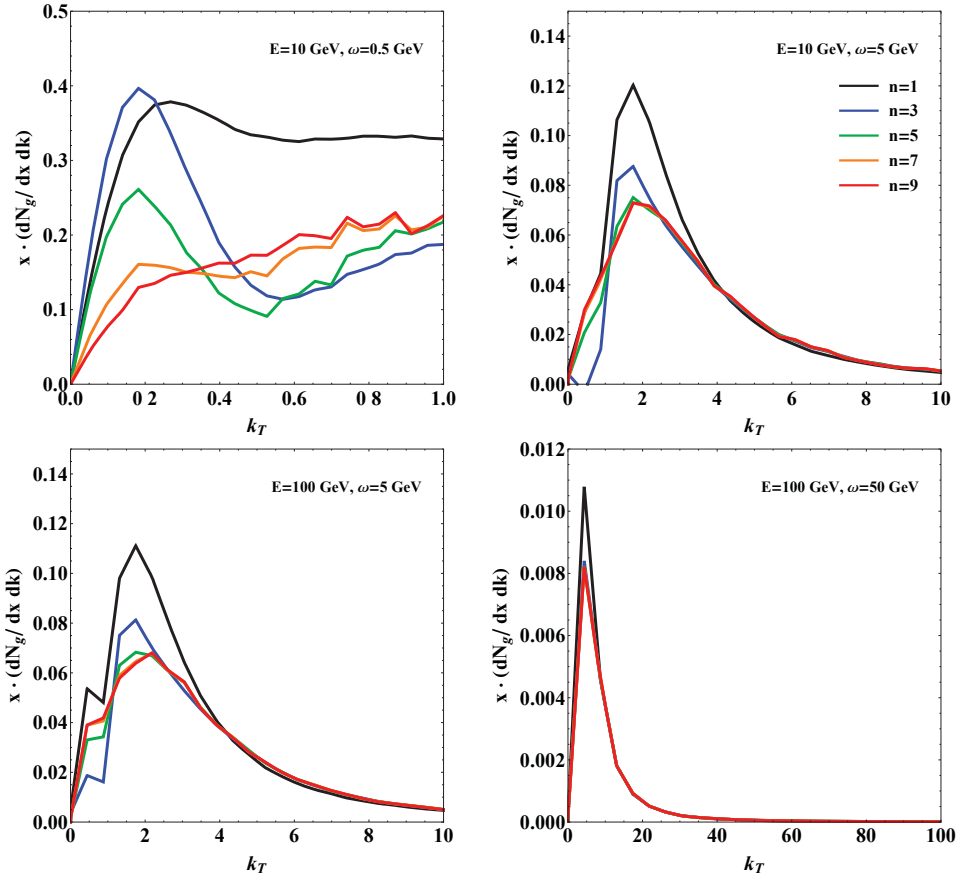

Figure 3.6: Gluon transverse momentum distribution generated by a light quark jet traversing a plasma of thickness $L = 5$ fm. Several orders in opacity up to $n = 9$ are shown in all figures. The incoherent or coherent regime of the radiation is determined by the value of ω: incoherent (top-left), intermediate (top-right and bottom-left), coherent (bottom-right). Note the faster convergence of the series for higher values of the gluon energy, i.e. longer formation times, determined by the reciprocal cancellation of the oscillating LPM factors. Also, the transverse momentum distribution seems to depend mostly on the value of the gluon energy ω, rather than the original energy of the jet E (top-right and bottom-left figures). Other parameters used in the simulation are: $\lambda = 1.16$ fm, $\mu = 0.5$ GeV, $M = 0.2$ GeV, $m_g = 0.356$ GeV, $\alpha_s = 0.3$.

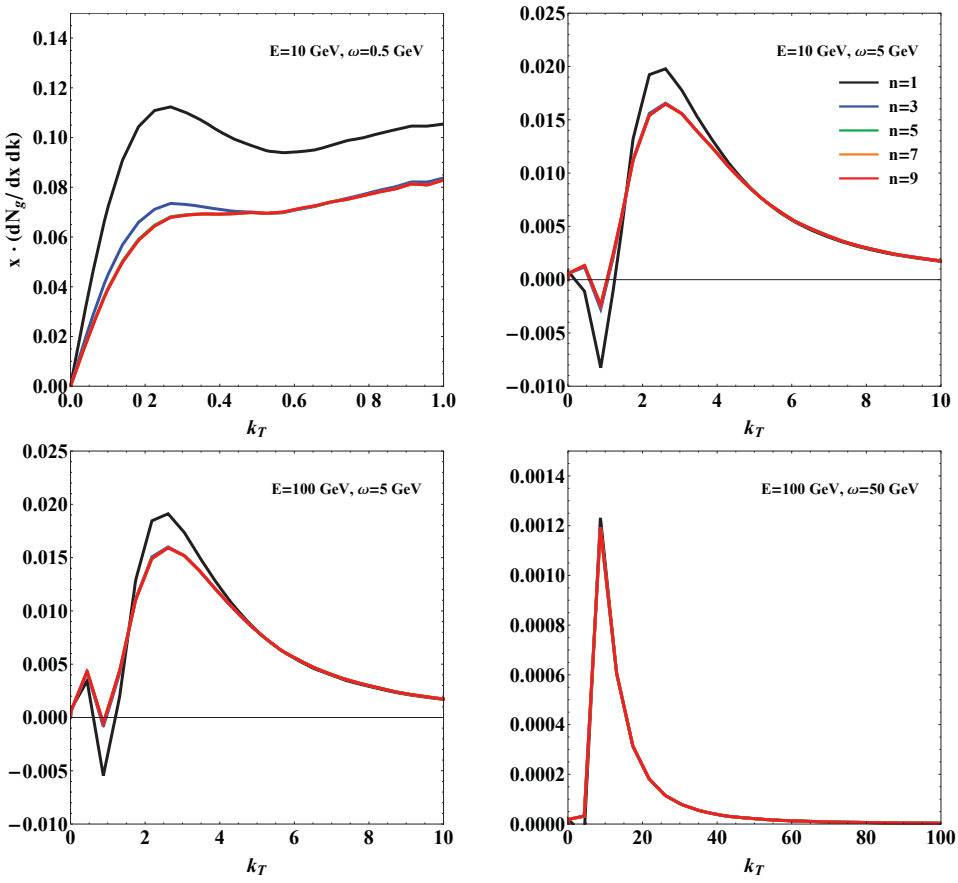

Figure 3.7: Gluon transverse momentum distribution generated by a light quark jet traversing a plasma of thickness $L = 2$ fm. As in Fig. 3.6, several orders in opacity up to $n = 9$ are shown in all figures. Here, as intuitively expected, the convergence is improved by the reduced size of the medium.

We conclude that coherent radiation is associated with faster convergence: the large formation time suppresses the magnitude of the LPM phases, leading to an approximate cancellation of the cosine terms in (2.14). On the other hand, the oscillatory behavior typical of incoherent emission results into a slower convergence of the opacity series.

In Fig. 3.8, we show the same simulation for a heavy quark jet in a plasma of thickness 5 fm: the convergence rate is almost unchanged despite the dependence of the gluon formation time on the mass of the incoming quark, manifested in the term $\chi^2 = M^2x^2 + m_g^2(1-x)$. The increase of M is in fact compensated by the small value of x for $\omega \ll 1$. Notice however the suppression of the radiated gluon multiplicity with respect to the light jet results of Fig. 3.6.

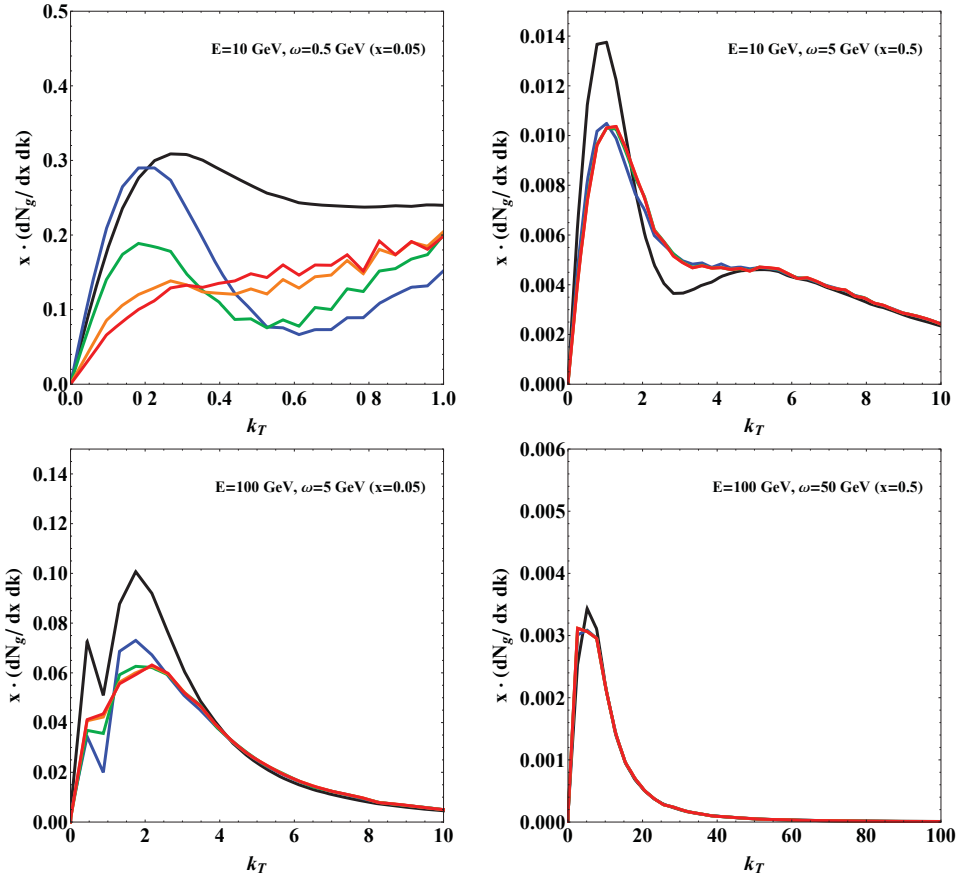

Figure 3.8: Gluon transverse momentum distribution generated by a heavy quark jet traversing a plasma of thickness $L = 5$ fm. The mass of the quark is assumed $M = 4.75$ GeV. All other parameters are the same as in Fig. 3.6. The effect of the quark mass in the expression for the formation time, which intuitively would slow the convergence of the series, is balanced by the x dependence of $\chi^2 = M^2x^2 + m_g^2(1-x)$: for small x, the results do not differ much from their light quark jet counterpart. However, we observe a remarkable splitting between radiation distributions with same gluon energy ω but different heavy jet energy E (top-right and bottom-left figures), due to the presence of the same x dependent χ^2 in the denominator of the antenna term in (3.12), which further suppresses radiation at large x.

Overall, we can conclude that except for a limited region of phase-space, when the emission mechanism is clearly incoherent, a satisfactory result can already be obtained by truncating the expansion at third order. Furthermore, when averaging over all possible path lengths in a realistic nuclear collision, $2 \lesssim L \lesssim 5$ fm, even the first order in opacity might be regarded as a good approximation to the series (Fig. 3.7).

3.3 Transverse momentum distribution

We now shift the attention from the convergence of the opacity expansion to the dependence of the gluon spectrum on the transverse momentum $k_\perp$.

In the previous Section we observed that ω determines how fast the series converges to its asymptotic limit. We didn't take into account the fact that the convergence appears to be faster for larger values of the transverse momentum $k_\perp$, despite the shorter formation time proportional to $1/k^2$. For instance, in Fig. 3.6, with $E = 100$ GeV, $\omega = 5$ GeV and $L = 5$ fm, the first order is already a good approximation for $k \geq 4$ GeV, whereas between $2 \geq k \geq 4$ GeV the fifth order is needed; below $k = 2$ GeV, only $n = 7$ is a good approximation to the series.

The reason can be found in the radiation antenna term of Eq. (3.12), which determines the shape of the momentum distribution: its $1/k^3 \sim 1/k^4$ asymptotic behavior suppresses high momentum corrections and dwarfs the contribution of higher orders in opacity. The effect is very similar to what

we observed for heavy quarks jets in Fig. 3.7, where the large contribution of χ^2 in the denominator of the antenna term offsets the increased oscillatory behavior of the integral due to shorter gluon formation times.

We noted in Chapter 2 the ability of the DGLV expansion to interpolate between the single hard scattering and multiple soft scattering approximations. The latter is derived assuming the radiated gluon experiences Gaussian diffusion in the transverse momentum space (cf. Section 2.3.4): for small gluon emission angles, i.e. $k_\perp \lesssim \hat{q}L$, the momentum distribution derived from the DGLV series approaches this limit. This effect is shown in Fig. 3.9 for a heavy quark jet.

Larger angle radiation, however, is poorly treated in the multiple soft scattering approximation, and the opacity expansion which includes the hard power-law Landau tails of the radiation reproduces the gluon multiplicity more accurately.

3.3.1 Integration and kinematic limits

The hard $1/k^3 \sim 1/k^4$ tails of the DGLV distribution offer a relevant contribution to the total emitted radiation and become a source of concern once finite kinematic limits are taken into account. If the integrand in (3.12) were exact, the result would vanish for unphysical values of $k_\perp$, and there wouldn't be the need of worrying about integration limits. In reality, however, the model is derived assuming collinear approximation ($k_\perp \ll \omega$), therefore

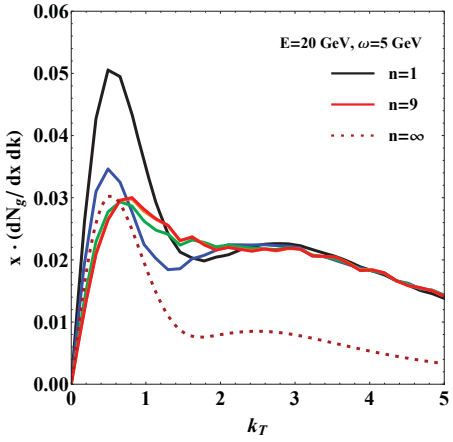

Figure 3.9: Gluon transverse momentum distribution for a heavy quark jet traversing a plasma of size $L = 5$ fm. The DGLV opacity expansion is computed up to ninth order and is shown to converge to the multiple soft scattering limit for small $k_\perp \lesssim \hat{q}L \approx 1$ GeV.

kinematic limits need to be imposed to enforce physicality. The integral, for consistency, should not be sensitive to the particular choice of UV $k_\perp$ cutoffs, but given the hard tails of the distribution, we will see that this is not always going to be the case.

The choice of upper bounds in the $k_\perp$ integration depends on the particular interpretation of x in the expression for the gluon energy $\omega = xE$: x as the fractional energy carried away by the radiated gluon ($x \equiv x_E$, $\omega = x_E E$), or x as the fraction of plus-momentum in light-cone coordinates, in which case $x \equiv x_+$ and $\omega \approx x_+ E^+/2$[1]. In the strictly collinear limit in which the

[1]Assuming the incoming parton four-momentum is $(E, E, \mathbf{0})$, then $E_+ = 2E$

DGLV integral is derived, the two definitions coincide:

$$x_+ = \frac{1}{2} x_E \left(1 + \sqrt{1 - \left(\frac{k_\perp}{x_E E} \right)^2} \right) \quad . \tag{3.14}$$

Equation (3.14) can be easily derived by writing explicitly the gluon four-momentum in Minkowski and light-cone coordinates, denoted respectively by parenthesis and square brackets:

$$k = (x_E E, \sqrt{(x_E E)^2 - \mathbf{k}}, \mathbf{k}) = [x_+ E^+, \frac{\mathbf{k}^2}{x_+ E^+}, \mathbf{k}] \quad . \tag{3.15}$$

Depending on the interpretation of x, the upper kinematic limit on $k_\perp$ will vary: in the case of x_+, in order to ensure forward gluon emission we need to set $k_\perp^{MAX} = x_+ E^+$, whereas in the case of x_E, to keep $k_\perp$ real we must set $k_\perp^{MAX} \approx xE \sin\theta$, where θ is the angle between the radiated gluon and the propagating parton ($\pi/2$ for forward emission)[2]. In Fig. 3.10, we plot the $k_\perp$ integrated gluon number distribution $x\frac{dN_g}{dx}$, for both interpretations of x and two different cutoff angles θ; to compare apples to apples, we add the Jacobian of the transformation $x_+ \to x_E$ to the x_+ curve and integrate up to $k_\perp^{MAX} = xE \sin\theta$:

$$\frac{dN_g}{dx_E} = \int_0^{x_E E \sin(\theta)} d\mathbf{k} \frac{dN_g}{dx_+ d\mathbf{k}}(\mathbf{k}, x_+(x_E)) J(x_E) \quad , \tag{3.16}$$

[2]In both cases, we neglect corrections due to the recoil of the scattering centers in the medium.

$$J(x_E) \equiv \frac{dx_+}{dx_E} = \frac{1}{2}\left(1 + \left(1 - \left(\frac{k_\perp}{x_E E}\right)^2\right)^{-1}\right) \quad . \tag{3.17}$$

The differences are notable, and even more prominent in the small x region, which dominates the gluon spectrum. The question of how we are going to quantify the error introduced by this systematic source of theoretical uncertainty arises immediately, and an answer will be given in the next Paragraph. In the discussion above, we followed closely an in-depth analysis performed by Horowitz and Cole [204].

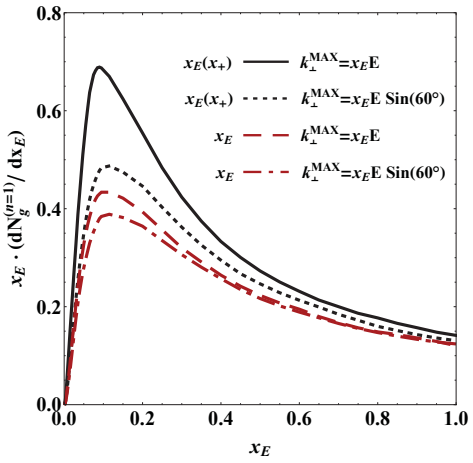

Figure 3.10: $k_\perp$ integrated, $n = 1$ gluon number distribution generated by a 20 GeV light quark jet traversing a plasma of thickness $L = 5$ fm. The two interpretations of x as gluon fractional energy (x_E) or gluon fractional plus-momentum (x_+) lead to remarkably different results, especially in the soft $x \ll 1$ region. The uncertainty due to the choice of θ^{MAX} is noticeable but less prominent.

Systematic uncertainties

We approach the problem of quantifying the systematic uncertainties caused by the choice of the $k_\perp$ integration limits in a way which will be iterated several times throughout the construction of the CUJET model. The idea is to isolate those sources of uncertainty that have a clear impact on the observables we are going to compute from other sources whose effect is hindered by the simple rescaling of a free parameter.

In the context of the $k_\perp$ integration, we ask in Table 3.1 what is the sensitivity of the energy loss $\Delta E/E$ to the particular choice of integration limits, provided the freedom to adjust a free parameter identified as the coupling constant α_s.

Curve	$\epsilon \equiv \frac{\Delta E}{E}$	$\alpha_s^{\epsilon=\mathbf{0.32}}$	$\alpha_s^{\epsilon=\mathbf{0.24}}$
$x_E(x_+)$	**0.32**	0.3	0.27
$x_E(x_+)^{\theta=60^\circ}$	**0.27**	0.32	0.29
x_E	**0.24**	0.33	0.3
$x_E^{\theta=60^\circ}$	**0.23**	0.33	0.30

Table 3.1: Fractional energy loss $\Delta E/E$ for the curves shown in Fig. 3.10, with $\alpha_s = 0.3$. The results are indicated in the second column and range from 0.23 to 0.32. In the two rightmost columns are listed the values of the effective parameter α_s^ϵ needed to obtain the energy loss specified in ϵ. The free parameter α_s needs to be tuned at most $\pm 10\%$.

Given the interest in the ratio of light to heavy quark energy loss, we can immediately construct an error band which offers a quantitative measurement of the uncertainty generated by the choice of $k_\perp$ limits. In this way, α_s is factored out and the results are independent of the rescaling of the

free parameter. Fig. 3.11 shows the scaling of $\Delta E_{light}/\Delta E_{heavy}$ with the jet energy E and the plasma size L, for two distinct assumptions $x \equiv x_E$ and $x \equiv x_+$.

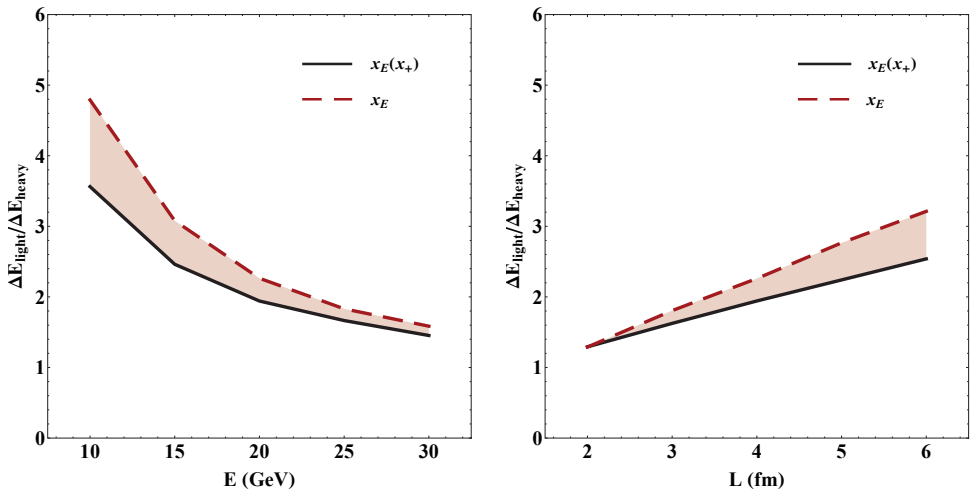

Figure 3.11: Energy loss ratio between light and heavy quark jets, for different interpretations of x as in Fig. 3.10. Here $\alpha_s = 0.3$, $L = 5$ fm (*left*), $E = 20$ GeV (*right*) and the energy loss has been computed at first order in opacity. An error of approximately $\sim 25\%$ is introduced for sufficiently small energies and large plasma sizes.

The conclusion is evident: the choice of $k_\perp$ limits has a relevant impact at small energies $E \leq 15$ GeV and long path lengths $L \geq 5$ fm. Further theoretical steps to address large angle radiation need to be taken, and the collinear approximation relaxed. Until then, in the development of the CUJET model we adhere to the collinear derivation of GLV and interpret $x \equiv x_+$.

3.3.2 Dead cone

In this paragraph we want to check the effects that the parton mass has on the transverse radiation distribution.

To summarize what we have seen so far, the mass term M appears to have only a minor impact on the convergence of the series, if nothing else by even improving it for certain combinations of E and ω. For very soft gluons ($x \ll 1$), the heavy quark jet radiation spectrum does not differ much from its light quark counterpart, while for large values of x the radiation seems highly suppressed. The strong x dependence of the magnitude and shape of $dN_g/dxd\mathbf{k}$, as seen in Fig. 3.8, breaks the scaling with ω typical of light quark radiation.

Another effect is the filling of the "dead cone" characteristic of the vacuum spectrum (cf. Section 2.1). In vacuum, the transverse momentum distribution takes the form

$$x\frac{dN_g^0}{dxd\mathbf{k}} \sim \frac{\mathbf{k}^2}{(\mathbf{k}^2+\chi^2)^2} \ , \tag{3.18}$$

and the depletion of radiation takes place at angles

$$\theta < \chi/\omega = \sqrt{M^2x^2 + m_g^2(1-x)}/(xE) \ . \tag{3.19}$$

If we compare in Fig. 3.12-*right* the radiation spectrum of a heavy quark at different orders in opacity with the reference vacuum spectrum radiation, we

notice immediately that the induced radiation fills in the dead cone already at first order in opacity. If the possibility for bottom quarks to radiate longitudinally enhances their rate of energy loss, on the other hand the dead cone region constitutes only a small fraction of the available phase space, and the energy loss experienced by a heavy quark remains smaller than that of a light jet.

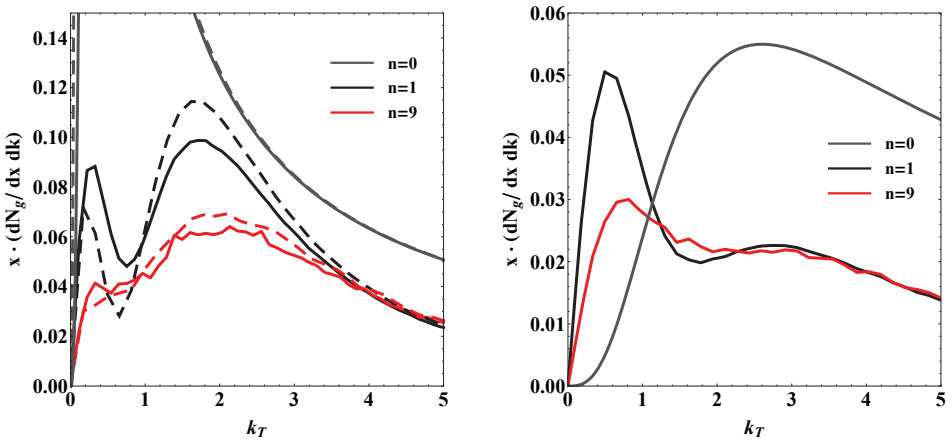

Figure 3.12: Radiation spectrum for charm (*left*) and bottom (*right*) quarks, with $E = 20$ GeV and $\omega = 5$ GeV ($x = 0.25$). The masses are assumed $M_c = 1.2$ GeV and $M_b = 4.75$ GeV. The dashed curves represent the spectrum of a light jet of mass $M_l = 0.2$ GeV. Notice the similarity between the light and charm spectra, as opposed to the bottom one. The vacuum spectrum radiation is added to the plot (gray curve), showing the radiation dead cone for bottom quark jets.

The left panel of Fig. 3.12 shows instead a striking feature: despite its non-vanishing mass equal to 1.2 GeV, the charm quark leads to a radiation spectrum very similar to the one of light quarks: not only the dead cone is absent and the vacuum spectrum almost divergent for $k_\perp \to 0$, but even

the spectra have approximately the same shape and magnitude. This critical feature will have vast phenomenological implications in the prediction of physical observables.

3.4 Energy loss

In the previous Sections we have studied in details the gluon transverse momentum distribution: we now want to shift gear and integrate over **k** to compute the radiation spectrum $x_E dN_g/dx_E$[3]. This is shown in Fig. 3.13 for a different set of initial parameters (E,L) and quark flavors.

[3]Here x_E unequivocally refers to the gluon fractional energy.

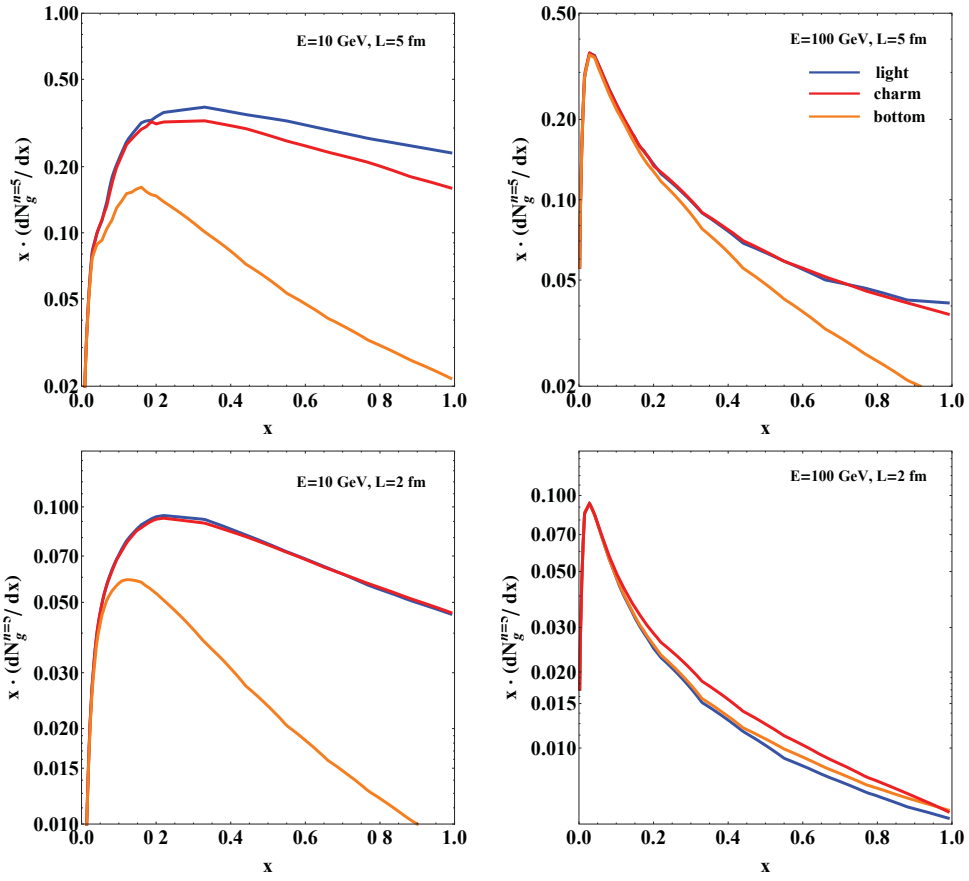

Figure 3.13: Gluon number distribution generated by a light (blue), charm (red), bottom (orange) quark jets traversing a brick-like plasma of temperature $\sim$ 250 MeV. All results are computed up to fifth order in opacity. We remind the mass values used in the computation: $M_l = 0.2$, $M_c = 1.2$, $M_b = 4.75$ GeV. The splitting between light and heavy quarks is evident at low energies ($E = 10$ GeV), but negligible at $E = 100$ GeV. Charm quarks results show a behavior almost identical to light jets.

The remarkable similarity between light and charm jets, previously observed in the transverse momentum distribution, is confirmed here. As expected, radiation from a bottom quark is instead heavily suppressed, except

for very high energies where the mass difference between the flavors becomes negligible. Finally, we notice how radiative energy is mostly carried away by low energy gluons, i.e. the distribution peaks at small values of x.

The next and last step in our analysis of the DGLV opacity expansion is to integrate over the gluon fractional energy x_E and compute the jet energy loss $\Delta E/E$. We assume that no other form of energy transfer happens between the jet and the medium, so that all the energy lost to induced radiation directly translates into quenching of the jet. The integration over x_E implies a coordinate transformation $x_+ \to x_E$, according to Eq. (3.16) and Eq. (3.17)

In Fig. 3.14 we show the energy loss of all three quark flavors assuming propagation through a brick-like plasma of temperature $\sim$ 250 MeV. We

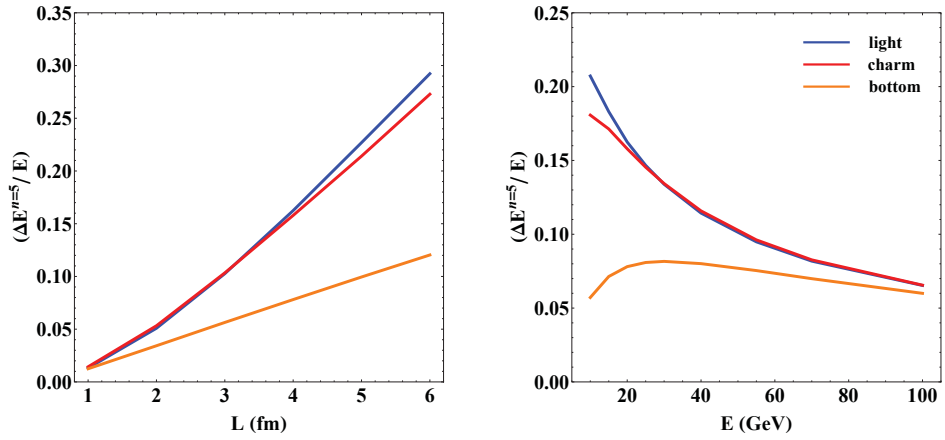

Figure 3.14: Relative energy loss $\Delta E/E$ for a light (blue), charm (red) and bottom (orange) quark jet, computed to fifth order in opacity. We show the dependence of $\Delta E/E$ on L with $E = 20$ GeV (*left*) and on E with $L = 4$ fm (*right*).

draw the following conclusions:

- Light and charm quarks experience the same amount of radiation even at relatively low energies and despite their mass difference.
- Bottom quarks are generally less quenched due to their heavier mass, however at high enough energies such difference vanishes. This confirms the expected asymptotic behavior of the theory.
- Light and charm quark jet energy loss grows quadratically with L, a distinct signature of the LPM effect. On the other hand, bottom quark jet energy loss grows linearly with L, characteristic of incoherent radiation emission.
- For sufficiently small plasmas or short path lengths ($L \lesssim 2$ fm), the energy loss experienced by all flavors is similar.

The non-trivial behavior of $\Delta E/E$ as a function of E indicates the importance of computing observables within a range of energies as broad as possible.

Systematic uncertainties

All the results we have shown so far have been computed to fifth order in the opacity series. It's time to ask the following question: was it necessary? According to what we have seen in Section 3.2, Fig. 3.6 and Fig. 3.8, it seems that higher order corrections cannot be ignored, at least if the goal is to make quantitative – and not only qualitative – predictions. Unfortunately,

the numerical power required to drive the computation at such high levels of precision might prove to be insufficient to calculate more complex observables than the simple energy loss for one specific plasma setup. A limitation of this kind would indisputably hinder the capabilities of our algorithm and limit its predictive power.

It is then our priority to quantify the error introduced by eventually limiting the computations to lower orders in opacity.We proceed in the exact same way as we did in Section 3.3.1, by looking at the energy loss ratio between a light and a bottom quark jets. The comparison between the first and fifth order in opacity $\Delta E_l/\Delta E_b(E, L)$ is a good indication on whether high order in opacity computations are needed.

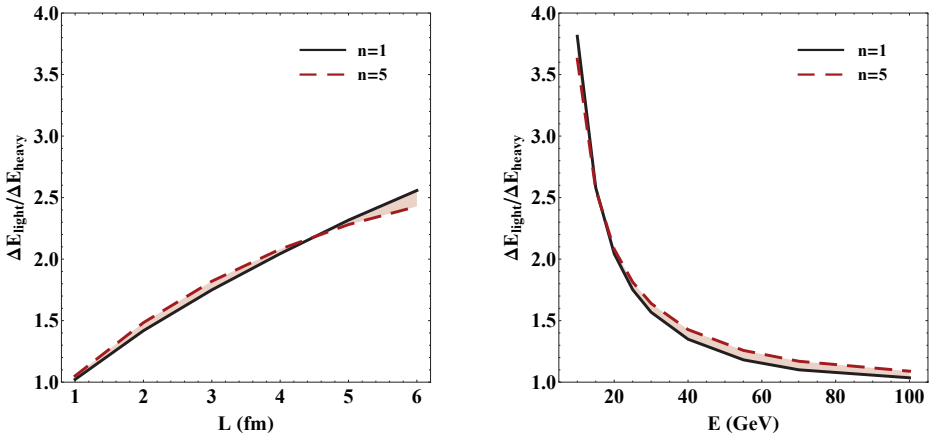

Figure 3.15: Energy loss ratio between light and heavy quark jets, as a function of E (*left*) and L (*right*). The solid black curves correspond to the $n = 1$ approximation to the opacity series and are the same as the solid black curves of Fig. 3.11. The dashed red curves are obtained by computing the energy loss up to fifth order in opacity. The difference is negligible across the whole range of jet energies and path lengths.

The results shown in Fig. 3.15 are striking: when the ratio between light and heavy quarks is taken, there is almost no difference between the first and fifth order in opacity. This implies that, granted the freedom to adjust the absolute value of the energy loss with a small ($\lesssim 10\%$) rescaling of the effective coupling constant α_s, the $n = 1$ approximation to the opacity series appears to be as good as the $n = 5$ one.

Another set of observables might of course scale differently with the opacity. However, for the purpose of computing the energy loss of different quark flavors, we have proved that truncating the series already at first order does not add a relevant source of systematic uncertainty. Unless otherwise stated, all the analysis presented in the following will be limited to $n = 1$.

3.4.1 Multiple gluon emission

Multiple gluon emission can be accounted for by performing a Poisson expansion in the number of emitted gluons, as we saw in Section 2.3.3 of the previous Chapter. Even assuming multiple incoherent radiation, statistical fluctuations in the number of emissions have an impact on the energy loss of the parent jet.

Starting from the integrated gluon spectrum dN/dx, a Poisson expansion is performed to obtain the full radiative energy probability distribution $P(\epsilon)$, with $\epsilon \equiv \Delta E/E$ (cf. Eq. (2.20)).

$$P(\epsilon) = P_0\delta(\epsilon) + \tilde{P}(\epsilon)|_0^{\epsilon_{MAX}} + P_1\delta(\epsilon_{MAX} - \epsilon) \tag{3.20}$$

Here the upper bound $\epsilon^{MAX} = 1$ is strictly valid in the massless limit: for a quark of mass M, $\epsilon^{MAX} = 1 - M/E$. Once all the terms in Eq. (3.20) are calculated, we correct the normalization of $P(\epsilon)$ in the physical range $\epsilon \in [0, \epsilon_{MAX}]$.

The energy loss is computed by integrating $\int d\epsilon\ \epsilon\ P(\epsilon)$ over the range $[0, \epsilon^{MAX}]$. In Fig. 3.16 we show the probability distribution $P(\epsilon)$ for different quark flavors that propagates into a plasma of size L. The integrated energy loss $\Delta E/E$ is shown in Fig. 3.17.

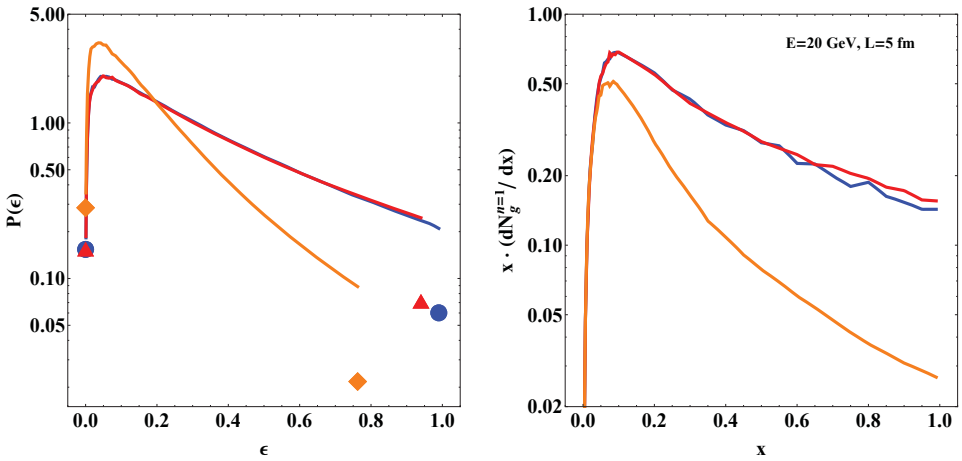

Figure 3.16: *left* Normalized radiative energy probability distribution $P(\epsilon)$ for light (blue), charm (red) and bottom (orange) jet quarks. The initial energy of the jet is 20 GeV and the size of the plasma 5 fm. All results are computed at first order in the opacity series. The markers on the left side represent the probability of zero gluon emission ($\epsilon = 0$, no energy loss), whereas the markers on the right side represent the probability of complete quenching ($\epsilon = 1 - M/E$). Notice again how bottom quarks consistently lose less energy than light ones. *right* The gluon spectrum $x\ dN^{n=1}/dx$ used to compute the distribution on the left via Eq. (2.21) is shown for reference.

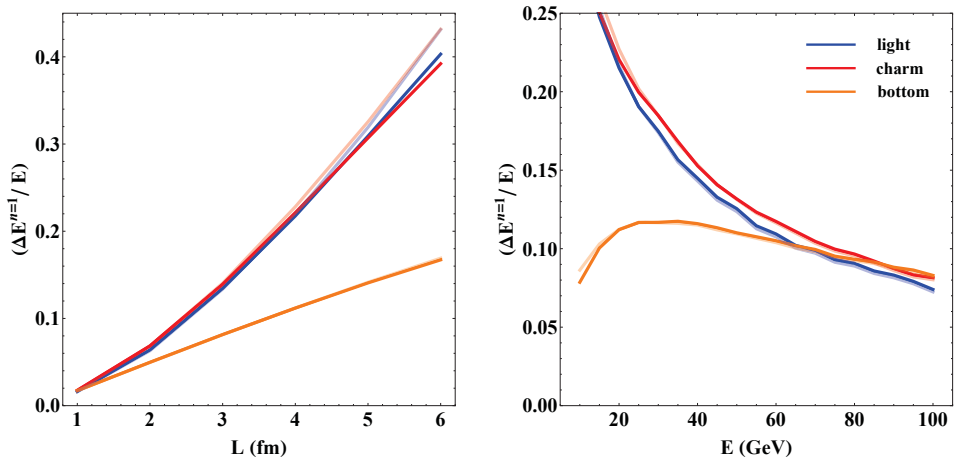

Figure 3.17: Energy loss $\Delta E/E$ for different quark jet flavors, with (solid lines) or without (opaque lines) the inclusion of fluctuation effects. The former are obtained by integrating $\epsilon\ P(\epsilon)$, the latter by integrating $x\ dN/dx$. As in Fig. 3.14 (where results are computed to fifth order in opacity), we show the dependence of $\Delta E/E$ on L fixing $E = 20$ GeV (*left*), and on E fixing $L = 4$ fm (*right*).

The inclusion of fluctuation effects appears to alter only minimally the result.

3.5 Conclusions

In this Chapter we presented the numerical algorithm at the core of the CUJET model. The clever application of Monte Carlo techniques allows for an extensive analysis of the DGLV energy loss expansion at arbitrary orders in opacity and poses the basis for the computation of more complex observables which can be directly compared to experimental data.

We performed an extensive analysis of the induced transverse radiation spectrum, with particular attention to the convergence of the opacity series. We then integrated over the transverse momentum $k_\perp$ and fractional energy loss x to obtain the energy loss of the jet.

This is a brief, non-exhaustive list of what we learned:

- The computation of the opacity series at intermediate opacities is essential to interpolate between the 'thin' and 'thick' plasma approximations. For the only purpose of computing inclusive variables such as the energy loss, the approximation to the first order is sufficient. However, future measurements such as jet broadening will require the computation of the full transverse radiation spectrum at higher order in opacity.

- Large angle radiation is relevant and the DGLV formalism is sensitive to the kinematic cutoff on $k_\perp$. We address this issue by carefully performing a coordinate transformation as suggested in [204].

- The energy loss does not distinguish between light and charm quark jets. Bottom quarks are suppressed, and the energy loss dependence on the size of the plasma L is linear rather than quadratic (incoherent versus LPM). For short path lengths ($L \lesssim 2$ fm) light and heavy quarks experience the same amount of quenching.

Chapter 4

Beyond GLV

This Chapter is devoted to the description of several improvements that are added on top of the GLV radiation kernel presented in Chapter 2 and 3.

In Section One, the static effective GLV potential is replaced with a dynamically screened potential developed by Djordjevic at first order in opacity. The effects of multiple coherent scatterings in a dynamical plasma are studied by developing a new effective potential which interpolates between the static and purely dynamical limits.

In Section Two, we add elastic energy losses to the radiative component. A brief theoretical introduction is presented before studying the effects of elastic collisions on jet quenching.

In Section Three, the average of the radiation kernel over an uncorrelated geometry is replaced by the jet path integration over a space-time dependent plasma density. The brick setup approximation is dropped and computations

are performed in a more realistic plasma scenario.

This allows the study of several dynamical effects, such as the running of the strong coupling constant $\alpha_s(Q^2)$ presented in Section Four.

4.1 Dynamical potential

"The computation of radiative energy loss in a dynamically screened QCD medium is a key ingredient for obtaining reliable predictions for jet quenching in ultra-relativistic heavy ion collisions. [...] The currently available studies suffer from one crucial drawback: the medium induced radiative energy loss is computed in a QCD medium consisting of randomly distributed but static scattering centers (static QCD medium). In such a medium the collisional energy loss is exactly zero. [...] Recent calculations showed that the collisional contribution is important and comparable to the radiative energy loss. The static approximation is thus qualitatively wrong as far as the computation of collisional energy loss is concerned and should therefore also be revisited in the context of radiative energy loss." (Djordjevic, [212])

The inclusion of dynamical effects is achieved by computing the scattering QCD diagrams in a finite temperature field theory framework, using Hard Thermal Loop resummed propagators for all gluons. The quark gluon plasma is assumed thermalized at temperature T and zero baryon density. Details of the computations can be found in the original papers [212, 213, 214].

The evaluation of the radiated gluon number distribution, at first order

in opacity and in the soft rescattering approximation, i.e. $\omega + q_0 \approx \omega$, leads to

$$\begin{aligned} x\frac{dN_g}{dx} = \frac{C_R\alpha_s}{\pi^2}\frac{L}{\lambda_{dyn}}\int dz\,\bar{\rho}(z)\int d^2\mathbf{q}\int d^2\mathbf{k}\frac{\mu^2}{\pi\mathbf{q}^2(\mathbf{q}^2+\mu^2)} \\ \times\ \frac{2(\mathbf{k}-\mathbf{q})}{(\mathbf{k}-\mathbf{q})^2+\chi^2}\left(\frac{(\mathbf{k}-\mathbf{q})}{(\mathbf{k}-\mathbf{q})^2+\chi^2}-\frac{\mathbf{k}}{\mathbf{k}^2+\chi^2}\right) \\ \times\ \left(1-\cos\left(\frac{(\mathbf{k}-\mathbf{q})^2+\chi^2}{2Ex}\Delta z\right)\right)\ . \end{aligned} \tag{4.1}$$

We remind $\chi^2 = M^2x^2 + m_g^2(1-x)$.

The effective dynamical mean free path λ_{dyn} is defined as $\lambda_{dyn}^{-1} \equiv 3\alpha_s T$. A quick comparison with the static equivalent Eq. (3.12) shows that the only changes in the radiated gluon number distribution involve the mean free path

$$\lambda_{stat} \Longrightarrow \lambda_{dyn}\ ,$$

and the interaction potential

$$\frac{\mu^2}{(\mathbf{q}^2+\mu^2)^2} \Longrightarrow \frac{\mu^2}{\mathbf{q}^2(\mathbf{q}^2+\mu^2)}\ .$$

The implications of these changes are profound: the absence of the μ^2 screening for soft momenta exchanges $\mathbf{q}$ makes the potential diverge and the mean free path vanish. In the limit of $\mathbf{q} \to 0$, in fact, each individual Feynman diagram diverges logarithmically. These singularities, however, cancel out after all the contributing diagrams to the energy loss are summed over, making

the result Eq. (4.1) finite.

The effective dynamical mean free path and its static counterpart are related by

$$\frac{1}{\lambda_{dyn}} = c(n_f)^{-1} \frac{1}{\lambda_{stat}} \ , \tag{4.2}$$

where $c(n_f)$ is a coefficient that depends on the number of effective quark flavors in equilibrium with the gluons in the plasma.

The combined effect of the enhanced cross section and reduced mean free path contributes to a remarkable increase of the energy loss in the dynamical framework, as already noted in [213]. In Fig. 4.1 we show the comparison between the static and dynamical gluon number integrated distributions for a plasma of temperature $\sim$ 250 GeV and size 5 fm. We assume a chemically equilibrated QGP with only gluonic degrees of freedom ($n_f = 0$, $c(n_f) = 0.73$). The fixed effective coupling α_s is set to 0.3.

The energy loss of the jet as a function of E and$L$ is presented in Fig. 4.2. The same features observed in the context of GLV are also present in the dynamical scenario, from the coherence physics that determines the quadratic or linear L dependence of $\Delta E/E$, to the similarity between light and charm quark jets across a broad range of energies and path lengths.

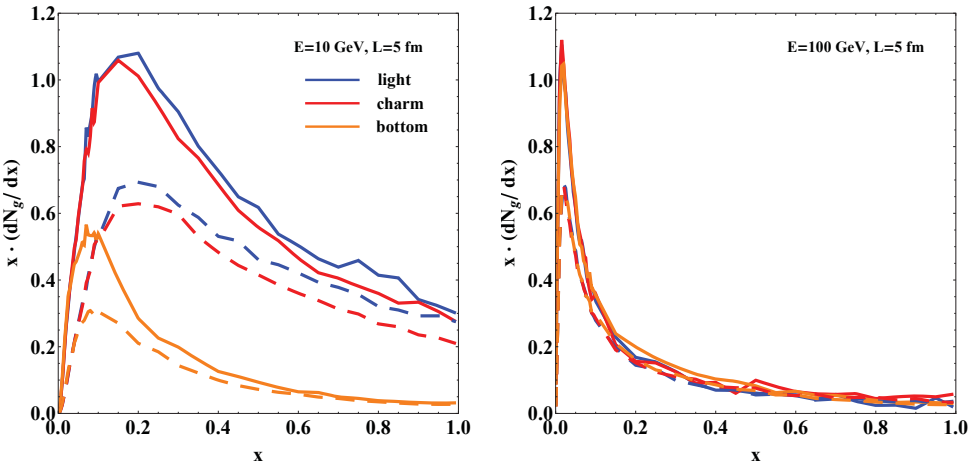

Figure 4.1: Comparison between dynamical (solid) and static (dashed) gluon number distribution, computed at first order in opacity. We show results for all quark flavors with initial energy equal to 10 GeV (*left*) or 100 GeV (*right*). We immediately observe that the radiation enhancement is strong, especially for low x gluons.

4.1.1 Light to heavy quark ratio

The dynamical model developed by Djordjevic predicts a jet energy loss which is remarkably higher than the one predicted by the static DGLV. This effect alone, on the other hand, could be equally obtained by the rescaling of the effective coupling α_s. In [213], however, it is suggested that the energy loss is enhanced is a mass dependent way.

In Fig. 4.3 we compute the ratio of light to bottom quark energy loss to study the effect that the inclusion of the dynamical model potentially has on flavor tomography. Bottom quark jets appear to be relatively more suppressed with respect to light ones in the dynamical framework, even though

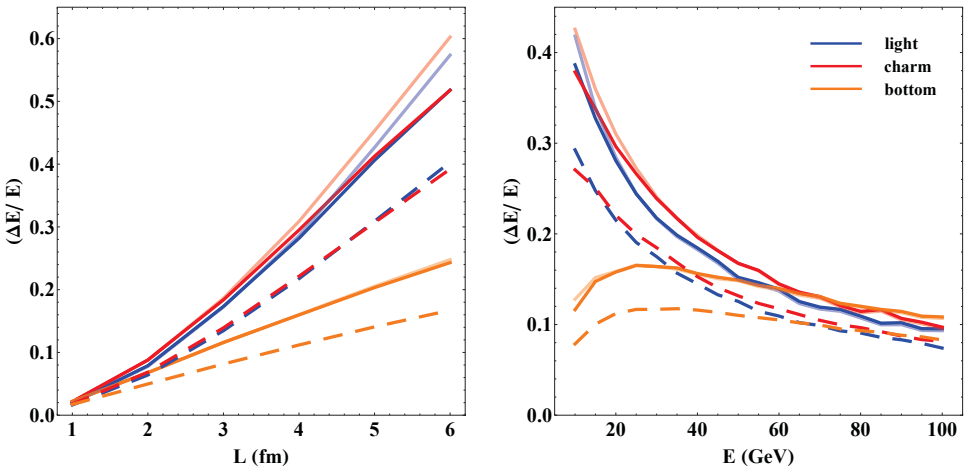

Figure 4.2: Energy loss $\Delta E/E$ for light, charm and bottom quark jets, computed in the dynamical framework at first order in opacity, including fluctuation effects (solid lines). Opaque curves represent the same dynamical computation without fluctuation effects (cf. Fig. 3.17), whereas dashed curves represent the DGLV results. *left* $E = 20$ GeV; *right* $L = 4$ fm

the effect is not large. Nevertheless, any contribution to heavy flavor quenching is welcome since current experimental results seem to contradict existing flavor tomography predictions made by static DGLV based models. Complete results will be presented in Chapter 6.

4.1.2 Hybrid potential

In the previous Chapter, we saw that the first order approximation to the GLV opacity expansion is sufficient for computing inclusive variables such as the energy loss. Is this true for the dynamical potential as well? In order to answer this question, an extension of the dynamical model to higher orders in

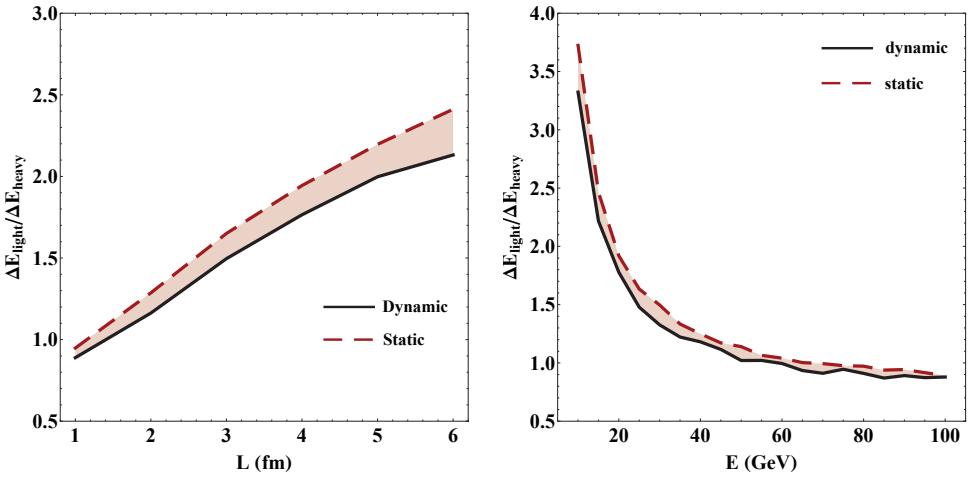

Figure 4.3: Energy loss ratio $\Delta E_{light}/\Delta E_{heavy}$ between light and bottom quarks, for dynamical (solid) and static (dashed) potential models, including fluctuations. *left* $E = 20$ GeV; *right* $L = 4$ fm. The light to heavy quark energy loss ratio is suppressed in the dynamical scenario for large L and small E, although this effects only accounts for an unimpressive $\sim 10 - 15\%$ reduction compared to DGLV.

opacity is needed. A direct comparison with the static DGLV model naively suggests

$$\lambda_{stat} \Longrightarrow \lambda_{dyn} \quad , \qquad \frac{\mu^2}{(\mathbf{q}^2+\mu^2)^2} \Longrightarrow \frac{\mu^2}{\mathbf{q}^2(\mathbf{q}^2+\mu^2)} \; ; .$$

Unfortunately, this simple prescription does not work.

We already noted that, as a consequence of the inclusion of dynamical effects, the elastic cross section diverge:

$$\frac{1}{\lambda} \equiv \rho(z)\sigma_{el} = \rho(z)\int d^2\mathbf{q}\frac{d\sigma_{el}}{d^2\mathbf{q}} \;\propto\; \int d^2\mathbf{q}\frac{1}{\mathbf{q}^2(\mathbf{q}^2+\mu^2)} \quad . \tag{4.3}$$

At first order in opacity, however, the infrared divergences disappear af-

ter resuming all the scattering diagrams. We then introduce a "magnetic" screening mass $\mu_m \equiv r_m \cdot \mu_e$ [32], where μ_e is the usual "electric" Debye mass and r_m a coefficient that interpolates between the static $r_m = 1$ and dynamical $r_m = 0$ limits. By developing the full opacity series for this hybrid model, we intend to study the limit for $r_m \to 0$ and observe the effects of higher order corrections to the $n = 1$ approximation of the dynamical model.

The hybrid approach involves replacing the normalized static Debye screened momentum distributions in the DGLV multiple collision kernel

$$\prod_{i=1}^{n} dz_i d\mathbf{q}_i \sigma_{el}(\bar{v}^2(\mathbf{q}_i) - \delta^2(\mathbf{q}_i))\rho(z_i) \quad , \tag{4.4}$$

with an effective normalized magnetic enhanced transverse distribution

$$\bar{v}^2(\mathbf{q}; r_m) = \frac{\mathcal{N}(r_m)}{\pi} \frac{\mu_e^2}{(\mathbf{q}^2 + \mu_e^2)(\mathbf{q}^2 + r_m^2 \mu_e^2)} \quad , \tag{4.5}$$

where $0 \leq r_m \equiv \mu_m/\mu_e \leq 1$ is the ratio of the color electric Debye and the assumed longer color magnetic screening lengths. The normalization factor

$$\mathcal{N}(r) = \frac{1 - r_m^2}{\log(1/r_m^2)} \tag{4.6}$$

reduces to unity when $r = 1$ but has a weak logarithmic zero for $r \to 0$. This zero is however canceled by the weak divergence of the effective elastic cross section $\sigma_{el}(r_m) = 9\pi\alpha_s^2/(2\mu_e^2\mathcal{N}(r_m))$. This no longer holds at opacity orders larger than one: the product of σ_{el} and $\delta^2(\mathbf{q})$ in Eq. (4.4), in fact, is

still divergent. Fortunately, in the finite-size quark gluon plasma produced in A+A reactions, r_m is bounded from below by $1/(\mu_e R_A)$ due to confinement of color outside the plasma.

In the development of the hybrid model, we ignore the contribution arising from the mean free path $\lambda_{dyn} = c(n_f)^{-1}\lambda_{stat}$. The coefficient $c(n_f)$, which varies from $c(0) = 0.73$ to $c(\infty) = 1.09$, does not contribute much to the energy loss compared to the magnetically enhanced potential. Besides, its effect on $\Delta E/E$ can be easily reproduced with a small rescaling of the effective coupling.

In Fig. 4.4, we show the energy loss ratio $\Delta E_l/\Delta E_b$ for three different values of the coefficient r_m and up to fifth order in opacity. For r_m approaching zero, it seems that higher order corrections to the $n = 1$ result assume increasingly more, albeit small, importance. The effect depends in a non-trivial way on the energy and the length of the medium, and future studies might address it in greater detail.

4.2 Elastic energy loss

The assumption that pQCD elastic losses are negligible compared to radiative ones was questioned in [17]: "The discrepancy between the DGLV Radiative only predictions and the data motivated us to revisit the assumption that pQCD elastic energy loss [150] is negligible compared to radiative.

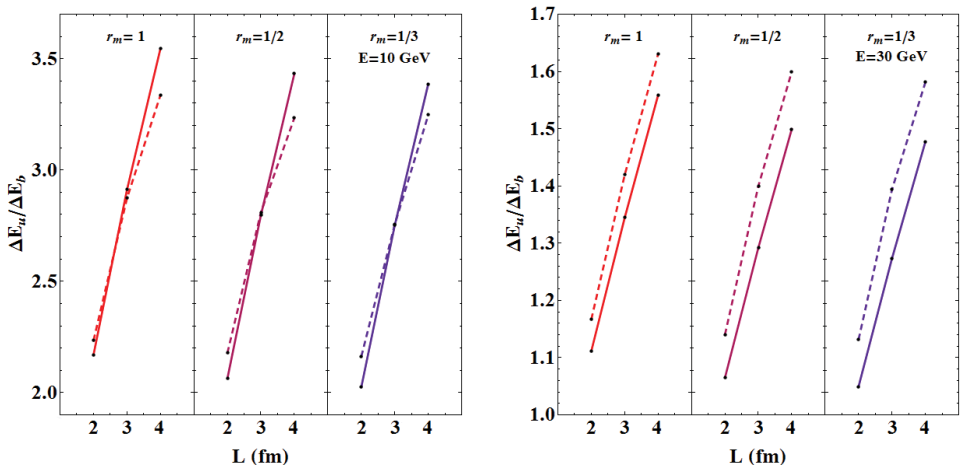

Figure 4.4: Energy loss ratio between light and bottom quarks as a function of L, for different values of $\mu_m = \mu_e, \mu_e/2$ and $\mu_e/3$ (left to right subpanels). Solid lines refer to the $n = 1$ approximation, dashed lines show instead computations up to fifth order in opacity. The left figure assumes $E = 10$ GeV, the right figure $E = 30$ GeV. The variation between $n = 1$ and $n = 5$ is never bigger than $\sim 5 - 10\%$.

[...] In contrast, Mustafa [168, 169] found that radiative and elastic average energy losses for heavy quarks were in fact comparable over a very wide kinematic range accessible at the Relativistic Heavy Ion Collider."

In [17], the authors confirm Mustafa's findings and extend them to the light quark sector, showing that elastic contributions to the total energy loss can be of the same order of magnitude of radiative ones.

It is obvious that quantitative tomographic predictions cannot ignore such large contribution to jet quenching, and elastic effects need to be included in CUJET as well.

4.2.1 Theoretical introduction

The first estimate for collisional energy loss in a quark gluon plasma was made by Bjorken [150], and his work still constitutes the benchmark against which any computation of this kind should be compared. Here we will briefly outline his derivation, and then introduce some of the more recent models that will be actually used in our computation.

In the limit $E \gg k$, where k the momentum of the target particle in the medium, we can approximate the quark-quark, quark-gluon and gluon-gluon elastic cross sections as

$$\frac{d\sigma_{i,j}}{d\hat{t}} = \frac{2\pi\alpha^2}{\hat{t}^2} c_{i,j} \quad , \tag{4.7}$$

where $c_{i,j}$ is a numerical factor equal to 4/9, 1, 9/4 for $\{i,j\} = \{q,q\}$, $\{q,g\}$ or $\{g,g\}$ respectively. The energy loss per unit length can be written as

$$\frac{dE}{dx} = \int d^3k \; \rho_i(k) \Phi \int_{\hat{t}_{MIN}}^{\hat{t}_{MAX}} d\hat{t} \frac{d\sigma_{i,j}}{d\hat{t}} \cdot (E - E') \quad . \tag{4.8}$$

Here $E - E'$ represents the energy lost in the collision, $\rho_i(k)$ is the quark or gluon number density, and Φ is the flux factor that accounts for the relative orientation of the target and projectile. Defining θ as the angle between the

incoming parton and the target,

$$\begin{aligned} E - E' &= -\frac{\hat{t}}{2k(1-\cos\theta)} \\ \Phi &= 1 - \cos\theta \ . \end{aligned} \tag{4.9}$$

Integrating (4.8) over $d\hat{t}$, we obtain

$$\frac{dE}{dx} = \int d^3k \ \rho_i(k) \left(-\frac{\pi\alpha^2}{k} c_{i,j} \log B \right) \ , \tag{4.10}$$

where B is defined by the integration limits $\hat{t}_{MAX}$ and $\hat{t}_{MIN}$. If we assume B independent of k for simplicity, we can set $\hat{t}_{MAX} \approx 2 \langle k \rangle E \approx 4TE$ and $\hat{t}_{MIN} = \mu^2$, the Debye screening mass of the plasma. If we further write the quark and gluon number densities as

$$\begin{aligned} \rho_q(k) &= \frac{12 n_f}{(2\pi)^3} \frac{1}{\mathrm{e}^{\beta \mathrm{k}} + 1} \\ \rho_g(k) &= \frac{16}{(2\pi)^3} \frac{1}{\mathrm{e}^{\beta \mathrm{k}} - 1} \ , \end{aligned} \tag{4.11}$$

we can perform the last integration over all momenta d^3k and finally get to the Bjorken energy loss formula

$$\frac{dE}{dx} = -\pi C_R \frac{\alpha^2}{\beta^2} \left(1 + \frac{n_f}{6} \right) \log B \ . \tag{4.12}$$

In order to derive this short analytic result, several approximations were made in the way infrared and ultraviolet divergences are being regulated, i.e.

$\hat{t}_{MIN}$ and $\hat{t}_{MAX}$. Such divergences, typical of the $1/t^2$ matrix element in the elastic cross section Eq. (4.7), are physically related to the lack of collective medium effects (soft scattering) and recoil (hard scattering) in the derivation of the theory.

The first improvement was made by Thoma and Gyulassy [215], who employed the use of hard thermal loop gluon propagators to provide a more natural infrared regulator. Their computation, which followed a classical scheme, leads to the following leading log result:

$$\frac{dE}{dx} = \frac{4\pi}{3} C_F \alpha_s^2 T^2 \left(\frac{1}{v} + \frac{v^2 - 1}{2v^2} \log \frac{1+v}{1-v} \right) \log \left(\frac{k_{max}}{\mu_D} \right) \quad . \tag{4.13}$$

For ultrarelativistic particles, the velocity v can be approximated to 1 and the v-dependent factor in parenthesis becomes 1. The integral over k is infrared finite due to the Debye screening mass in the denominator, but a maximal momentum k_{max} must be set in order to screen the otherwise ultraviolet divergent logarithm. Assuming that the maximal momentum transfer comes from forward scattering against target particles with average momenta $q \approx 2T$ – much smaller than the projectile momentum –, the value of k_{max} is $4Tp/(E - p + 4T)$.

We immediately see that this model yields a result very similar to the Bjorken computation, with only a different Coulomb log that reflects the

more natural cutoffs which are being used now:

$$\log\left(\frac{k_{max}}{\mu_D}\right) \equiv \log\left(\frac{4Tp}{(E-p+4T)\mu_D}\right) \quad . \tag{4.14}$$

Despite the improvement over the Bjorken result, the Thoma-Gyulassy model leaves the ultraviolet region unbounded, since their classical calculation has no knowledge of the particle nature of the medium and particle recoil, which becomes important when the momentum transfer q becomes large. The hard momentum transfer contribution is more naturally taken into account by Braaten and Thoma in [216, 217], although our analysis shows that the differences in practical applications are almost negligible.

Fluctuations of the elastic energy loss around the mean were addressed in [17] and [170]. Using a framework generally applied to diffusive processes that are characterized by a large number of soft collisions, the probability distribution to lose the collisional energy $\epsilon \equiv \Delta E/E$ is represented by a Gaussian centered around the average $\overline{\Delta E}$, with variance $\sigma^2 = 2T\overline{\Delta E}/E$:

$$P_{el}(\epsilon) = e^{-\overline{N}_c}\delta(\epsilon) + \mathcal{N}e^{-\frac{\epsilon-\bar{\epsilon}}{4T\epsilon}} \quad . \tag{4.15}$$

The first term represents the probability of no collisions, with $\overline{N}_c = \int dz\, \sigma_{el}\, \rho(z)$. The second term is the normalized Gaussian distribution centered

around $\bar{\epsilon} = \overline{\Delta E}/E$, with $\mathcal{N} = 1 - e^{-\overline{N}_c}$.

Once the $P_{el}(\epsilon)$ distribution is computed, a convolution with the radiative distribution $P_{rad}(\epsilon)$ (cf. Eq. (3.20)) gives the full fluctuation spectrum:

$$P(\epsilon) = \int dx \; P_{rad}(\epsilon) P_{el}(x - \epsilon) \;\; . \tag{4.16}$$

4.2.2 Numerical results

In Fig. 4.5 we observe the gain in $\Delta E/E$ after elastic collisions are taken into account. We notice three main features: (1) the energy loss is increased by up to 20%; (2) elastic losses almost do not distinguish between light and heavy quarks; (3) For sufficiently large L, $\Delta E/E$ shows signs of saturation, indicating complete quenching of the jets.

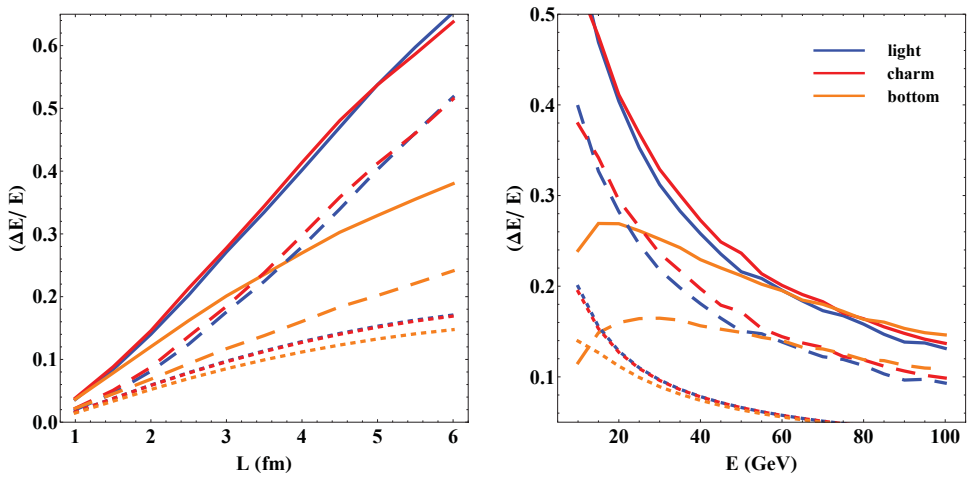

Figure 4.5: Radiative (dashed), Elastic (dotted) and total Radiative plus Elastic (solid) energy loss in a dynamical quark gluon plasma of size L. The plasma is thermalized at temperature ~ 250 MeV and characterized by only gluonic degrees of freedom ($n_f = 0$). Poisson fluctuations for the radiative part and Gaussian fluctuations for the elastic part are taken into account. *left* The energy is set equal to 20 GeV; *right* $L = 4$ fm. The dashed curves are the same as in Fig4.2.

The partial contribution of radiative and elastic losses to the total ΔE is given in Fig. 4.6, always assuming a dynamical medium. Here we immediately appreciate the difference between light and bottom quarks: while the relative elastic contribution diminishes with L and is approximately constant with E in the case of light partons, the exact opposite behavior is observed for heavy quarks. This has a remarkable impact on the phenomenology: the ratio $\Delta E_{light}/\Delta E_{heavy}$, shown in Fig. 4.7, drops by almost 25% in the large L and small E regions.

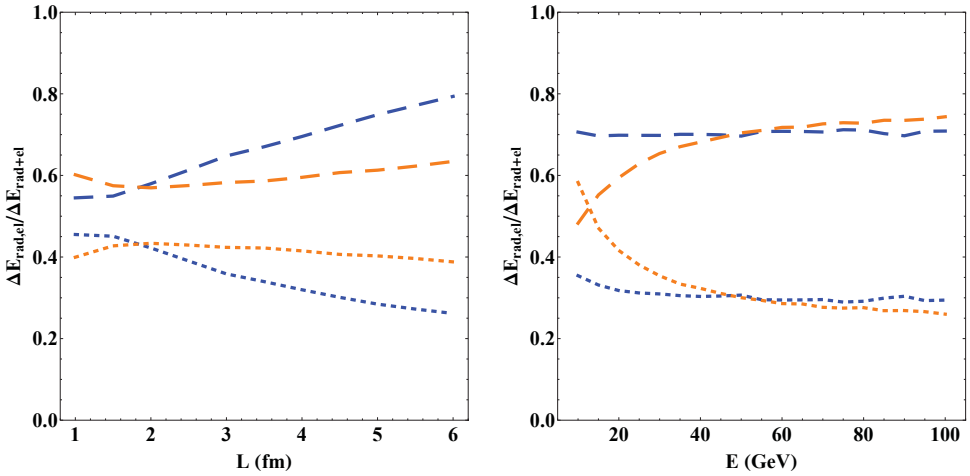

Figure 4.6: Ratio $\Delta E_{rad}/\Delta E_{rad+el}$ (dashed lines) and $\Delta E_{el}/\Delta E_{rad+el}$ (dotted lines), for light and bottom quarks. The ratios are computed starting from the results of Fig. 4.5. The dominant contribution to the total energy loss comes from inelastic collisions.

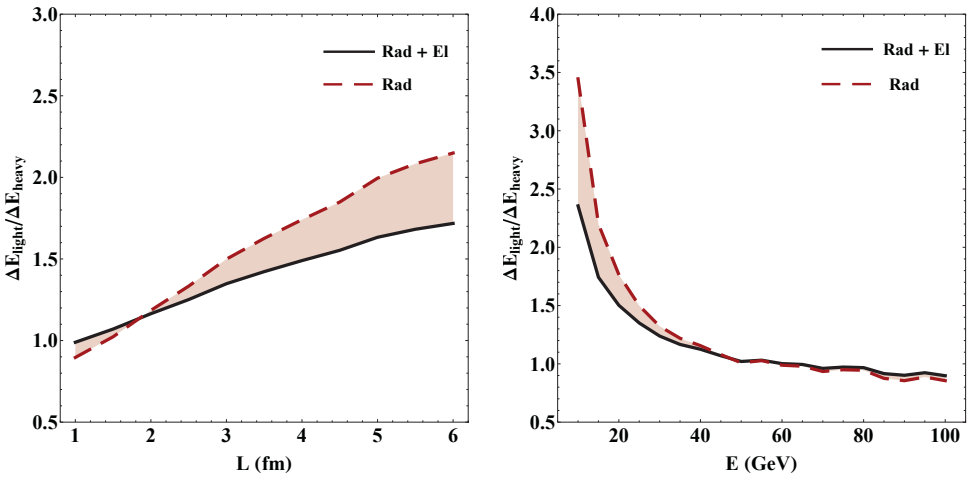

Figure 4.7: Light to bottom quark energy loss ratio, for radiative only (dashed) and total radiative plus elastic (solid) energy loss. The curves are obtained from the same data plotted in Fig. 4.5.

The inclusion of dynamical effects first, and elastic collisions later, has

brought the light to heavy quark energy loss ratio down from a factor of more than 2x to about 1.5x, in the range of energies $E \sim 10 - 30$ GeV and path lengths $L \sim 4 - 6$ fm.

These improvements constitute a promising step toward closing the gap between theoretical models and experimental data, which show at RHIC a surprising similarity between the quenching of light and heavy quark jets.

4.3 Jet path integration

In order to study the mechanics of any energy loss model, the simple brick approximation offers an ideal setup where results are not altered by complicated geometry assumptions. However, quantitative predictions of experimental data cannot ignore the effects due to the expansion and cooling of the medium. Previous phenomenological models, such as WHDG, included the longitudinal plasma expansion by evaluating a static non-uniform plasma density $\rho(\mathbf{x})|_{\tau=\tau_{MAX}/2}$ at a fixed proper time τ roughly equivalent to half the time of the plasma expansion [17].

Nevertheless, the non-trivial dependence of the energy loss on the temperature of the plasma, and the intricate interplay with the energy and mass of the jet, make any static geometry assumption a too-crude approximation to rely on when quantitative predictions are needed. Fig. 4.8 shows the dependence of $\Delta E/E$ on T for several choices of parameters E and L.

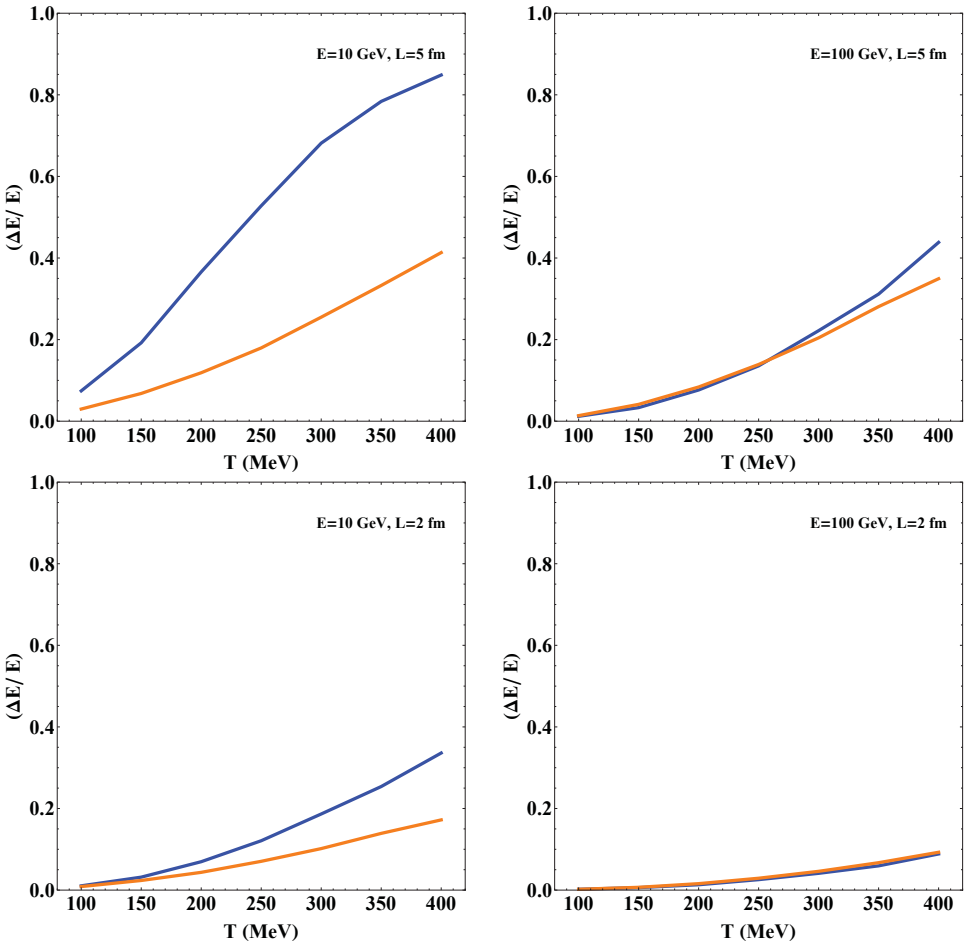

Figure 4.8: Energy loss $\Delta E/E$ for light and bottom quarks as a function of the temperature T of the plasma. Both dynamical potential and elastic contributions are considered. For different combinations of E and L, the temperature is increased in a range $[100, 400]$ MeV. Both the Debye mass $\mu = gT$ and the effective mean free path $\lambda_{dyn} = 3\alpha_s T$ are affected. $\Delta E/E$ scales approximately as T^3. When the relative energy loss approaches unity, saturation effects occur.

In order to account for generic space-time dependent plasma geometries, we need to define first the density profile $\rho_{QGP}(z)$. Here z represents the

longitudinal coordinate along the (straight) path of the jet, which is assumed transverse to the beam axis. In other words,

$$\rho_{QGP}(z) \equiv \rho_{QGP}(x_0 + \tau\cos\phi, y_0 + \tau\sin\phi; \tau)|_{\tau=z} \ , \tag{4.17}$$

where (x_0,y_0) and ϕ represent respectively the jet creation point and jet direction in the transverse plane. For simplicity, in $\rho_{QGP}(z)$ we omit the explicit dependence on $\mathbf{x}_0 \equiv (x_0,y_0)$ and ϕ.

In the GLV static medium, the opacity can be expressed as

$$\frac{L}{\lambda_{stat}} \ \longrightarrow \ \int dz\ \rho(z)\sigma_{el}(z) \ , \tag{4.18}$$

At higher orders,

$$\frac{1}{n!}\left(\frac{L}{\lambda_{stat}}\right)^n \ \longrightarrow \ \int_0^\infty dz_1\ \rho(z_1)\sigma_{el}(z_1)\ \cdots \int_{z_{n-1}}^\infty dz_n\ \rho(z_n)\sigma_{el}(z_n) \ . \tag{4.19}$$

If we expand the cross section into a gluon-quark and gluon-gluon term (remember that λ_{stat} is the *gluon* mean free path, thanks to the 'color triviality' proved in [166]), we obtain:

$$\frac{1}{\lambda_{stat}} = \sigma_{gq}(z)\rho_q(z) + \sigma_{gg}(z)\rho_g(z) = \frac{2\pi\ \alpha_s^2}{\mu^2(z)}\rho_q(z) + \frac{9}{4}\frac{2\pi\ \alpha_s^2}{\mu^2(z)}\rho_g(z) \ . \tag{4.20}$$

Taking $\mu = \left(gT\sqrt{1+n_f/6}\right)$ and assuming ideal gas conditions, from the

boson/fermions statistics we obtain

$$\begin{aligned} \rho_q(z) &= \frac{9n_f\zeta(3)}{\pi^2}T^3(z) \\ \rho_g(z) &= \frac{16n_f\zeta(3)}{\pi^2}T^3(z) \ . \end{aligned} \tag{4.21}$$

Combining the three together,

$$\frac{1}{\lambda_{stat}} = 18\frac{\pi\ \alpha_s^2}{\mu^2(z)}\frac{4+n_f}{16+9n_f}\rho(z) \equiv 3\alpha_s\ T(z)\left(6\frac{\zeta(3)}{\pi^2}\frac{1+n_f/4}{1+n_f/6}\right) \ , \tag{4.22}$$

with $\rho(z) = \rho_q(z) + \rho_g(z)$.

In the dynamical case, the definition of the effective mean free path becomes $\lambda_{dyn}^{-1} \equiv 3\alpha_s T$, as seen in Section 4.1. Comparing with the equations above, we can immediately derive the proportionality coefficient $c(n_f)$ between λ_{stat} and $\lambda_{dyn} = c(n_f)\lambda_{stat}$:

$$c(n_f) = 6\frac{\zeta(3)}{\pi^2}\frac{1+n_f/4}{1+n_f/6} \ . \tag{4.23}$$

We are now ready to substitute Eq. (4.22) into Eq. (3.12) and Eq. (4.1):

$$\begin{aligned} x\frac{dN_g^{STAT}}{dx} = &\frac{18C_R\alpha_s^3}{\pi^2}c_s(n_f)\int dz\ \rho(z)\int d^2\mathbf{q}\int d^2\mathbf{k}\frac{1}{(\mathbf{q}^2+\mu^2(z))^2} \\ &\times\ \frac{2(\mathbf{k}-\mathbf{q})}{(\mathbf{k}-\mathbf{q})^2+\chi^2(z)}\left(\frac{(\mathbf{k}-\mathbf{q})}{(\mathbf{k}-\mathbf{q})^2+\chi^2(z)} - \frac{\mathbf{k}}{\mathbf{k}^2+\chi^2(z)}\right) \\ &\times\ \left(1-\cos\left(\frac{(\mathbf{k}-\mathbf{q})^2+\chi^2(z)}{2Ex}z\right)\right) \ , \end{aligned} \tag{4.24}$$

$$x\frac{dN_g^{DYN}}{dx} = \frac{18C_R\alpha_s^3}{\pi^2}c_d(n_f)\int dz\;\rho(z)\int d^2\mathbf{q}\int d^2\mathbf{k}\frac{1}{\mathbf{q}^2(\mathbf{q}^2+\mu^2(z))} \times \frac{2(\mathbf{k}-\mathbf{q})}{(\mathbf{k}-\mathbf{q})^2+\chi^2}\left(\frac{(\mathbf{k}-\mathbf{q})}{(\mathbf{k}-\mathbf{q})^2+\chi^2(z)}-\frac{\mathbf{k}}{\mathbf{k}^2+\chi^2(z)}\right) \times \left(1-\cos\left(\frac{(\mathbf{k}-\mathbf{q})^2+\chi^2(z)}{2Ex}z\right)\right)\;, \tag{4.25}$$

with

$$\begin{aligned} c_s(n_f) &= \frac{4+n_f}{16+9n_f} \\ c_d(n_f) &= 9\frac{(4+n_f)^2}{(6+n_f)(16+9n_f)}\frac{\zeta(3)}{\pi^2}\;. \end{aligned} \tag{4.26}$$

The ability to perform the full jet path integration allows in first place the study of several dynamical features of the plasma evolution. In second place, it also permits the study of different initial thermalization and final hadronization assumptions by measuring their impact on the energy loss. Most of these aspects will be object of detailed analysis in the next Chapter.

4.4 Running coupling

The inclusion of (strong) running coupling effects into our model of energy loss was naturally motivated be the extended energy range probed in heavy ion collisions at LHC.

Previous attempts to consider running coupling effects were already made, in particular by Zakharov [218, 219]. The coupling constant $\alpha_s(Q^2)$ is parametrized by the one-loop expression and it is assumed to saturate at some

value α_0 for $Q \leq Q_0$.

$$\alpha_s \longrightarrow \alpha_s(Q^2) = \begin{cases} \alpha_0 & \text{if } Q \leq Q_0 \\ \dfrac{2\,\pi}{9\,\log(Q/\Lambda_{QCD})} & \text{if } Q > Q_0 \end{cases} \tag{4.27}$$

The choice of α_0 is not straightforward: indications of $\alpha_0 \approx 0.7$ come from the analysis of the heavy quark energy loss in vacuum [220]. However, in the QGP, thermal partons can give additional suppression of α_s at low momenta and lattice simulations [221] predict the thermal $\alpha_s(T)$ smoothly decreasing from 0.5 at $T \sim 175$ MeV to 0.35 at $T \sim 400$ MeV. Since these are only mean values, α_0 is expected to be somewhat bigger than that: in the absence of robust theoretical predictions for the in-medium α_s, Zakharov chooses $\alpha_0 = 0.7, 0.5, 0.4$ for different scenarios in his analysis.

Our approach consists of letting the strong coupling running in accordance to Eq. 4.27. We identify , in Eq. 4.24 and 4.25, three distinct scales Q^2 with which different powers of $\alpha_s(Q^2)$ scale. Assuming the scale is set by the exchanged four-momentum in the relevant Feynman vertex, we have:

1. Two powers $\alpha_s^2(Q^2)$ originate from the jet-medium interaction vertices; the exchanged momentum is q, and $Q^2 = q^2$.

2. One power $\alpha_s(Q^2)$ originates from the radiated gluon vertex; the ex-

changed momentum is the Mandelstam variable $\hat{t}$ [222] and

$$Q^2 = \hat{t}^2 \approx \frac{k_\perp^2}{x(1-x)} + \frac{M_q^2}{1-x} + \frac{m_g}{x} \quad . \tag{4.28}$$

3. One power of the thermal coupling originates from the Debye mass $\mu(\alpha_s(Q^2); T)$; we set the scale proportional to the temperature of the plasma, $Q^2 = (2T)^2$.

In the choice of running scales there is no explicit dependence on the jet energy, which comes instead from the kinematic limits of the $\mathbf{q}$ and $\mathbf{k}$ integrations. We extensively discussed the $k_\perp^{MAX} = xE$ limit in Section 3.10, but only briefly mentioned the $q_\perp^{MAX} = \sqrt{4ET}$ limit in Section 3.1.1. Since the integrand peaks at small values of $q_\perp$, the upper kinematic bound has always been neglected, allowing the application of the importance sampling method to our Monte Carlo algorithm. This is no longer possible, as long as we want to analyze the running coupling effects on jet tomography at LHC.

As a final note, the free parameter of the theory usually identified with the coupling constant α_s is now replaced by its saturation value α_0. In the next Chapter we will perform extensive studies to quantify the theoretical systematic uncertainties attributable to the choice of running scale Q^2.

4.4.1 The a-b-c model

We quantify the impact that the running coupling has on jet quenching by taking a novel approach based on the work by Gyulassy and Horowitz. In

[223], the authors develop a simple power law model for jet energy loss

$$\frac{dP}{d\tau} = -\kappa P^a \tau^b T^{2-a+b} \quad , \tag{4.29}$$

where $P(\tau)$ corresponds to the momentum of a massless jet passing though a plasma characterized by a local temperature T. The power of T is constrained by simple dimensional analysis, and the index a and b are set by the asymptotic LPM behavior of the *GLV* model:

$$\frac{\Delta E}{E} \propto T^3 L^2 \frac{\log(E/T)}{E} \quad . \tag{4.30}$$

For the range of energies of interest, we can approximate the $\log(E/T)/E$ dependence as E^a, with $a \sim 1/3 - 1/4$.

In Fig. 4.9 we show the value of the index a as a function of the jet energy E, for five different cases: α_s fixed, only $\alpha_s(4T^2)$ running, only $\alpha_s^2(q_\perp^2)$ running, only $\alpha_s(k_\perp^2/(x(1-x))$ running and finally all couplings running. In this example, we use for the first time a non-uniform density profile that approximate the thermal medium formed in a Pb+Pb collision at LHC (cf. next Chapter for more details). The results are insightful:

- As expected, the fixed case shows $a \sim 1/3 - 1/4$.
- By introducing the thermal coupling, only the absolute value of the energy loss is affected and the energy dependence of the index remains unaltered. The scale at which the thermal alpha is evaluated is in

fact independent of E. Not noticeable in this plot, at very high temperatures the reduced thermal coupling causes a stronger quenching compared to the fixed coupling case, since the smaller Debye mass diminishes the screening in the plasma. This running effect is however small: for most of the temperature ranges, $alpha_s$ is in fact equal to the saturated value α_0 (with $Q_0 \sim 1$ GeV, T needs to be greater than 0.6 GeV to start feeling the running effects).

- The couplings $\alpha_s^2(q_\perp^2)$ and $\alpha_s(k_\perp^2/(x(1-x))$ sensibly reduce the dependence of $\Delta E/E$ on E, and as a consequence the value of the index a gets smaller and closer to 0. The $\alpha_s^2(q_\perp^2)$ contribution is smaller since the $q_\perp$ distribution is peaked at small values of $q_\perp$, as opposed to the $\alpha_s(k_\perp^2/(x(1-x))$ contribution which is larger due to the high tails of the $k_\perp$ distribution.

- The all-running case shows almost no dependence of $\Delta E/E$ on E, and $a(E) \approx 0$. The phenomenological implications of this effect will be emphasized in Chapter 6.

Finally, we include for completeness running coupling effects also in the elastic portion of the energy loss, even though the contribution to the final result is very limited. In doing this, we closely follow the work of Peigné and Peshier [224]: both powers of α_s in Eq. (4.7) run with $\hat{t}$, and when integrated

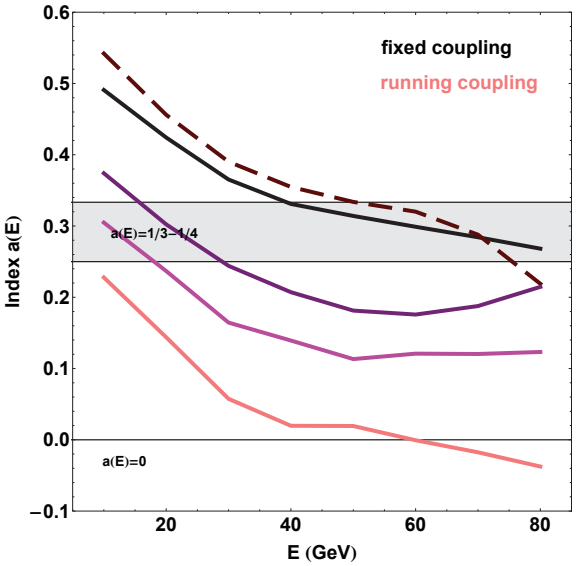

Figure 4.9: Index $a(E)$ (cf. Eq. (4.29)) for different assumptions of the running coupling: fixed effective $\alpha_s = 0.3$ (black), only thermal coupling running (dashed red), only $\alpha_s^2(q_\perp^2)$ running (purple), only $\alpha_s^2(k_\perp^2/(x(1-x)))$ running (magenta), all couplings running (pink). The saturated α_0 value is chosen equal to 0.4, which corresponds to approximately $Q_0 \sim 1$ GeV. The plot shows the energy loss of a light quark traveling through a gluonic plasma of size 5 fm. The density profile resembles the medium created in a Pb-Pb head-on collision.

over $d\hat{t}$ in Eq. (4.8), we obtain

$$\alpha_s^2 \int_{\mu^2}^{4ET} \frac{d\hat{t}}{\hat{t}} \longrightarrow \int_{\mu^2}^{4ET} \frac{d\hat{t}}{\hat{t}} \alpha_s^2(\hat{t}) \ , \tag{4.31}$$

$$\alpha_s^2 \log \frac{4ET}{\mu^2} \longrightarrow \alpha_s(\mu^2)\alpha_s(4ET) \log \frac{4ET}{\mu^2(\alpha_s(4T^2);T)} \ . \tag{4.32}$$

Here the values of $\hat{t}_{MIN}$ and $\hat{t}_{MAX}$ are chosen according to the Bjorken computation of elastic energy losses. In the CUJET model, the argument of the

logarithm is modified according to the Thoma-Gyulassy model.

4.5 Conclusions

In this Chapter we presented several improvements that distinguish CUJET from existing models similarly based on the GLV opacity expansion:

- The inclusion of dynamical magnetic effects at first order in opacity greatly enhances the energy loss of a parton in the medium. The development of a hybrid potential which assumes the existence of a non-vanishing "magnetic" screening mass allows the computation of the energy loss at arbitrary order in opacity.

- The combined effect of the effective dynamical potential and the inclusion of collisional energy loss reduces the discrepancy between light and heavy quark jet quenching.

- The full jet path proper time integration over space-time dependent plasma geometries opens the possibility to evaluate systematic theoretical uncertainties such as sensitivity to formation and decoupling phases of the QGP evolution, local running coupling and screening scale variations, and other dynamical effects out of reach with analytic approximation.

- The inclusion of running coupling effects reduces the asymptotic logarithmic dependence of ΔE on E (see Eq. (2.19)) to an almost constant

value, with remarkable consequences on the phenomenology at LHC.

Chapter 5

Development of CUJET

It is now time to introduce the CUJET model and describe its development in great detail, starting from the early stages of the collision and ending with the fragmentation of the quenched jets.

In Section One, we show how CUJET models the quark gluon plasma assuming a 1D+1 hydrodynamical expansion. Particular attention is dedicated to the description of the initial conditions, namely the Glauber density profile and the pre-thermalization phase.

In Section Two, we describe the jet quenching process: creation of the jets; evolution of the jets in the medium with consequent energy loss; fragmentation of the jets.

Finally, in Section Three, we define and compute the nuclear modification factor R_{AA}. For the first time, CUJET will applied to the computation of an experimental observable and will be extensively tested.

5.1 Modeling of the plasma

In Chapter 1 we described the initial stages of the collision in terms of color glass condensate and glasma states. In this section we want to focus on the kinematics of the event and some relevant experimental observations.

The naive picture of two Lorentz-contracted nuclei that collide head-on into each other and melt into a plasma of nucleon constituents is replaced at very high energies ($\sim$ 200 AGeV) by the more sophisticated Bjorken picture, where sea quarks and gluons play a determining role. The wee partons have a much smaller momentum fraction (x) of the nucleon compared with the valence quarks, and their number increases as x approaches zero. Because of their non-perturbative nature, the typical momentum p of wee partons is of order Λ_{QCD}, and according to the uncertainty principle the longitudinal size of a nucleus cannot shrink beyond $\Delta Z \sim p^{-1} \sim 1$ fm.

When two highly energetic nuclei collide, the stopping power is not sufficient to bring the valence quarks at rest: the two Lorentz-contracted pancakes swipe through each other unharmed and leave behind a strain of excited virtual quanta that soon de-excite into real quarks and gluons. If the proper time needed for the excitations to de-excite is τ, in the center of mass framework the real quanta are seen emerging at $t = \gamma\tau$ along a constant proper time hyperbola $\tau = \sqrt{t^2 - z^2}$, as shown in Fig. 5.1. This phenomenon takes the name of *inside-outside cascade* and an immediate consequence is that slow particles emerge first near the collision point, while fast particles emerge last

and far from it.

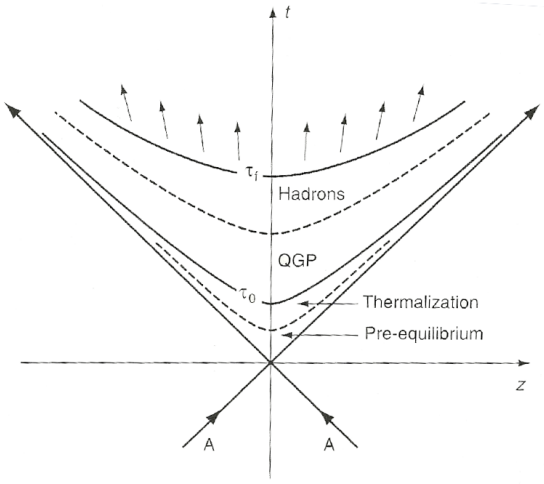

Figure 5.1: Minkowski diagram representing the evolution of the plasma according to the Bjorken picture. τ_0 is the time it takes for the system to reach thermalization, whereas τ_f is the instant when the system hadronizes.

Since in the central region the evolution of the plasma is invariant under boost transformations, physical properties such as energy and entropy density depend only on τ. The constant τ hyperbolas in Fig. 5.1 can be used to distinguish between the different phases of the collision evolution.

Useful information about the collision dynamics can be extracted from the distribution of net baryons, i.e. the difference between baryons and antibaryons. The region interested by the de-excitation of the virtual quanta is mostly baryon-free and is characterized by an approximately constant average multiplicity per rapidity interval, dN/dy, which forms a central boost-

invariant plateau in the rapidity distribution of hadrons.

At higher rapidities, instead, the particle production is subject to the contribution from the original baryon content of the colliding nuclei. This phenomenon is the signature of a high energy collision: at lower $\sqrt{s}$, in fact, the nuclear stopping power is strong enough to stop the baryon-rich nuclei, and the net-baryon rapidity distribution spikes near the central value $y = 0$ (Fig. 5.2).

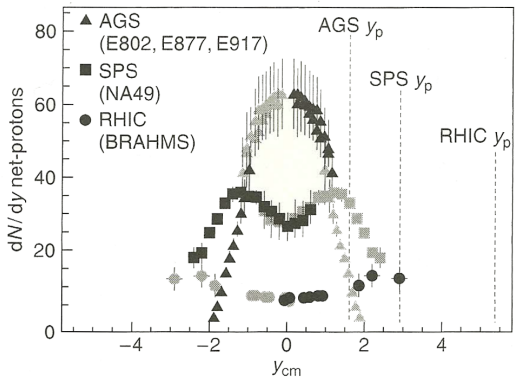

Figure 5.2: Comparison of the net-baryon (proton) rapidity distributions at AGS ($\sqrt{s_{NN}} = 5$ GeV Au+Au), SPS ($\sqrt{s_{NN}} = 17$ GeV Pb+Pb) and RHIC ($\sqrt{s_{NN}} = 200$ GeV Au+Au). Taken from Bearden et al. (2004). At low energy, the colliding nuclei almost reach a halt resulting in a peak of the net-barion distribution at mid rapidity. The more energetic the collision is, the more transparent the nuclei become. The height and width of the central plateau seen at RHIC depend on the center-of-mass energy of the collision and the nuclear mass number.

At very early times, the matter created during the collision is characterized by extremely high energy densities. While it expands and the gluon

density decreases, the interaction strength among particles increases facilitating the thermalization process into what is known as quark gluon plasma. The time scale over which the thermalization process takes place is generally referred to as τ_0 and is assumed to be approximately equal to $\sim 0.5-1$ fm/c.

Once the plasma has reached the thermalized stage, the system can be approximated by a fluid and its evolution computed in the framework of relativistic hydrodynamics. The fundamental equations of energy-momentum and baryon number conservation are assumed to hold.

5.1.1 Glauber model

The geometry of the collision, the plasma density profile and the jet production point distribution are given in CUJET by the Glauber model [122]. In particular, the density profile is proportional to the distribution of participant nucleons in the reaction.

The thickness function of the nucleus A is defined as

$$T_A(\mathbf{x}) = \int dz\ \rho_A(z, \mathbf{x}) \ , \tag{5.1}$$

with the density profile of the nucleus given by the Woods-Saxon parametrization

$$\rho_A(r) = \frac{\mathcal{N}_\mathcal{A}}{1 + \exp((r-R)/a)} \ . \tag{5.2}$$

The density is normalized to the mass number A, R is the nuclear radius and a represents the surface thickness. Typical values used in Au+Au (RHIC)

and Pb+Pb (LHC) collisions are:

	A	R (fm)	a (fm)	σ_{in} (mb)
Au	197	6.37	0.535	42
Pb	207	6.48	0.535	63

Table 5.1: Woods-Saxon parameters used in CUJET.

With σ_{in} the inelastic nucleon-nucleon cross section, the distribution of participants in a collision between two nuclei A and B that collide with impact parameter $\mathbf{b}$ is given by

$$\begin{aligned} \rho_{part}(\mathbf{x},b) =& T_A(\mathbf{x})\left(1-\mathrm{e}^{-\sigma_{in}T_B(\mathbf{x}-\mathbf{b})}\right) \\ &+ T_B(\mathbf{x}-\mathbf{b})\left(1-\mathrm{e}^{-\sigma_{in}T_A(\mathbf{x})}\right) \\ N_{part}(b) =& \int d\mathbf{x}\ \rho_{part}(\mathbf{x},b)\ \ . \end{aligned} \tag{5.3}$$

The proportionality constant between the transverse QGP density profile $\rho_{QGP}(\mathbf{x},b)$ and $N_{part}(\mathbf{x},b)$ is given by the gluon density

$$\frac{dN_g}{dy} = \frac{3}{2}\frac{dN_{ch}}{dy}\ \ , \tag{5.4}$$

where dN_{ch}/dy represents the measured charged-hadrons rapidity distribution. As we can see, if we relate the total number of particles observed in a given volume to the plasma density ρ_{QGP}, we obtain:

$$\rho_{QGP}\ d^3x = \frac{dN_g}{dy}\ dy\ \ . \tag{5.5}$$

By defining the proper time $\tau = \sqrt{t^2 - z^2}$ and the rapidity $y = \frac{1}{2}\log\left(\frac{t+z}{t-z}\right)$, the volume element d^4x becomes $d^4x = \tau\, d\tau\, dy\, r\, dr\, d\phi$, and we can rewrite Eq. (5.5) as:

$$\rho_{QGP,0}\, \tau_0\, dy\, \pi R^2 = \frac{dN_g}{dy}\, dy \;\longrightarrow\; \rho_{QGP,0} = \frac{1}{\pi R^2 \tau_0}\, \frac{dN_g}{dy} \quad . \tag{5.6}$$

The density $\rho_{QGP,0}$ is measured at a given proper time τ_0, here chosen as the time it takes for the system to reach thermalization. Instead of the uniform $1/\pi R^2$ distribution, we can finally substitute the normalized participant density and write

$$\rho_{QGP,0}(\mathbf{x}, b) = \frac{1}{\tau_0}\, \frac{\rho_{part}(\mathbf{x}, b)}{N_{part}(b)}\, \frac{dN_g}{dy} \quad . \tag{5.7}$$

The jet production points are distributed according to the binary collision distribution, given by

$$\begin{aligned} \rho_{binary}(\mathbf{x}, b) =& \sigma_{in}\, T_A(\mathbf{x}) T_B(\mathbf{x} - \mathbf{b}) \\ N_{binary}(b) =& \int d\mathbf{x}\, \rho_{binary}(\mathbf{x}, b) \quad . \end{aligned} \tag{5.8}$$

5.1.2 Bjorken expansion

CUJET computes the time evolution of the plasma density profile ρ_{QGP} according to the Bjorken picture. A simple analytical expression is obtained by making few assumptions: (1) the system expands only longitudinally,

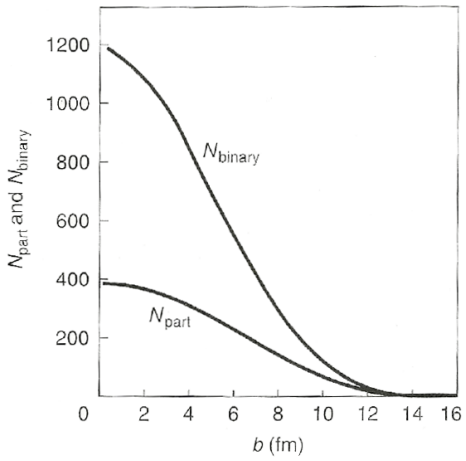

Figure 5.3: Number of binary collisions and number of participant nucleons as a function of the impact parameter in a Au+Au collision.

along the beam direction (1D+1 expanding plasma); (2) the plasma is a perfect fluid; (3) the computation is carried out in a relativistic hydrodynamical framework.

In the local comoving frame of the fluid, the energy-momentum tensor takes the form

$$T^{\mu\nu}(x) = \mathrm{Diag}(\epsilon(x), p(x), p(x), p(x)) \ . \tag{5.9}$$

In this rest frame, the fluid velocity is simply given by $u^\mu = (1, 0, 0, 0)$. In the center-of-mass frame, however, $u^\mu(x) = \gamma(1, 0, 0, v(z))$ and $T^{\mu\nu}$ becomes

$$T^{\mu\nu}(x) = (\epsilon + p)u^\mu u^\nu - g^{\mu\nu}p \ . \tag{5.10}$$

Starting from the conservation laws of the energy-momentum tensor and baryon number current density

$$\begin{aligned} \partial_\mu T^{\mu\nu}(x) &= 0 \\ \partial_\mu j_B^\mu(x) = \partial_\mu(n_B(x)u^\mu(x)) &= 0 \quad , \end{aligned} \tag{5.11}$$

we obtain the conservation law for the entropy current density if we contract u_ν with the first equation and then plug in the second equation. The result is:

$$\partial_\mu(s(x)u^\mu(x)) = 0 \quad . \tag{5.12}$$

It the Bjorken picture, thermalization happens during the very early stages of the collision, and particles are seen originating from the same point, with an initial velocity that remains constant during the evolution (free stream). According to this picture, the four-velocity can be rewritten as

$$u^\mu = \gamma(1,0,0,v_z) \;\longrightarrow\; \frac{t}{\tau}(1,0,0,\frac{z}{t}) = (\cosh y, 0, 0 \sinh y) \quad . \tag{5.13}$$

Consequently, after transforming $\partial_t, \partial_z \to \partial_\tau, \partial_y$, we have

$$u_\mu \partial^\mu = \partial_\tau \quad , \qquad \partial^\mu u_\mu = 1/\tau \quad , \tag{5.14}$$

and Eq. (5.12) becomes

$$\frac{\partial s(\tau, y)}{\partial \tau} = -\frac{s(\tau, y)}{\tau} \quad . \tag{5.15}$$

This is easily solved to give

$$s(\tau, y) = s(\tau_0, y)\frac{\tau_0}{\tau} \quad . \tag{5.16}$$

Eq. 5.16 shows the temporal evolution of the entropy density in a longitudinally expanding plasma. For an ideal fluid, the following relations hold among the number density, energy density, pressure density and entropy density:

$$\begin{aligned} \rho(\mathbf{x}) &= \sum \frac{\zeta(3)}{\pi^2} g_i \eta_i T^3(\mathbf{x}) \\ \epsilon(\mathbf{x}) &= \sum \frac{\pi^2}{30} g_i \eta_i' T^4(\mathbf{x}) \\ p(\mathbf{x}) &= \epsilon(\mathbf{x})/3 \\ s(\mathbf{x}) &= \frac{p(\mathbf{x}) + \epsilon(\mathbf{x})}{T} \approx \kappa \rho(\mathbf{x}) \quad , \end{aligned} \tag{5.17}$$

where $g_i = (16, 12n_f)$, $\eta_i = (1, 3/4)$, $\eta_i' = (1, 7/8)$, depending on whether $i = (g, q)$ (gluons, quarks) respectively. The constant κ ranges from 3.6 to 3.1 depending on the value of n_f. From the last relation, we can immediately determine the τ dependence of the quark gluon plasma density profile:

$$\rho_{QGP}(\mathbf{x}, b, \tau)|_{y=0} = \frac{1}{\tau_0} \frac{\rho_{part}(\mathbf{x}, b)}{N_{part}(b)} \left.\frac{dN_g}{dy}\right|_{y=0} f(\tau/\tau_0) \quad , \tag{5.18}$$

with

$$f(\tau/\tau_0) = \frac{\tau_0}{\tau} \quad . \tag{5.19}$$

For most of the practical applications, we will concentrate on the mid-rapidity region of the collision ($y = 0$), characterized by longitudinal boost invariance.

5.1.3 Formation time physics

Eq. 5.18 diverges in the limit $\tau \to 0$ and we need to choose a thermalization time τ_0 to run the evolution from there on. What happens for $\tau < \tau_0$ though? How does a high energy jet couple before it's thermalized? In the absence of a clear theoretical answer, we need to make a phenomenological assumption.

We parametrize the temporal evolution of the system in three different ways:

1. The plasma takes a proper time τ_0 to thermalize, while the density "seen" by the jet grows linearly until thermalization is reached. The density decreases as $1/\tau$ thereafter. Referring to Eq. (5.19),

$$f(\tau/\tau_0) = \begin{cases} \tau/\tau_0 & \text{if } \tau \leq \tau_0 \\ \tau_0/\tau & \text{if } \tau > \tau_0 \end{cases} \tag{5.20}$$

2. The jet "sees" a divergent density at $\tau = 0$ that decreases with $1/\tau$

(instant thermalization).

$$f(\tau/\tau_0) = \frac{\tau_0}{\tau} \tag{5.21}$$

3. The jet doesn't couple with the medium until the plasma has thermalized (free streaming).

$$f(\tau/\tau_0) = \begin{cases} 0 & \text{if } \tau \leq \tau_0 \\ \tau_0/\tau & \text{if } \tau > \tau_0 \end{cases} \tag{5.22}$$

Our standard choice for τ_0 is $\tau_0 = 1$ fm/c. In Fig. 5.4, we illustrate the time evolution of the QGP density.

Fig. 5.5 shows instead how differently light and heavy quarks lose energy due to elastic and inelastic collisions during the early stages of the plasma longitudinal expansion. For jets produced in central Au+Au events, the differential $d < \Delta E/E > /dz$ indicates the fractional energy loss during the first fermi of the jet evolution. Heavy quarks appear to lose a larger percentage of their energy via radiative processes in the time that immediately precedes and follows the medium thermalization.

The mass-dependent jet behavior observed in Fig. 5.5 could be used as a phenomenological indicator of the thermalization mechanics. For different parametrizations of $f(\tau/\tau_0)$ one could expect a different relative yield between light and heavy quark jets. This fact is portrayed in Fig. 5.6, where

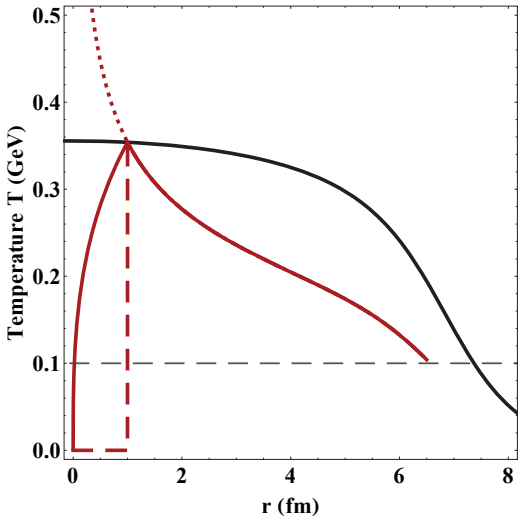

Figure 5.4: Temperature profile of the QGP in a central ($b = 0$) collision at RHIC energies. The density is constrained by the observed $dN/dy = 1000$. The black curve represents the temperature at constant $\tau_0 = 1$ fm/c for a radial section of plasma. The red curves represents the $1/\tau^{1/3}$ temperature probed by a quark that is created at $r = 0$ and propagates outward along $z \equiv r$ (with the solid, dotted and dashed curves representing the linear, divergent and free streaming cases respectively). The dashed black $T \approx 100$ MeV line corresponds to the fragmentation temperature of the jet.

the ratio $\Delta E_{light}/\Delta_{bottom}$ is given as a function of L for all possible temporal envelopes.

5.1.4 Future developments

In Fig. 5.4, we showed the smooth temperature profile of a symmetric plasma. The shape of the region interested by the collision takes the form of a perfect circle when the impact parameter is null, or an almond when $b \neq 0$.

The reality, however, is different. Nuclear matter is very granular at short

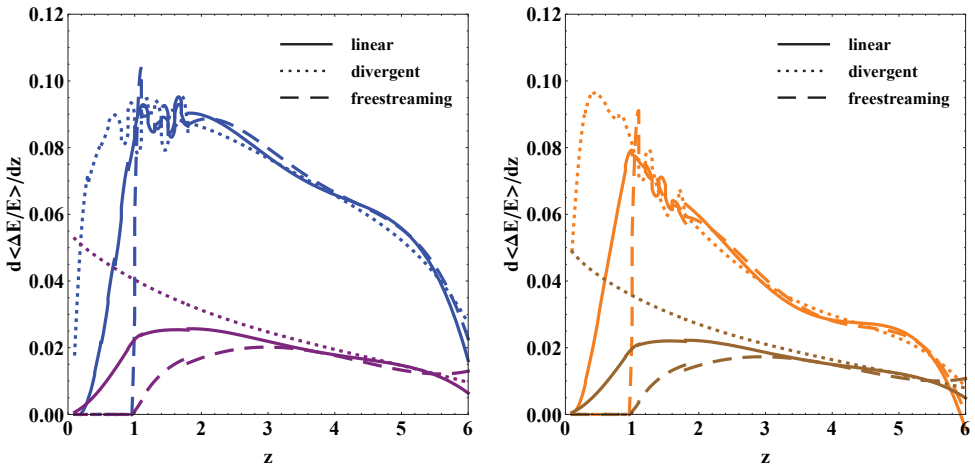

Figure 5.5: Differential $d < \Delta E/E > /dz$ for light (*left*) and heavy (*right*) quarks, in a QGP defined by $dN/dy = 1000$, $\tau_0 = 1$ fm/c and $n_f = 0$. The initial energy of the quarks is 20 GeV. Blue and orange colors refer to radiative losses, whereas purple and brown to elastic ones. Notice how quickly $d < \Delta E/E > /dz$ drops for heavy quarks compared to light jets. LPM interference effects are responsible for the finite value of the energy loss at very short z in the divergent plasma scenario.

distances, and the nucleons are not distributed in a perfectly symmetrical way. The naive picture of a circle or an almond is most of the time an idealization of the collision geometry, and the identification of a reaction plane determined by the orientation of the impact parameter is often a hard experimental task. If the average over multiple collisions might lead to a smooth temperature profile, this is not the case on an event-by-event basis, where fluctuations over initial conditions might lead to considerably different results.

Also the full three-dimensional hydrodynamic expansion differs substantially from the Bjorken 1D+1 evolution presented in the previous Section.

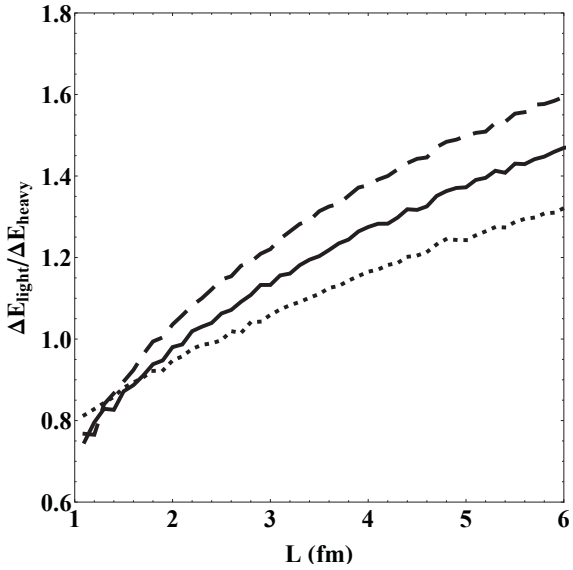

Figure 5.6: Energy loss ratio $\Delta E_{light}/\Delta E_{heavy}$ as a function of L between light and bottom quarks, for the three linear (solid), divergent (dotted) and free streaming (dashed) initial conditions. The energy loss is obtained by integrating the curves in Fig. 5.5 up to $z = L$. For sufficiently long path lengths, the relative difference between the three approximations reaches approximately 10%.

Besides the obvious inclusion of the transverse expansion, a complete description of the system needs to consider viscous corrections to the perfect fluid. Furthermore, other effects such as initial condition fluctuations or jet energy deposition into the medium should be considered as well.

CUJET, by evolving the plasma only longitudinally in an ideal hydrodynamic context, seems to miss out on many recent advancements of the theories that govern heavy ion collisions. Our claim, however, is that the se-

ries of approximations made by CUJET does not invalidate at all the results obtained by the model, assuming that such systematic errors are negligible in the specific context of our predictions.

In [225], initial state fluctuations are seen to affect only higher harmonics of the particle azimuthal flow distribution, while viscosity effects in central collisions can be accounted for by a rescaling of the coupling constant α_s or its saturation value α_0. In other words, when looking at angle-integrated observables in central events, the Bjorken ideal 1D+1 hydrodynamic evolution is a good enough approximation.

The inclusion of more complex geometries and more accurate plasma evolutions is readily obtainable in CUJET. Since the algorithm pre-evaluates the QGP density in a separate subroutine and tables it to improve the speed of the Monte Carlo integration, virtually any external hydrodynamical code could be coupled to CUJET in order to provide the necessary input.

5.2 Jet propagation

When two heavy nuclei collide, few hard events lead to the creation of highly energetic partons with momenta of several GeV. The spatial distribution of these jets is proportional, according to the Glauber model, to the distribution of nucleon-nucleon collisions in the plasma (cf. Eq. 5.8). The distribution of momenta, instead, is given by pQCD computations and is

measured in p+p events.

The study of the quark gluon plasma via hard jet quenching relies in large part on the comparison between A+A and p+p results, often assuming that cold nuclear matter effects play a minor role in the suppression of jets. Observed pion p+p spectra, for instance, provide the baseline for the comparison, but quenching in the plasma happens at the partonic level, and the partonic spectra are needed to make any kind of prediction. The factorization of scales in hard processes permits the isolation of the partonic spectra, which otherwise cannot be directly measured experimentally. Only after being convoluted with the appropriate fragmentation function, the spectra can be compared to p+p data.

We are going to identify three distinct phases in the propagation of jets in the quark-gluon plasma: (1) formation of jets ($\tau = 0$); (2) parton quenching while the medium thermalizes and expands longitudinally ($0 < \tau \leq \tau_f$); (3) fragmentation of jets into hadrons ($\tau = \tau_f$). In this Section we will explain how CUJET computes each of these processes.

5.2.1 Partonic spectra

For the light jet sector, production is based on a leading order (LO) calculation scaled by a simple K-factor and computed from the LO pQCD CTEQ5 code of X.N. Wang [226].

For the heavy jet sector, both next-to-leading order [227] and fixed-order plus next-to-leading-log (FONLL) [228, 229] computations are used. In addi-

tion to including the full NLO result [230, 231, 232], the FONLL calculation resumms large perturbative terms with next-to-leading logarithmic accuracy [233]. We report results for both NLO and FONLL initial cross sections to estimate the error band associated with this source of systematic uncertainty. Numerical computations of the spectra are provided by R. Vogt as in [234]. In Fig. 5.7, we show the initial partonic production spectra at RHIC and LHC energies.

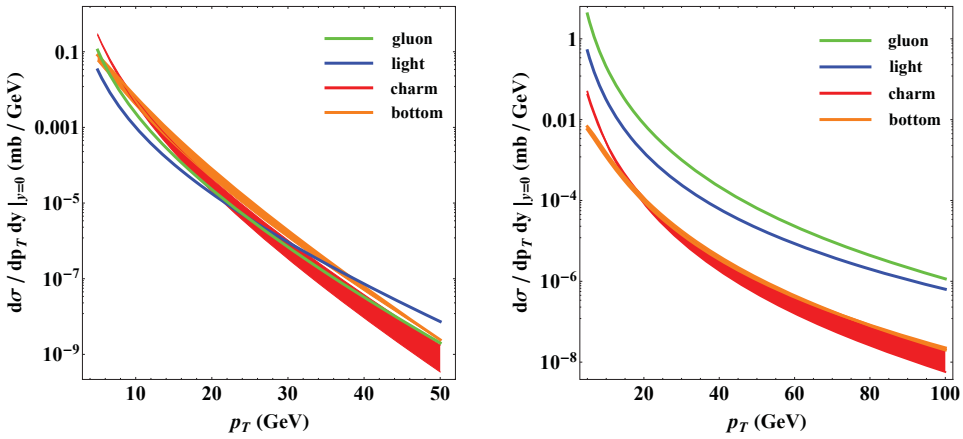

Figure 5.7: pQCD p+p production spectra at $\sqrt{s_{NN}} = 200$ GeV (RHIC, *left*) and $\sqrt{s_{NN}} = 2.76$ TeV (LHC *right*). Notice how steeper the RHIC spectra are compared to LHC ones.

Depending on what physical observables we are interested to compute, different features of the partonic spectra may or may not assume a relevant role. Let's consider, for instance, the nuclear modification factor R_{AA}. Since R_{AA} is defined as a ratio of particles yields (cf. Section 5.3 for the rigorous definition), the absolute value of the cross section matters little and the normalization drops out in the very same definition of the observable. What

affects the computation is rather the slope of the cross section, and eventually the relative normalization between different flavors.

An insightful example comes from the pion yield in p+p events at LHC, Fig. 5.8, which is computed by convoluting the production spectra of quarks and gluons with the appropriate fragmentation functions (more details in Section 5.2.3).

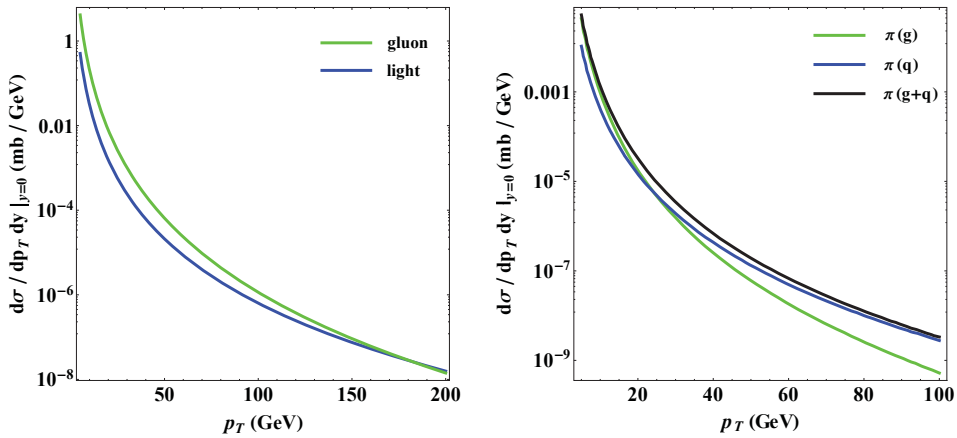

Figure 5.8: *left* p+p gluon and light quark production spectra, same as Fig. 5.7 *right* p+p pion spectra from gluon only contribution (green), quark only contribution (blue), and total gluon plus quark contribution (black), assuming no 'cold' nuclear effects. The pion spectra are computed using KKP fragmentation functions.

We can make two observations:

- Since gluons and light quark contributions are summed together to get the pion yield, the relative normalization between the two matters. The absolute normalization, on the other hand, drops out once the nuclear

modification factor ratio is taken.

- Despite the high production of gluons at low $p_\perp$, the gluon distribution is much steeper than the quark one. As a consequence, once fragmentation is taken into account, the gluonic contribution to the total number of pions produced sinks below the quarkonic one already at $p_\perp \gtrsim 25$ GeV. It is then reasonable to expect R_{AA} to depend on the light quark sector only for sufficiently high momenta.

Another example where only the relative steepness between two production spectra matters is given by the comparison between the (unphysical) partonic yields of light and charm quarks. In Chapter 3 we saw that light and charm quarks approximately lose the same amount of energy when they propagate through a deconfined medium, however the production spectrum of charm quarks is much steeper than the one of light quarks (cf. Fig. 5.7). The immediate consequence is that the partonic yield for charm quark is suppressed compared to the other, regardless of the separate normalization of the production spectra.

A similar effect applies when we compare RHIC (steeper) and LHC (flatter) spectra: the expected induced energy loss increase at LHC with respect to RHIC due to higher densities and temperatures, which itself would drive the particle yields down, is going to be partly compensated by the flatter production cross-sections, which in turn drive the yields up.

CUJET computes the quenched partonic spectra convoluting the production cross section with the energy loss probability distribution $P(\epsilon)$, Eq. (4.16). This is a critical improvement of CUJET over its predecessor WHDG, which assumes instead a simple and slowly varying power law distribution for the p+p spectra (spectral index approximation) and makes considerable simplifications in the computation of the nuclear modification factor. Given the sensitivity of the results to the details of the production cross sections, and the complex interplay between the latter and the energy loss mechanism, it is essential that no approximations are carried out in this delicate step of the computation.

This is how CUJET performs the computation the quenched partonic spectra:

- The algorithm starts from a parton created at $\mathbf{x}_0$ with initial direction ϕ and mass M. The transverse space distribution of jets is given by ρ_{binary}. The initial transverse momentum probability distribution $P_0(p_i)$ of the partons is proportional to the production cross section:

$$P_0(p_i) \equiv \frac{d\bar{\sigma}^{pp}}{dp_i}(p_i) = \frac{1}{\mathcal{N}} \frac{d\sigma^{pp}}{dp_i}(p_i) \quad , \tag{5.23}$$

with

$$\int_{p_i^{MIN}}^{p_i^{MAX}} dp_i \; P_0(p_i) = 1 \quad . \tag{5.24}$$

Here $d\sigma^{pp}/dp_i$ represents a generic p+p partonic production spectrum. A range of discrete momenta $[p_i^{MIN}, p_i^{MAX}]$ needs to be defined for the

numerical computation.

- For each initial momentum p_i in the range $[p_i^{MIN}, p_i^{MAX}]$, CUJET computes the energy loss according to Eq. (4.24) or (4.25). This is the most resource- and time-consuming process, where the full jet path Monte Carlo integral is evaluated over the expanding plasma and the medium-induced gluon radiation spectrum is computed. The user can specify all the dynamical properties of the plasma and which contributions to the energy loss – radiative and/or elastic – should be considered. Once fluctuations effects are taken into account – Eq. (4.16),(3.20),(4.15) – the output takes the form of a distribution function which represents the probability of losing the relative energy ϵ given the initial momentum p_i:

$$P(\epsilon; p_i) = P_0(p_i)\delta(\epsilon) + \tilde{P}(\epsilon; p_i)|_0^{\epsilon_{MAX}} + P_1(p_i)\delta(\epsilon - \epsilon_{MAX}) \ , \quad (5.25)$$

with

$$\epsilon_{MAX} = 1 - \frac{M}{\sqrt{p_i^2 + M^2}} \ . \quad (5.26)$$

- Once all the $\{p_i\}$ in the range specified have been computed, the $\{P(\epsilon; p_i)\}$ are converted into a two-dimensional distribution map that represents the probability of a jet with initial momentum p_i to leave

the plasma with final momentum p_f:

$$P(p_f, p_i) = P(\epsilon; p_i)\frac{d\epsilon}{dp_f}$$
$$= P_0(p_i)\delta(p_f - p_i) + \tilde{P}(\epsilon(p_f, p_i); p_i)\frac{p_f}{E_f E_i} - P_1(p_i)\delta(p_f) \ , \tag{5.27}$$

with

$$\epsilon(p_f, p_i) = 1 - \frac{E_f}{E_i} \ , \quad E_f = \sqrt{p_f^2 + M^2} \ , \quad E_i = \sqrt{p_i^2 + M^2} \ . \tag{5.28}$$

The normalization is such that

$$\int_0^{p_i^{MAX}} dp_f \ P(p_f, p_i) = 1 \ . \tag{5.29}$$

In Eq. (5.27) we omitted the explicit dependence on the jet parameters $\mathbf{x}_0$ and ϕ.

- CUJET, then, integrates over the normalized production spectrum, Eq. (5.23), to obtain the distribution of final transverse momenta:

$$P(p_f; \mathbf{x}_0, \phi) = \int_{p_i^{MIN}}^{p_i^{MAX}} dp_i \ P(p_f, p_i; \mathbf{x}_0, \phi)\frac{d\bar{\sigma}^{pp}}{dp_i}(p_i) \ . \tag{5.30}$$

Obviously,

$$\int_0^{p_i^{MAX}} dp_f \ P(p_f; \mathbf{x}_0, \phi) = 1 \ . \tag{5.31}$$

- At last, the A+A quenched partonic spectra as a function of the observed momentum p_f and azimuthal angle ϕ are obtained by integrating over the jet transverse distribution :

$$\frac{d\sigma^{AA}}{dp_f d\phi} = \int d\mathbf{x}_0 \, \overline{\rho}_{binary}(\mathbf{x}_0) \, \mathcal{N} \, P(p_f; \mathbf{x}_0, \phi) \quad . \tag{5.32}$$

$\mathcal{N}$ is given by Eq. (5.23).

5.2.2 Jet quenching parameters

It should be clear, at this point, what the input and output of CUJET are: the algorithm is given a parametrization of the plasma and a jet spectrum, and it returns a quenched spectrum after computing the energy loss of the partons in the medium. Each jet is evolved individually in this process no approximations are made.

Here we present a comprehensive list of all the parameters that enter the computations.

Plasma formation and evolution

A table of the transverse QGP density at mid-rapidity, generated by an independent subroutine, is generated. For the current computations, we use a Glauber plasma profile (Eq. (5.3)), which undergoes longitudinal Bjorken expansion (Eq. (5.18)). These approximations hold fine when looking at symmetrical angle-integrated observables such as the nuclear modification

factor in central collisions. In addition to the parameters shown in Table 5.1, we have:

parameter	description	default value
b	impact parameter	0
$\frac{dN}{dy}$	initial rapidity density	1000 (RHIC), 2200 (LHC)
n_f	quark flavors	0
$f(\frac{\tau}{\tau_0})$	thermalization process	linear
τ_0	formation time	1 fm/c
T_f	fragmentation temperature	≈ 100 MeV

Jet creation and quenching

Jets are created at $\tau = 0$ and are distributed according to ρ_{binary} (Eq. (5.8)). Each jet is tagged with an initial location $\mathbf{x}_0$ and direction ϕ. The momentum distributions, i.e. production spectra, are plotted in Section 5.2.1. CUJET evolves each jet in the plasma individually and computes the energy loss. The input parameters are:

parameter	description	default value
$\mathbf{x}_0$	jet creation point	according to ρ_{binary}
ϕ	jet direction	uniformly distributed $[0, 2\pi]$
M	parton mass	0 (gluon), 0.2 (l), 1.2 (c), 4.75 (b) GeV
$p_\perp$	initial momentum	according to production spectra

Additional parameters specific of the jet-medium interaction model are:

parameter	description	default value
n	opacity expansion order	1
$r_m \equiv \frac{\mu_m}{\mu_e}$	ratio of screening masses	0 (pure dynamical model)
α_s	coupling constant (if fixed)	0.3
α_0	saturated coupling (if running)	0.4

We consider the effective coupling constant α_s – if the coupling is fixed – or the saturated value α_0 – if the coupling is running – as the single free parameter in CUJET.

5.2.3 Jet fragmentation

Partonic spectra provide additional insight on the jet quenching mechanism, nevertheless comparison with data can only be done at the hadronic level. The quenched spectra, Eq. (5.32), need to be convoluted with a set of fragmentation functions (FFs).

The process that leads to the fragmentation of partons in the medium is not theoretically well understood, especially for heavy quarks: dissociation and recombination theories [235, 236] assume that heavy D and B mesons can be formed within the plasma and lose additional energy through collisional dissociation, in a similar fashion to what has been suggested for heavy quarkonium states [237]. This, however, seems to contradict more recent lattice results [149], which indicate the complete melting of open heavy flavors at temperatures $T \gtrsim 220$ MeV.

Since we are dealing with high $p_\perp$ partons, hadronization via recombination processes is suppressed compared to fragmentation (cf. Chapter 1). We will assume that fragmentation takes place in vacuum, on a hypersurface parametrized by $\mu(\mathbf{x}, \tau_f) = \Lambda_{QCD}$. Results do not show a particular sensitivity on the precise choice of T_f, as shown in the next Section.

The convolution of the partonic spectrum with the appropriate FF takes the form

$$\begin{aligned} \frac{d\sigma^h}{dp}(p) &= \sum_i \int_{p/p_{MAX}}^1 dy \; \frac{d\sigma^i}{dp}(\frac{p}{y}) \; D^{i\to h}(y; \frac{p}{y}) \\ &= \int_{p/p_{MAX}}^1 dy \; \frac{1}{y} \frac{d\sigma^i}{d\frac{p}{y}}(\frac{p}{y}) \; D^{q_i\to h}(y; \frac{p}{y}) \quad . \end{aligned} \tag{5.33}$$

We remind that $D^{i\to h}(y; Q)$ represents the probability that a parton i fragments into a hadron h which carries a fraction y of the parton energy. Q is the scale at which the FF is evaluated, here given by the energy of the parton. Eq. (5.33) is summed over all species i that fragment into h.

For light quarks and gluons fragmenting into pions, we use leading order KKP functions [238].

For heavy quarks fragmenting into D and B mesons ($c \to D$ and $b \to B$), we use instead the Peterson [239] function with $\epsilon_c = 0.06$ and $\epsilon_b = 0.006$, as done also in [240]. While the Peterson FF does not couple well with the FONLL production cross section [234], it was shown in [240] that similar results are produced anyways even using a more accurate fragmentation

description. Finally for the decay of the heavy mesons into non-photonic electrons ($c \to D \to e$ and $b \to B \to e$), we use the same functions as in [234]. The secondary decay $D \to B \to e$ is also accounted for, even though the contribution to the total yield is negligible.

5.3 Systematic analysis of CUJET

The nuclear modification factor, R_{AA}, is defined as the ratio of the quenched A+A spectrum to the unquenched p+p spectrum, scaled according to the number of binary collisions N_{binary}:

$$R_{AA}(p_\perp) = \frac{\dfrac{d\sigma^{AA}}{dp_\perp}(p_\perp)}{N_{binary}\,\dfrac{d\sigma^{pp}}{dp_\perp}(p_\perp)} \quad . \tag{5.34}$$

Assuming the absence of both 'cold' and 'hot' nuclear matter effects, i.e. assuming the partons are unaffected by the presence of the deconfined medium, the nuclear modification factor is expected to be equal to unity, at least for sufficiently high $p_\perp$. If jet quenching processes occur, instead, R_{AA} drops below unity due to the medium-induced suppression of the A+A spectrum. As a rule of thumb, larger energy loss and steeper production spectra lead to a stronger suppression of R_{AA}, whereas smaller energy loss and flatter spectra lead to a weaker suppression.

More details on R_{AA} will be given in the next Chapter, where we will

present a comprehensive experimental picture of the quark gluon plasma based on the observation of the nuclear modification factor.

In this Section we are going to use R_{AA} as a tool to test the CUJET model and quantify the theoretical systematic uncertainties that affect our predictions.

As the first example, we plot in Fig. 5.9 the p+p (unquenched) and A+A (quenched) partonic spectra of gluons and light quarks, along with the pion multiplicity derived from the fragmentation of the gluons and the quarks. The resulting nuclear modification factor is shown in the right panel of the figure for all three species.

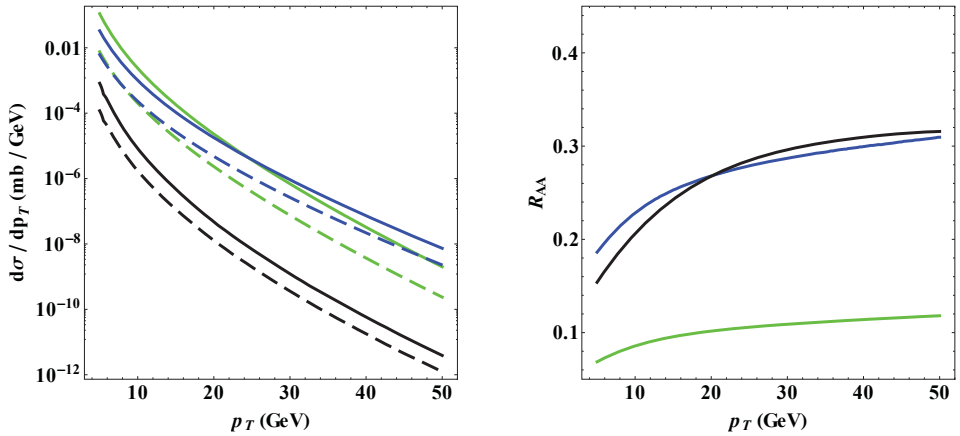

Figure 5.9: *left* unquenched (solid) and quenched (dashed) spectra for gluons (green), light quarks (blue) and pions (black). Default parameters are used, as shown in Sec. 5.2.2. The initial rapidity density is constrained by RHIC measurements ($dNdy = 1000$). Radiative contributions to the energy loss are computed in the pure HTL framework (dynamical model), and the coupling constant is assumed fixed at the effective value $\alpha_s = 0.3$. Fragmentation is taken according to the KKP fragmentation scheme as explained in Sec. 5.2.3. *right* R_{AA} is computed using the spectra shown on the left. R_{AA}^{gluon} is much suppressed with respect to R_{AA}^{quark} due to the enhanced energy loss, proportional to the Casimir ratio $C_A/C_F = 9/4$.

The $p_\perp$ dependence of R_{AA} is a result of the competing effects between the energy dependence of the energy loss ($\Delta E/E \sim E^{1/3}$ for fixed coupling) and the $p_\perp$ dependence of the partonic cross section. Notice the surprising similarity between R_{AA}^{pion} and R_{AA}^{quark} as if the gluons didn't contribute at all. This effect is due to a complex interplay between the gluon spectra and the fragmentation function which further suppresses the gluonic yield for sufficiently high $p_\perp$.

5.3.1 Plasma parameters

In this paragraph we analyze the sensitivity of CUJET to the parameters that govern the evolution of the medium: the number of quarkonic flavors, the formation time and thermalization scheme, the fragmentation temperature, and the initial rapidity density. Depending on our choice of fixed or running coupling constant, we consider α_s or α_0 the free parameters of the model.

In Fig. 5.10 we change the value of n_f from 0 (pure gluonic matter), to 2.5 (mix of gluonic and quarkonic degrees of freedom in chemical equilibrium). We can easily observe that a simple rescaling of α_s of approximately 6% leads to a perfect agreement between the two scenarios. In [218], Zakharov reaches a similar conclusion starting from a path integral approach to the energy loss and using a strong running coupling. This simple analysis demonstrates the substantial insensitivity of our model to the detailed composition of the quark gluon plasma.

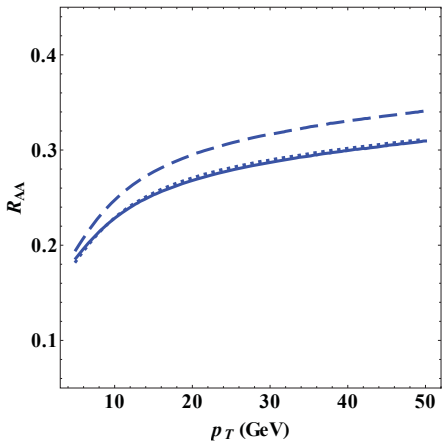

Figure 5.10: Light quark R_{AA}, with $n_f = 0$ and $\alpha_s = 0.3$ (solid line), $n_f = 2.5$ and $\alpha_s = 0.3$ (dashed line), $n_f = 2.5$ and $\alpha_s = 0.32$ (dotted line). The pure gluonic scenario and the equilibrated quark gluon plasma scenario with a 6% increase of the coupling are indistinguishable.

The next step is to study the sensitivity to the thermalization phase of the plasma. In Sec. 5.1.2 we hinted to the complexity of the problem, and approximated the initial evolution of the QGP with three analytic models: linear, divergent and free streaming. After thermalization is reached at $\tau_0 = 1$ fm/c, the plasma expands as $1/\tau$. The results in Fig. 5.11 indicate a great sensitivity to the pre-thermalization phase of the evolution, which can be counter-balanced by an adequate rescaling of the coupling constant.

If we constrain α_s to fit a specific $p_\perp$ point of pion R_{AA} at RHIC initial conditions, *left*, we observe a complete overlap – or "degeneracy" – among the linear, divergent and free streaming scenarios. The constrained fit extrapolated to LHC energies, *right*, shows on the other hand a moderate "splitting"

at high $p_\perp$ among the same curves. Although the difference is too small to be measured experimentally, at least in theory this effect could be studied to discriminate among pre-thermalization phenomenological models.

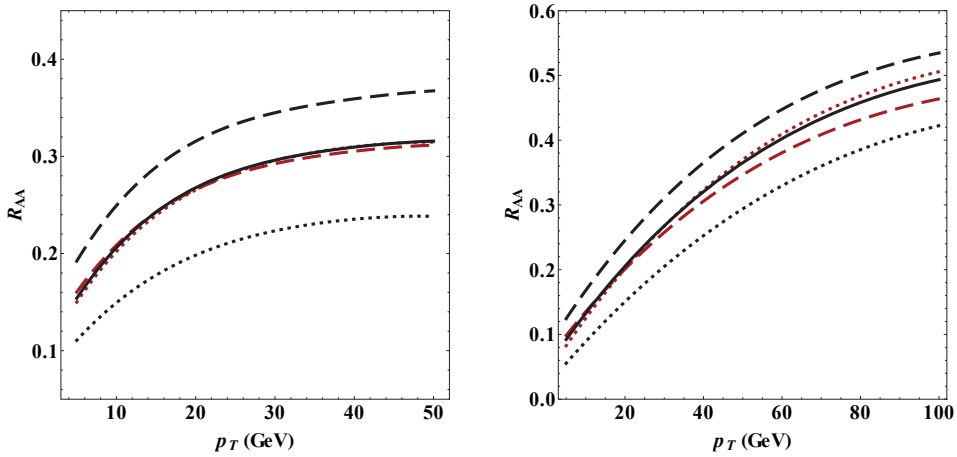

Figure 5.11: Pion R_{AA} for three distinct plasma thermalization scenarios, with and without rescaling of the coupling constant: linear with $\alpha_s = 0.3$ (solid black); divergent with $\alpha_s = 0.3$ (dotted black) or $\alpha_s = 0.27$ (dotted red); free streaming with $\alpha_s = 0.3$ (dashed black) or $\alpha_s = 0.32$ (dashed red). The coupling constant is rescaled to fit $R_{AA}^{\pi,RHIC}(p_\perp = 10 \text{ GeV}) = 0.2$ (*left*), and the constrained extrapolation to LHC is shown on the *right*.

The same effect is visible in Fig. 5.12, where pions, D and B meson R_{AA} is plotted assuming RHIC (*left*) and LHC (*right*) initial conditions. The curves are constrained by the same RHIC fit of Fig. 5.11-*left*. In particular, we observe a moderate "splitting" of B meson R_{AA} across all $p_\perp$, which is a signature of the differences between the light and heavy quark quenching mechanism during the early evolution of the plasma (cf. Fig. 5.5).

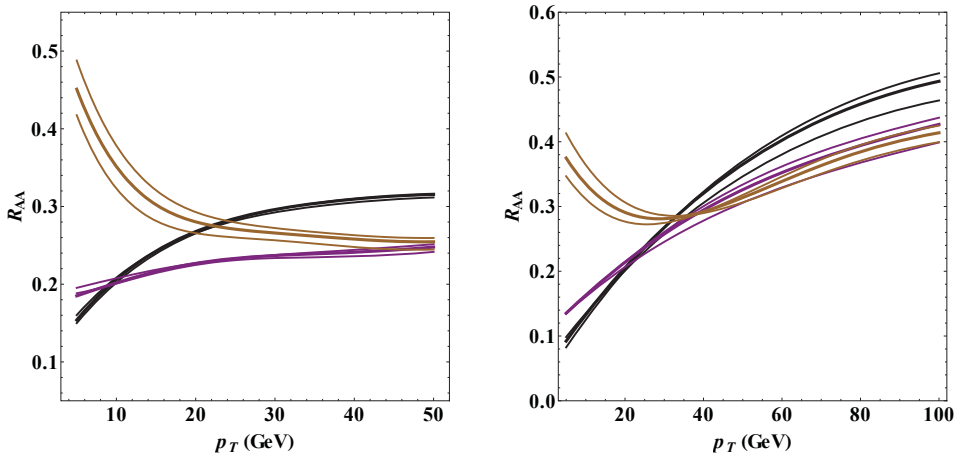

Figure 5.12: Flavor R_{AA} at RHIC (*left*) and LHC (*right*). In black the pions, in purple the D mesons, in brown the B mesons. Thick lines correspond to the linear thermalization model with $\alpha_s = 0.3$, thin lines represent both the divergent and free streaming models with $\alpha_s = 0.27, 0.32$ respectively.

We now focus the attention to the late phase of plasma evolution and measure the sensitivity of R_{AA} to the jet hadronization temperature T_f. In Fig. 5.13, the partonic nuclear modification factor is shown for light and heavy quarks, for the default $T_f = 100$ MeV and $\alpha_s = 0.3$ parameters, $T_f = 50$ MeV and $\alpha_s = 0.3$, and finally $T_f = 200$ MeV and α_s rescaled to 0.35. We observe that jet quenching is "saturated" already at $T_f = 100$ MeV: even if we let the jets interact until T drops to the (unphysical) value of 50 MeV, no significant changes occur in R_{AA}. On the contrary, restricting the interaction region to $T > 200$ MeV alters significantly the results and a moderate $\sim 20\%$ rescaling of the coupling constant is needed in order to reproduce the the original curve. However, given the freedom to fit the α_s parameter, our model is again insensitive to this source of theoretical

uncertainty.

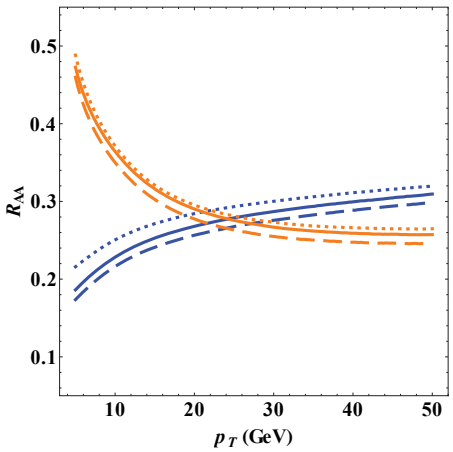

Figure 5.13: Light (blue) and heavy (orange) quark partonic R_{AA} at RHIC energy, assuming $T_f = 100$ MeV and $\alpha_s = 0.3$ (solid), $T_f = 50$ MeV and $\alpha_s = 0.3$ (dashed), $T_f = 200$ MeV and $\alpha_s = 0.35$ (dotted).

Finally, we study the sensitivity of R_{AA} to the initial rapidity density dN_g/dy. This parameter, constrained by experimental observations, fixes the initial density and temperature of the plasma according to Eq. (5.18). Intuitively, we expect the quenching to be higher for denser plasma, resulting in an increased suppression of R_{AA} for collisions observed at the LHC. Our expectations are confirmed in Fig. 5.14.

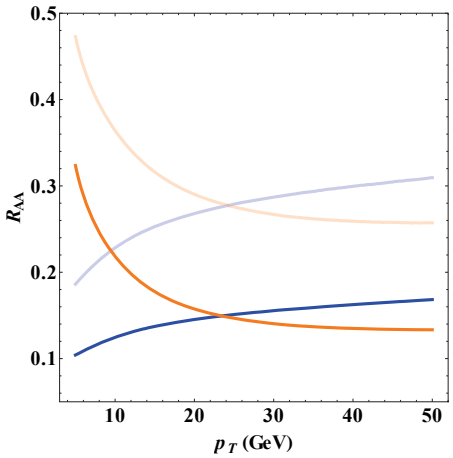

Figure 5.14: R_{AA} for light (blue) and heavy (orange) quarks. RHIC production spectra are used in this plot, as well as RHIC collision parameters (Au+Au nuclei). However, the initial observed rapidity density is increased from 1000 (RHIC, opaque lines) to 2200 (LHC, solid lines). The increased quenching is responsible for the suppression of R_{AA}.

5.3.2 Spectrum variations

In this paragraph we are going to study the systematic uncertainties related to the choice of initial production spectra.

Let's take the previous example where we increased the density dN_g/dy from RHIC to LHC conditions, and change the production spectra accordingly, from RHIC to LHC as in Fig. 5.7-*right*. The impact on R_{AA} is large, and two separate effects can be noticed: (1) softer LHC spectra cause a vertical lift in R_{AA} that completely counters the suppression generated by the increased density; (2) pion R_{AA} rises faster with $p_\perp$, again due to the particular shape of the light quark spectra at LHC.

Once again, the complex interplay between energy loss and initial partonic spectra leads to non-trivial results out of reach with simple analytical approximations.

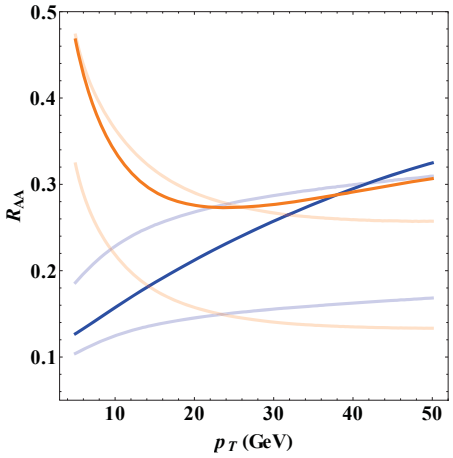

Figure 5.15: LHC production spectra are used in conjunction with $dN_g/dy = 2200$ to show the sensitivity of R_{AA} to the steepness of the p+p partonic cross sections. As usual, we present results for light (blue) and heavy (orange) quarks. The solid curves are superimposed to the plot of Fig. 5.14 (opaque curves), where either RHIC initial conditions or a mix of RHIC (spectra) and LHC (density) initial conditions are used.

The uncertainties that arise from the choice of NLO or FONLL schemes for heavy quark initial spectra are shown in Fig. 5.16. The error bands shown in the Figure are relatively small. At the partonic level, in fact, any uncertainty in the normalization of the production spectra is factored out: R_{AA} is only sensitive to changes in the slope.

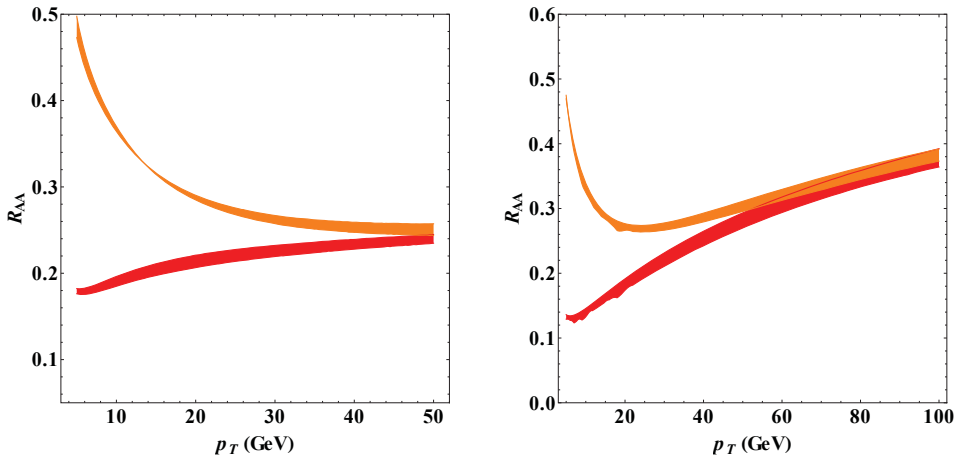

Figure 5.16: Charm (red) and bottom (orange) partonic R_{AA}, at RHIC (*left*) and LHC (*right*). Only the uncertainty in the slope of the spectra matters, since the uncertainty in the absolute normalization is canceled when the R_{AA} ratio is taken.

5.3.3 Running coupling

In this final paragraph, we study the systematic uncertainties related to the choice of running coupling.

According to Fig. 4.9, the running coupling drastically alters the jet energy dependence of the energy loss, making $\Delta E/E$ approximately independent of E. This naively implies smaller quenching at high energies and an increase in the R_{AA} slope. Fig. 5.17 proves our assertions. Remarkable is the fact that the change in the slope of R_{AA} cannot be mimic by a rescaling of the fixed coupling α_s: this measurement constitutes a potentially clear signature of running coupling effects.

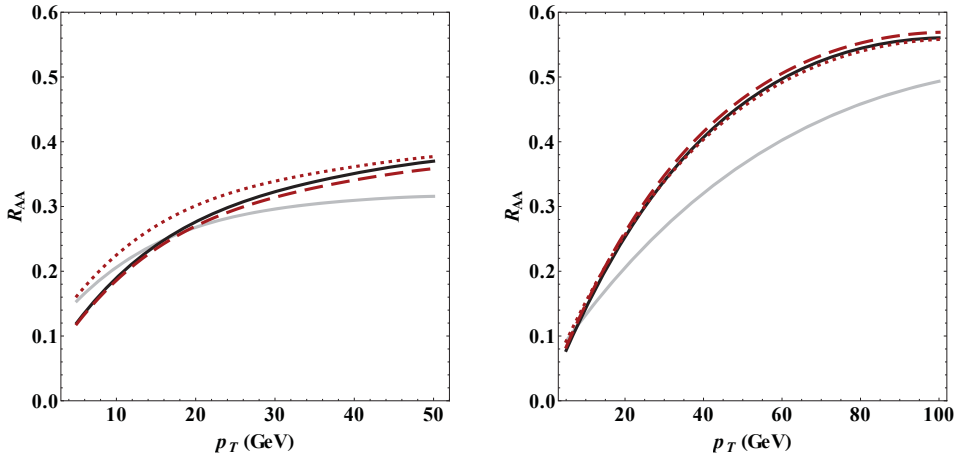

Figure 5.17: Fixed and running coupling pion R_{AA} results are compared side to side at RHIC (*left*) and LHC (*right*). The gray opaque curves use a fixed $\alpha_s = 0.3$, while the black curves use a running coupling with $\alpha_0 = 0.4$. The difference is notable, especially in the higher energy range available at the LHC, while RHIC results are left almost unchanged. The sensitivity to the variation of running scales Q (cf. Eq. (4.27) and following) is measured by the red curves: on one side we decrease the value of all scales Q by 50% and lower α_0 to 0.3 (red dashed), on the other we increase all scales Q by 25% and increase at the same time α_0 to 0.6 (red dotted). α_0 is constrained to fit $R_{AA}^{\pi,LHC}(p_\perp \approx 30 \text{ GeV}) = 0.35$.

As pointed out in Sec. 4.4, the choice of running scale Q^2 is subject to a certain degree of arbitrariness. To study the effects of this source of systematic uncertainty on jet tomography, we increase or decrease the running scale Q by 25 and 50 percent respectively, and compensate the change by a rescaling of the free parameter α_0. The results, shown in the same Fig. 5.17, demonstrate the substantial insensitivity of CUJET to the choice of running scales.

5.4 Conclusions

In this Chapter we presented the CUJET model and its application to the computation of the nuclear modification factor. The first two Sections were dedicated to the modeling of the quark gluon plasma and the analysis of the propagation of the jet through the medium. The third and last Section was fully devoted to the study of the theoretical systematic uncertainties that affect our results.

We concluded that CUJET is a reliable model capable of making accurate experimental predictions. The freedom to fit one single parameter (α_s or α_0) to the data guarantees that the results are insensitive to most of the known theoretical systematic uncertainties.

The robustness of CUJET, then, derives from the possibility of making constrained predictions that span a wide range of physical observables (plasma density, jet flavor, collision energy, centrality and angular dependence).

Chapter 6

Flavor tomography

The discovery of the suppression of high $p_\perp$ hadrons made at RHIC in Au+Au collisions at $\sqrt{s_{NN}} = 130$ GeV [241, 242] and $\sqrt{s_{NN}} = 200$ GeV [14, 243, 244], as opposed to what observed at the SPS [245], was readily interpreted as a possible signature of the formation of quark gluon plasma for sufficiently high collision energies [113, 114, 115, 11], and opened up the possibility to study the nature of the plasma through the tomographic analysis of highly energetic jets [246, 247].

6.1 Nuclear modification factor

The idea is simple: the production of hard jets in heavy ion collisions scales with the number of binary collisions N_{binary}, Eq. (5.8). In the absence of any effect induced by the presence of nuclear matter, one should expect

the spectrum of the observed hadrons produced in the collision to be proportional to the spectrum observed in an equivalent proton+proton (p+p) event, with proportionality constant given by N_{binary}. In other words, the nucleus+nucleus (A+A) collision can be interpreted as an incoherent superposition of elementary p+p interactions. The hard collisions that lead to the creation of high $p_\perp$ jets, in fact, are well localized and interference effects expected to be negligible. In this scenario, the nuclear modification factor R_{AA}, which itself scales with N_{binary}, is equal to unity by definition.

In the presence of effects induced by the existence of either 'cold' or 'hot' nuclear matter, the multiplicity of the produced hadrons will be immediately affected, leading to the suppression, or enhancement depending on the dominant effect, of the nuclear modification factor. R_{AA}, therefore, becomes an invaluable yet simple tool used to probe the nature of the quark gluon plasma and to validate our understanding of the dense nuclear matter and jet-medium interaction mechanism.

So far we have only mentioned high $p_\perp$ particles. On the contrary, low $p_\perp$ particles are produced in soft processes characterized by large values of the coupling constant, and non-perturbative QCD effects become dominant. In this context, the wounded nucleon model [248] postulates that the multiplicity of the soft particles scales with the number of participating nucleon pairs, or $1/2N_{part}$, Eq. (5.3). Given $N_{part} < N_{binary}$, it follows that at low $p_\perp$ the nuclear modification factor is smaller than unity, even in the absence of nuclear matter effects.

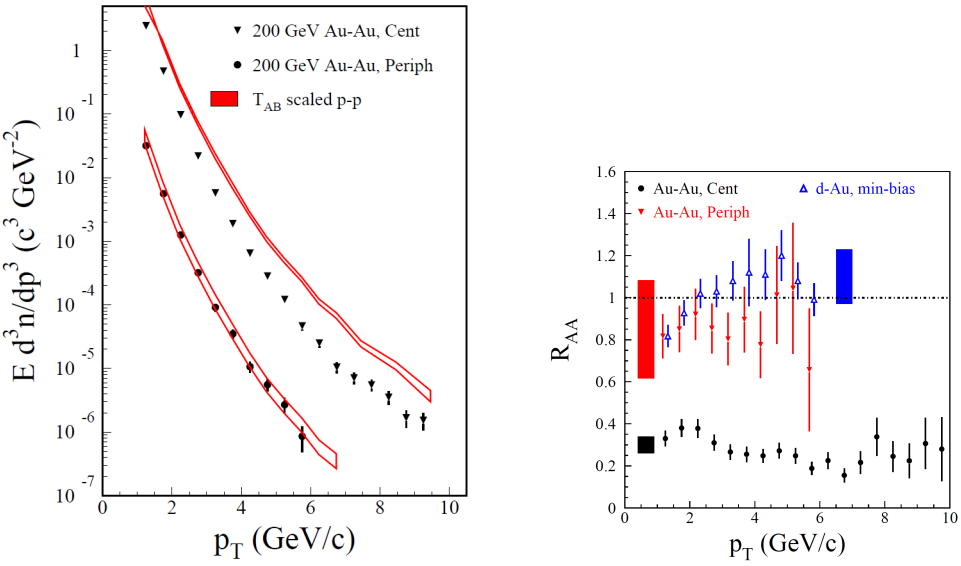

Figure 6.1: *left* Transverse momentum spectra of π^0 measured in 200 GeV Au+Au central and peripheral collisions [11]. Solid curves indicate π^0 spectra measured in 200 GeV p+p collisions [12], scaled by N_{binary}. *right* The nuclear modification factor clearly shows π_0 yield suppression [11], interpreted as a signature of dense QGP formation in central collisions. Peripheral events do not lead to suppression due to the thinner size and smaller density of the plasma.

It then becomes clear that there are three regimes we need to take into consideration, identified by the transverse momentum of the particles produced in the collision:

- low $p_\perp \lesssim 2$ GeV particles, produced in nonperturbative soft processes;
- high $p_\perp \gtrsim 5$ GeV particles, produced in perturbative hard processes;
- an intermediate region, consisting of particles with momenta $2 \sim 5$

GeV, where a mix of soft and hard processes take place.

Our chances to apply the principles of tomography to the study of the quark gluon plasma rely on the correct understanding and theoretical control over the nuclear effects that dominate each of these different regions. In order to shed light on the properties of the dense matter created in the early stages of heavy ion collisions, we need to be able to disentangle those effects ascribable to parton-plasma interactions (namely parton energy loss or jet quenching) and those instead attributable to phenomena that precede the formation of the hot medium (so-called initial 'cold' state effects, cf. Sec. 1.3).

The increased particle multiplicity observed at moderately high $p_\perp$, for instance, which manifests itself with a sudden rise of R_{AA} above unity in the energy range $1 \lesssim p_\perp \lesssim 7$ GeV [249, 250], is explained by the presence of the Cronin effect [161]. Multiple parton scatterings that happen prior to the hard scattering process broaden the transverse momentum distribution of the partons inside the nucleus, causing in turn an enhancement of the final $p_\perp$ distribution of the observed hadrons. Competing with this increase, however, are the interference effects among successive scatterings, that suppress the particle multiplicity gains at very low and high $p_\perp$: the net enhancement of particle spectra due to multiple scatterings decreases as $1/p_\perp^2$ and vanishes for sufficiently high $p_\perp$.

The Cronin effect shows us the importance of isolating all those effects that are not directly attributable to final state interactions, and therefore

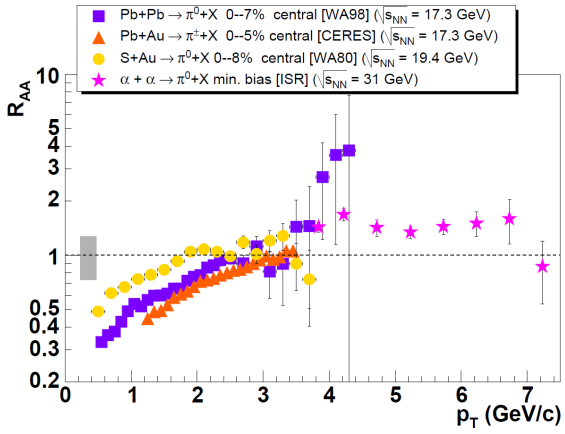

Figure 6.2: Nuclear modification factor for π^0 production in A+A collisions at different center-of-mass energies. Both Cronin effect and binary scaling are visible. Taken from [11].

useful to probe the properties of the hot plasma. Crucial to this purpose is the measurement of R_{AA} in deuteron+nucleus (d+A) collisions, otherwise called control experiments. If p+p collisions provide the baseline, or reference spectrum, for the computation of R_{AA}, p+A and d+A experiments ensure our correct understanding of cold nuclear effects, or at least indicate their impact on A+A measurements.

At RHIC, such control experiments [244, 251, 252] have confirmed the negligible effect that initial state interactions have on the production of high $p_\perp$ particles, and have substantiated our understanding of the suppression of R_{AA} in terms of induced radiative processes [246, 247].

Early predictions of $p_\perp > 2$ GeV pion R_{AA} [13] show the interplay of initial (shadowing and Cronin) and final (parton energy loss) state nuclear

effects in d+Au and Au+Au reactions at $\sqrt{s_{NN}} = 17, 200, 5500$ GeV (SPS, RHIC and LHC respectively). The hierarchy of the three competing effects is clear (see Fig. 6.3): at SPS the spectra are dominated by Cronin enhancement, resulting in an increased multiplicity with respect to the p+p reference and substantially confirming what already observed in [245]. At RHIC, the combination of the three effects leads to an approximately constant suppression pattern of π^0 in the range $2 < p_\perp < 20$ GeV, with the parton energy loss becoming the dominant effect for $p_\perp \gtrsim 8$ GeV. On the contrary, at LHC shadowing and Cronin effects are found to be almost negligible, and R_{AA} shows a rapid growth driven only by jet quenching.

Once again, the importance of measuring the high end of the transverse momentum spectrum is remarked: only in this region, in fact, we can isolate the contribution to the nuclear modification factor arising from parton energy loss and apply perturbative QCD techniques to the computation of jet-medium interactions. Furthermore, given the systematic large uncertainties that affect both predictions and data, only the $p_\perp$ dependence of R_{AA} measured over a sufficiently large momentum range is sometimes useful to discriminate among different theoretical models and constraint any calculation of jet energy loss. There is also another more subtle reason to favor high $p_\perp$ measurements: the exclusion of radiative gluon fragmentation contribution from pion production at low and moderate transverse momenta [253].

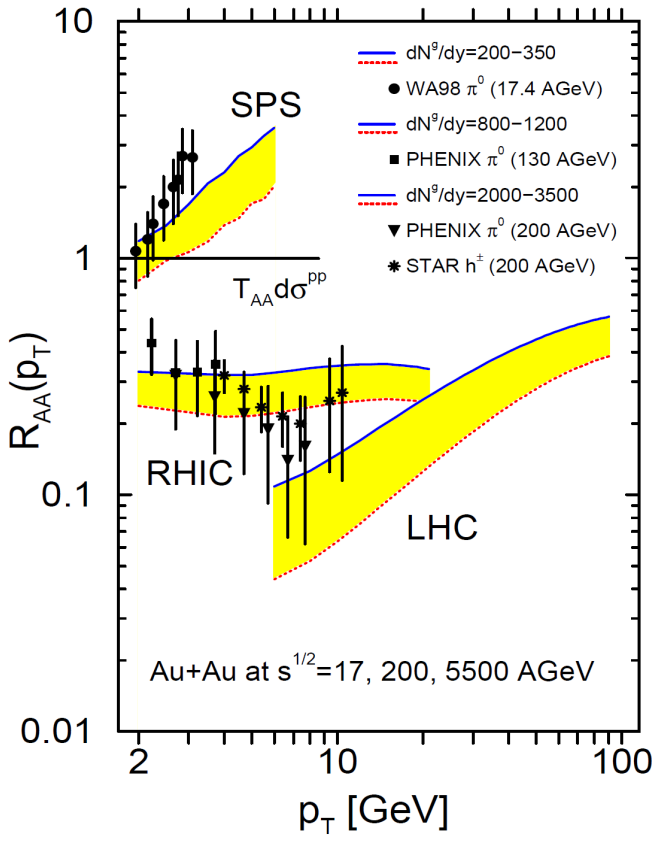

Figure 6.3: The suppression/enhancement of $R_{AA}(p_\perp)$ for π^0 produced in A+A collisions at SPS, RHIC and LHC (predictions). The relative importance of 'cold' nuclear matter effects with respect to parton energy loss is shown to diminish for increasing $\sqrt{s_{NN}}$ energies and transverse momenta. Taken from [13].

6.2 Jet tomography at RHIC

All RHIC experimental results have confirmed the substantially flat behavior of R_{AA} for several hadronic species in Au+Au reactions up to 20 GeV [115, 11, 254]. Applying several distinct energy loss formalisms, pre-

dictions were extended to this energy range: the opacity expansion (GLV) [184, 185, 186, 166, 187, 188, 164, 189, 13, 240, 17, 31], the multiple soft scattering approximation (BDMPS-Z) [171, 172, 173, 174, 175, 176, 177, 178, 179, 180, 165], the derived quenching weights (ASW) [181, 182, 183, 255, 256, 257], higher twist [190, 191, 192], and finite temperature field theory (AMY) [193, 194, 120, 195, 196, 197, 198].

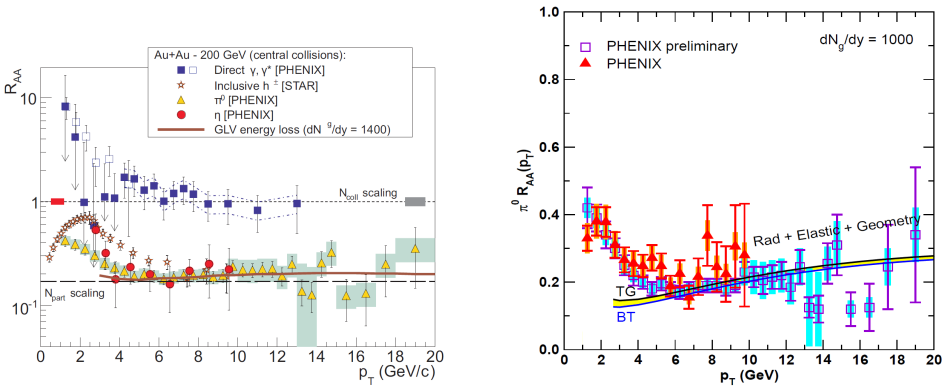

Figure 6.4: *left* $R_{AA}(p_\perp)$ measured in central Au+Au collisions at $\sqrt{s_{NN}} =$ 200 GeV. Π^0 data [14] show flat suppression across the whole $p_\perp$ range, as predicted by the GLV model. Measurements of direct photon [15], which are not subject to color interactions, confirm the scaling of R_{AA} with N_{binary}. Taken from [16]. *right* Details of π^0 suppression, as computed by the WHDG model [17].

The remarkable good agreement with data displayed by all models (Fig. 6.4 and 6.5), however, should not induce us to premature celebrations: if the goal was to uniquely characterize the medium by parameters like its density, or transport coefficients, one should observe that few of the models agree on the extrapolated values. We note that a direct comparison among the four theoretical approaches is impaired by the different medium scaling laws that

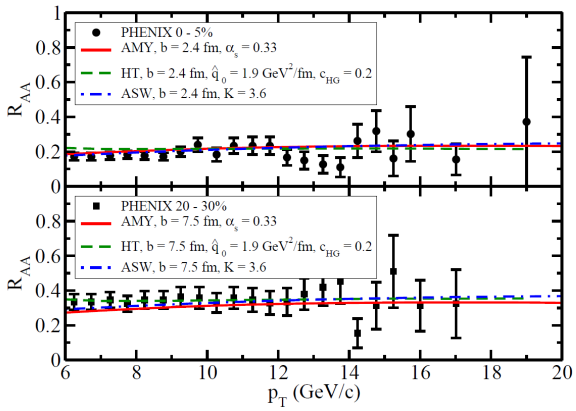

Figure 6.5: Nuclear modification factor in Au+Au collisions at $0-5\%$ (top) and $20-30\%$ centrality calculated in the ASW, HT and AMY approaches compared to data from PHENIX [18]. Taken from [19].

each model considers as the natural choice, namely rapidity density for GLV, transport coefficient $\hat{q}$ for ASW, temperature scaling for AMY and entropy density for HT. Choosing to perform the jet energy loss calculation with temperature scaling $\sim T^3$ for all approaches, and deriving the corresponding $\hat{q}$ at $\tau = 0.6$ fm/c for a central Au+Au event, one can find that the correct fit to the data is obtained for $\hat{q} = 1.9$ GeV^2/fm for GLV (only radiative, $dNdy = 1400$), $\hat{q} = 10$ GeV^2/fm for ASW, $\hat{q} = 4.1$ GeV^2/fm for AMY $\hat{q} \approx 2.3$ GeV^2/fm for HT [19]. An extended comparison among the latter three models is given in [19, 258]

6.2.1 Heavy quark puzzle

The situation became even more complicated as soon as the first results on open heavy flavor quenching via non-photonic electron measurements were made available [259, 260, 261, 262, 263, 20, 21], showing a surprising affinity with light hadron results. Using an anecdote by Prof. Gyulassy, the discovery was analogous to a "rolling bowling ball being stopped by a field of daisies", and led to the identification of the so-called Heavy Quark Puzzle [264, 240, 17, 265]: all experimental observations disagreed with predictions, jeopardizing the chances of applying jet tomography principles to heavy probes within the same consistent framework.

The assumption that elastic energy losses are negligible compared to radiative was revisited [169], and a new model was developed, the WHDG [17]. By including elastic losses and a better treatment of the collision geometry and plasma expansion, the authors were able to reduce significantly the discrepancy between light and heavy jet quenching, even though agreement with data was still far from reality (Fig. 6.6).

CUJET

It is in this context that the development of CUJET started, as part of the ongoing JET Collaboration [30] effort to construct more powerful numerical codes necessary to (1) reduce previous large theoretical and numerical systematic uncertainties [202] , which have hindered quantitative jet tomography; (2) predict new observables that could better discriminate between

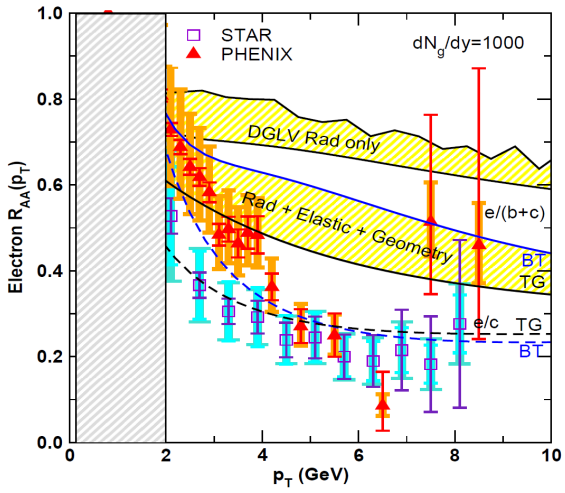

Figure 6.6: Non-photonic electron R_{AA} from WHDG is compared to RHIC data. The upper yellow band takes into account radiative energy loss only; the lower yellow band includes elastic contributions. The fit is constrained by the π^0 fit already shown in Fig. 6.4-*right*. Taken from [17].

energy loss models.

Upgraded detectors at RHIC and the built-in heavy quark capabilities of the ALICE, ATLAS, and CMS detectors at LHC were soon going to open a new chapter in jet tomography by allowing for the first time the measurement of the jet parton flavor $a = g, u, c, b$ and mass dependence of nuclear modification factors, $R_{AA\to a\to f}(p_T; \sqrt{s})$, for a wide variety of final fragments, e.g. $f = \pi, D, B, e^-$, over broader kinematic ranges and higher center of mass energies than previously available.

CUJET, by extending the development of the GLV, DGLV, and WHDG opacity series approaches and by including several novel dynamical features (cf. Chapter 4), would have been in the unique position to make accurate

predictions of the nuclear modification factor observed at RHIC and LHC, for both pions and open heavy flavors, within the same consistent theoretical framework.

The first application of CUJET is to address the key open A+A phenomenology problem of heavy quark jet quenching. We report here the results published in [31, 32].

To illustrate the proposed jet flavor tomography test of jet-medium dynamical models, we take the pure dynamical HTL limit, computed at first order in opacity. Elastic energy losses are included as well, and the coupling constant is assumed fixed, for the time being. The quark gluon plasma and jet production spectra are modeled as outlined in Section 5.2.2, using the same default parameters.

Our central physical tomographic assumption leading to our main RHIC result, Fig. 6.7, is that aside from the unavoidable $\sqrt{s}$ dependence of the initial pQCD partonic invariant cross sections, the only $\sqrt{s}$ dependent nuclear input in CUJET is the variation of the bulk final pion rapidity density, dN/dy. Given $dN/dy = 1000$, we fix the RHIC partonic level to constrain one reference point of pion $R^{\pi}_{AA}(p_T = 10 \text{ GeV}) = 0.2$, setting $\alpha_s = 0.3$. The robustness of our results, i.e. the insensitivity of the level crossing pattern to the various systematic uncertainties of the model (cf. Section 5.3), is granted by the freedom to fit the above reference point by varying the coupling parameter $\alpha_s = 0.3 \pm 0.03$. Because CUJET includes the dynamical magnetic

enhancement, this moderate coupling is sufficient to account for the RHIC data with $dN/dy = 1000$, as we check in Fig. 6.7-*right*.

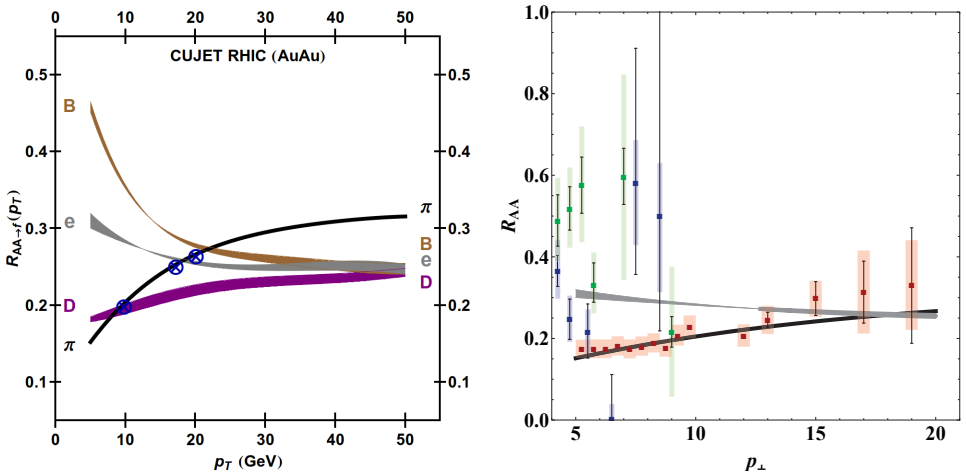

Figure 6.7: Jet flavor tomography. *left* Illustration of the level crossing pattern of nuclear modification factors versus p_T at $y = 0$. π, D, B, e fragmentation from quenched g, u, c, b jets is computed at RHIC in Au+Au central (5%) collisions. R_{AA} is constrained at RHIC, given $dN_g/dy(RHIC) = 1000$ and $\tau_0 = 1$ fm/c, by a fit to a reference point $R^{\pi}_{AA}(p_\perp = 10 \text{ GeV}) = 0.2$ setting the effective fixed coupling $\alpha_s = 0.3$. The D, B, e bands reflect the uncertainty due to the choice of NLO or FONLL initial production spectra. Setting $\tau_0 = 0$ fm/c but readjusting $\alpha_s = 0.27$ to fit our reference pion point, the crossing points (crossed blue circles) are only slightly offset. Note the possible partial inversion of π, D, B levels predicted by CUJET at high p_T at RHIC arising from competing dependencies of the energy loss and of the initial pQCD spectral shapes on the parton mass. *right* π (black) and e (gray) predictions are compared to pion data (red, PHENIX []) and non-photonic electron data (green, PHENIX [20]; blue, STAR [21]).

The novel inversion of the $\pi < D < e < B$ R_{AA} hierarchy ordering at high p_T, Fig. 6.7-*left*, is due to the interplay between energy loss and steeper initial invariant jet distributions of c and b jets at RHIC, as already noted in Sec. 5.3 and also in [266]. The splitting between pion and electron R_{AA} is found to

remain quite evident below 10 GeV in spite of the use of the dynamically enhanced potential. Nevertheless, with respect to WHDG, the value of the electron nuclear modification factor is sensibly lower and consistent with the available data, as shown on the right side of the figure, where predictions are compared with the latest PHENIX and STAR data.

If, on one hand, this could be a solution to the heavy quark puzzle, on the other hand we believe that present uncertainties in the non-photonic electron data do not allow to discriminate between the models, and only the separate contribution of open D and B mesons could provide stringent new constraints on the assumed jet-medium interaction mechanism.

The importance of experimentally isolating and observing charged heavy mesons cannot be overstated since the mass splitting between c and b jets is a particularly robust prediction of pQCD in a deconfined QGP medium.

6.3 Jet tomography at LHC

The extensive studies of hard probes performed at RHIC at energies $0.02 < \sqrt{s_{NN}} < 0.2$ TeV were extended to much higher energies $\sqrt{s_{NN}} = 2.76$ TeV at LHC [267, 268, 269, 270, 23]. The first experimental results on the nuclear modification factor showed that R_{AA} increases with $p_\perp$, as opposed to the relatively flat result observed at RHIC for $p_\perp < 20$ GeV, and in agreement with any prediction made by pQCD-based energy loss models [271].

CUJET

The second application of CUJET is aimed at studying the phenomenology of the QGP at the higher energies and densities reached at LHC.

Assuming that the charged particle pseudo-rapidity density $dN_{ch}^{LHC}/d\eta = 1600$, reported by ALICE [22] for central Pb+Pb collisions and confirmed by CMS [272] and ATLAS [273] experiments, translates directly into a 2.2 increase factor of the density ρ_{QGP} at LHC relative to RHIC (for the same centrality), we perform a parameter-free RHIC-constrained extrapolation to LHC assuming again a fixed coupling constant that does not vary with $\sqrt{s}$: $\alpha_s = 0.3$. The results are shown in Fig. 6.8.

The constrained jet flavor tomographic pattern is shown on the left side. With the much wider kinematic window accessible at LHC, the predicted flavor-dependent p_T spectrum of nuclear modifications is seen to involve again multiple level crossings. These are qualitatively different than at RHIC energies because of the complicated interplay between flavor dependent spectral shapes and opacity enhanced jet energy loss.

However, if on one side the absolute value of the nuclear modification factor depends sensitively on specific dynamical mechanics such as the effective coupling, initial formation time and freeze-out, on the other side the shape of the level crossings is not: the jet flavor quenching pattern, function of only p_T, $\sqrt{s}$, centrality and nuclear mass variations, appears as a particularly promising observable that could help discriminating among jet-medium dynamical models.

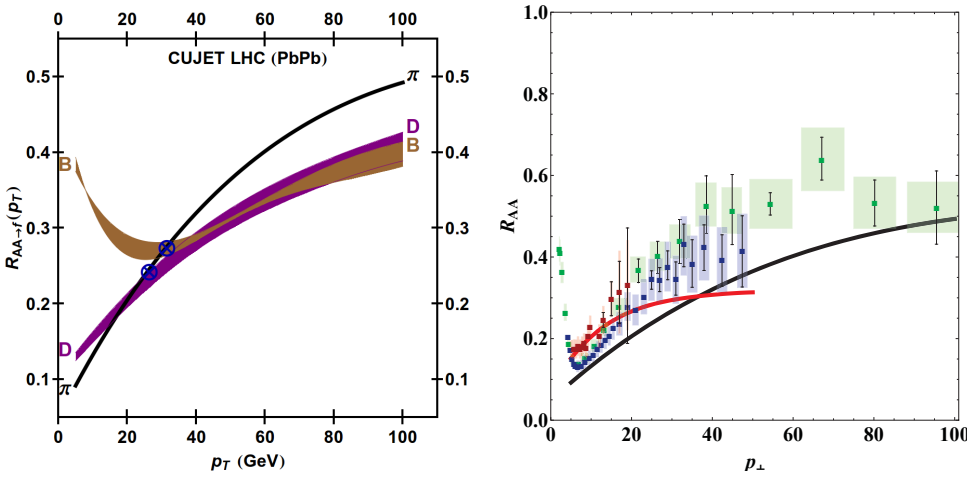

Figure 6.8: *left* Level crossing pattern of nuclear modification factors at LHC. The Au+Au RHIC results of Fig. 6.7 are extrapolated parameter-free to Pb+Pb 5% centrality at LHC. The extrapolation to LHC assumes $dN_{ch}/d\eta$ scaling of the opacity as measured by ALICE [22]. Note the total inversion of π, D, B levels predicted by CUJET at high p_T at LHC. *right* π LHC (black) and RHIC (red) predictions are compared to LHC pion data (green, CMS [23]; blue, ALICE [24]) as well as RHIC pion data (red, from Fig. 6.7) for comparison.

For comparison, we show on the right side of Fig. 6.8 the CUJET constrained predictions along with central PHENIX (RHIC) and preliminary ALICE and CMS π^0 data.

6.3.1 Surprising transparency

The pion R_{AA} theoretical curve computed with CUJET and shown in Fig. 6.8 clearly tends to fall below the preliminary LHC results. It turns out that this is a common issue that most of the quenching models face: the $p_\perp$ dependence of the nuclear modification factor measured at $\sqrt{s_{NN}} = 2.76$

TeV is steeper than expected, and the models systematically overpredict the energy loss. The quark gluon plasma probed at the LHC seems surprisingly transparent to hard probes [223, 274].

A possible solution was given in [31, 275, 276], suggesting the intriguing possibility that the effective jet-medium coupling at LHC could be weaker than at RHIC. This motivated us to explore the running coupling effects on the energy loss presented in Chapter 4.4 and 5.3.

In Fig 4.9 and 5.17 we showed the softened dependence of $\Delta E/E$ with E and the increased slope of R_{AA} with $p_\perp$ that result from the inclusion of a strong running coupling which scales with $q_\perp^2$ and $k_\perp^2/x(1-x)$. It is then reasonable to expect that new refined predictions applied to the LHC phenomenology will result in a better agreement with data.

Given $dN/dy = 2200$, we now constrain one reference point $R_{AA}^{\pi}(p_\perp = 40\,\text{GeV}, \sqrt{s_{NN}} = 2.76\,\text{TeV}) = 0.35$, setting $\alpha_0 = 0.4$. We remind that α_0 is the saturation value of $\alpha_s(Q^2)$ below $Q^2 \sim 1\,\text{GeV}^2$. The backward extrapolation to RHIC is then parameter free, assuming that α_0 does not vary with $\sqrt{s}$: only the initial rapidity density $dN/dy = 1000$ and the jet production spectra are modified. This is an inversion of the standard practice to fit the data at RHIC and extrapolate to LHC, which reflects the need to probe a much broader range of energies, once inaccessible at RHIC.

The agreement of the new running coupling CUJET predictions [33, 34] with data, reported here in Fig 6.9, is striking. On the left panel, preliminary ALICE and CMS data indicate a rather fast increase of R_{AA} for $p_\perp \lesssim 50$

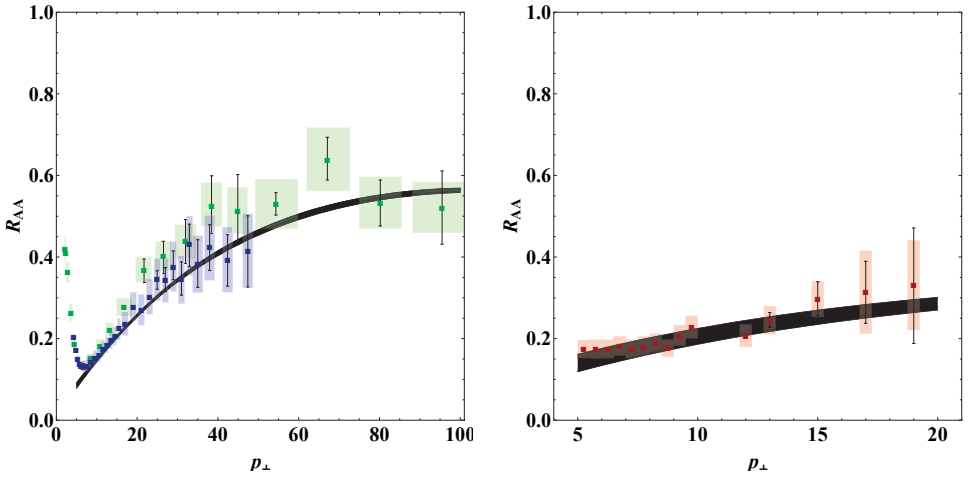

Figure 6.9: Running coupling CUJET predictions of pion R_{AA} versus p_T in Pb+Pb central collisions at LHC (*left*) and extrapolated down to Au+Au at RHIC (*right*). R_{AA} is constrained at LHC, given $dN_g/dy(LHC) = 2200$, by a fit to a reference point $R^{\pi}_{AA}(p_T = 40 \text{ GeV}) = 0.35$ setting the running coupling saturation value $\alpha_0 = 0.4$. The extrapolation to RHIC is parameter-free and only assumes $dN_g/dy(RHIC) = 1000$. The error bands reflect the uncertainty due to the choice of running scales Q^2 in $\alpha_s(Q^2)$. Data are taken from [23, 24].

GeV, and a tendency to flatten out at higher momenta, well explained by our computations which reach the asymptotic value of $R_{AA} \sim 0.6$ for $p_\perp \gtrsim 100$ GeV. On the right panel, the updated RHIC predictions are shown to be still consistent with a very slow increase of R_{AA}: running coupling effects have a negligible impact given the limited range of energies at play.

Open heavy flavor R_{AA} is also compared in Fig. 6.10 with the latest preliminary D meson and non-photonic electron data as measured by ALICE [277, 25]. Even though the limited available range of transverse momentum is

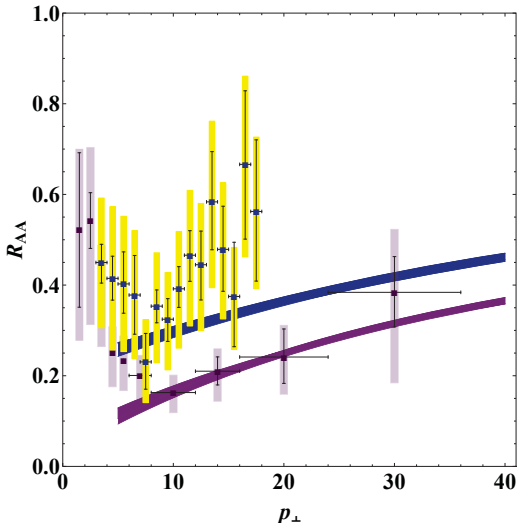

Figure 6.10: Running coupling CUJET predictions of D meson (purple) and B meson (blue) nuclear modification factors at LHC. The parameter-free results are constrained by the same fit to a LHC reference point $R^{\pi}_{AA}(p_T = 40\ \text{GeV}) = 0.35$ as in Fig. 6.9. LHC D meson data (purple, ALICE [25]) and B meson data (yellow, ALICE [25]) are added for comparison.

not enough to confirm the flavor level crossing pattern predicted by CUJET, the satisfactory agreement with data indicates a remarkable robustness of the model: heavy meson predictions, in fact, are again completely parameter free and constrained by the above fit to pions.

Future measurements across an extended range of energies, for heavy D and especially B mesons at RHIC and LHC, will test CUJET predictions of the nuclear modification factor and add new constraints on the phenomenology of jet quenching.

6.4 Azimuthal flow

High $p_\perp$ observations at RHIC and LHC are not limited to the measurement of nuclear modification factors in central collisions. The dependence of particles yields on the event centrality, for instance, allows the study of jet quenching in increasingly less dense and thinner plasmas. Another aspect to consider is the angular dependence of the particle spectra, which becomes relevant in peripheral events. Here the transverse section of the thermalized plasma assumes an irregular almond-like shape while pressure gradients attempt to restore azimuthal symmetry during the early stages of medium evolution.

In Chapter 1 we noted how the measurement of the bulk elliptic flow v_2, defined in Eq. (1.45), and the remarkable agreement with hydrodynamical predictions, shown in Fig. 1.12, provide strong indications of the formation of a hot deconfined plasma. The same observations applied to high $p_\perp$ particles, on the other hand, could offer additional insight on the jet-medium coupling and provide new constraints on the plasma parameters [278] as well as on the proposed energy loss mechanisms.

Current predictions formulated in a pQCD framework [279] get mixed response when compared to available data, as shown in Fig. 6.11 (RHIC) and Fig. 6.12 (LHC). As opposed to R_{AA}, where jet quenching appears to be the dominant effect already at $p_\perp \gtrsim 5$ GeV, here the same constrained

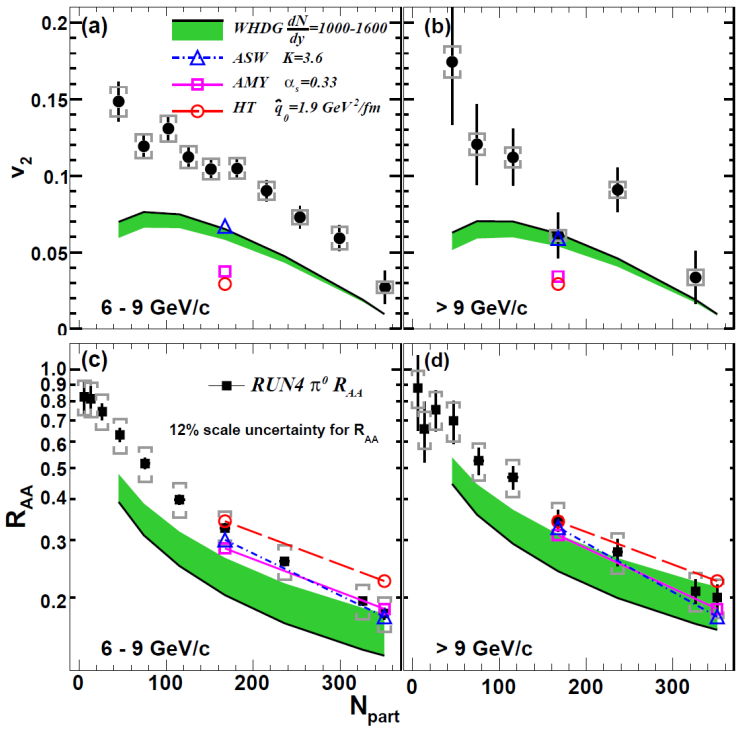

Figure 6.11: Elliptic flow v_2 (upper figures) and R_{AA} (lower figures) versus N_{part}, measured in Au+Au collisions at $\sqrt{s_{NN}} = 200$ GeV. Each are compared with four pQCD models: WHDG, ASW, HT, AMY. The agreement between data and theoretical curves worsen for higher centralities and lower transverse momenta. Taken from [26].

theoretical approach leads to a surprising underestimation of the azimuthal flow for $p_\perp < 10 \sim 15$ GeV. The agreement with data clearly worsen as the centrality (number of participants) increases (decreases). As if this weren't enough, recent analysis [280] suggest that with the proper inclusion of the transverse plasma expansion in the theoretical computations, the mismatch between predictions and data would widen as the calculated v_2 drops further below the observed value [281].

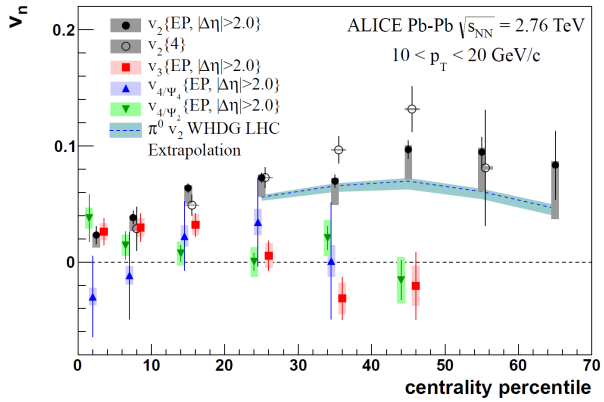

Figure 6.12: Azimuthal flow v_2 integrated over transverse momentum range $10 < p_\perp < 20$ GeV/c as a function of collision centrality. The dashed line represents the WHDG model calculations for neutral pions extrapolated to the LHC collision energy. Taken from [27].

CUJET, in its present stage of development, is capable of making both non-central R_{AA} and v_2 predictions, which do not differ much from the WHDG curves shown above. However, as mentioned already in the previous Chapter, the approximations made in the development of the model do not make it fit to provide precise quantitative non-central results. In particular, the sensitivity of the azimuthal flow to the transverse evolution of the plasma requires a better modeling of the medium expansion, which can be achieved for instance by implementing a 2D+1 hydro evolution rather than the current 1D+1. This is the logical next step to take in the development of CUJET, and work is already under progress.

6.4.1 Holography

Despite the success at explaining the measured nuclear modification factor, the present failure at predicting other high $p_\perp$ observables such as v_2 poses a serious threat to any pQCD-based jet quenching model. In recent years, several new theoretical frameworks have been proposed which could address the stronger-than-expected dependence of the energy loss with the size of the plasma L and boost the v_2 anisotropy measured in highly asymmetric impact geometries.

The most notable and promising attempt has been made by string theory inspired (conformal and nonconformal) gravity-dual holographic models. Using the Anti-deSitter/Conformal Field Theory (AdS/CFT) correspondence [282, 283, 284], these models assume a strong coupling between the jet and the medium. The energy loss of a parton quenched in a thermal plasma is then described by the dynamics of its dual classical string moving in a five-dimensional AdS space with a black hole [285, 286, 287, 288].

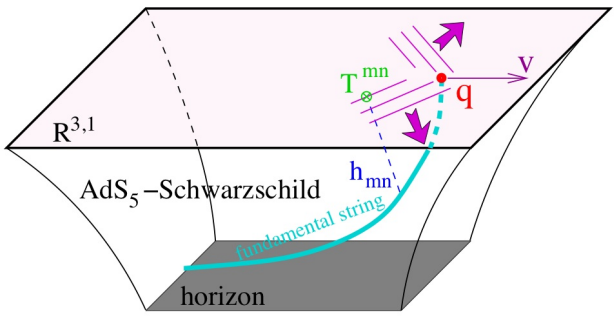

Figure 6.13: Illustration of jet quenching in gravity-dual holographic models, taken from [28].

A characteristic feature of some of the AdS/CFT models is the approximate scaling of the energy loss with L^3 for light quarks. As noted in [223], the more appropriate choice of the parameters a and b of Eq. (4.29) (cf. Section 4.4.1) for this class of models is $a = 1/3$ and $b = 2$.

In [289] the authors show that leading order AdS/CFT holography with a common large 't Hooft coupling may simultaneously describe the elliptic flow of bulk hadrons as well as the nuclear modification factor of heavy-quark jets. The consequence is that a much stronger suppression of charm particles than experimentally observed is predicted as well.

The original works also indicate a flat dependence of R_{AA} with $p_\perp$ at LHC energies, a result contradicted by the latest ALICE and CMS data reported above. In [290], however, Ficnar identifies important corrections to [287] that lead to an increase of the nuclear modification factor with $p_\perp$ [291].

6.4.2 Near T_c enhancement

Another avenue of active research is dictated by the work of Shuryak and Liao in [292, 293, 294]. Motivated by the magnetic scenario for the strongly coupled QGP, the authors point out that the jet energy loss may have a nontrivial dependence on the density and temperature of the plasma. In particular, it is shown that the inclusion of a jet quenching component with strong enhancement in the near-T_c region successfully explains the geometric data on v_2, Fig. 6.14. As stated in [29], "such an enhancement of jet-medium interactions may originate from non-perturbative structures created by the

(color-)electric jet passing a plasma of (color-)magnetic monopoles that dominate the near-T_c matter".

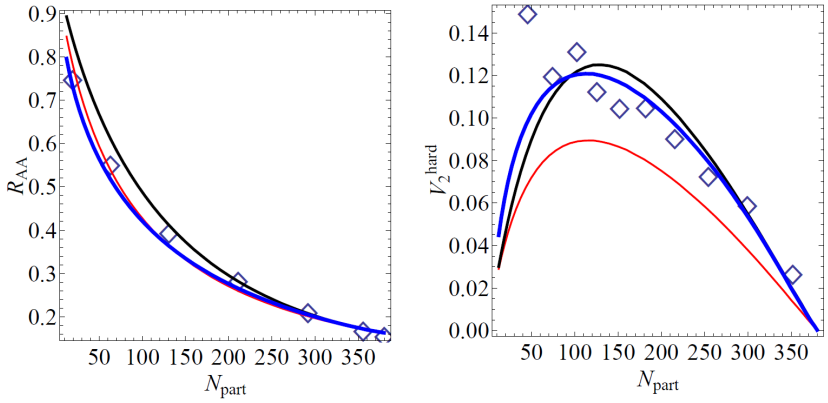

Figure 6.14: High $p_\perp = 8$ GeV hadron R_{AA} (*left*) and v_2 (*right*) versus N_{part}: a comparison between RHIC data and calculations from L^2 pQCD models (red), near-T_c enhancement models (blue) and L^3 models (black) respectively. Taken from [29]

At present time, no quantitative extensive predictions have been made in this framework, and CUJET is a possible platform candidate given the simplicity to modify its kernel and incorporate the near-T_c enhancement effects.

6.4.3 CGC initial conditions

Could the discrepancy between R_{AA}-constrained pQCD models and v_2 data be due to a wrong interpretation of the initial conditions? This possibility is explored in [225], where the authors show that a pQCD-based energy loss model coupled with color glass condensate initial conditions is compatible with currently available data.

In practical applications, such as CUJET, the Glauber model is often used to describe the initial plasma density and temperature profiles, although the CGC constitutes a more elaborate theory to describe initial conditions, as we saw in Chapter 1.

Both models, in reality, are shown to reproduce certain bulk RHIC results, even though quantities such as the initial temperature gradients, high $p_\perp$ parton distributions or size of the plasma differ considerably. One of the early LHC results, the measurement of the charged-particle multiplicity density [22], seemed to disfavor CGC initial conditions. On the other hand, more recent work [104] has demonstrated that under specific conditions both RHIC and LHC hadron multiplicities are well reproduced by CGC models.

Still an open problem of critical importance, the disentanglement among different types of initial conditions will possibly make a leap forward once the data from control p+Pb experiments are available.

Conclusions

Experimental evidence for the creation of a new form of matter, the Quark Gluon Plasma, comes from the observation of low $p_\perp$ 'bulk' properties, in particular near perfect-fluid elliptic flow that requires fast thermalization of the medium followed by low viscosity hydrodynamical expansion of the deconfined matter. The different stages of the QGP evolution, along with a summary of the underlying theoretical frameworks, were outlined in Chapter 1.

High $p_\perp$ jets observables, on the other hand, offer complementary ways to probe and characterize the properties of the plasma, understand the coupling between partons and the medium, and test the validity of perturbative QCD versus string inspired holographic methods near the phase transition of the QCD theory. Additionally, they provide further constraints on the phenomenological models that attempt a comprehensive description of the QGP physics.

Lacking the possibility to measure the transient QGP system directly

using external beams, high $p_\perp$ jets are considered the next best effective probe, calibrated via p+p and p+A collision experiments. The medium-induced modifications can then be studied to infer the nature of the plasma, much in the same way that tomography is used in medical radiology or several other fields of applied-physics.

The successful application of the tomographic method, however, requires a detailed understanding of the jet-medium physics, such as the energy loss and the transverse broadening of the jets. This thesis work was aimed to advance that understanding through the development of more powerful numerical methods that can circumvent the limitations of previous approximations or ideal analytic models.

We identified four relevant key aspects of the QGP and high $p_\perp$ partonic physics: (1) the initial conditions; (2) the plasma evolution; (3) the parton-medium coupling, i.e. energy loss; (4) the jet fragmentation. In particular, referring to the third point, we mentioned in Chapter 2 the need for a numerical algorithm able to compute the medium-induced radiation spectrum of high $p_\perp$ jets at intermediate orders in opacity, thus providing a link between the 'thin' (single hard scattering) and 'thick' (multiple soft scatterings) plasma approximations.

In this context we started the development of CUJET, a new phenomenological model that can make accurate quantitative predictions of the experimental observations carried out at RHIC and LHC.

Using Monte Carlo integration techniques, I built a flexible numerical kernel capable of performing fast computations of the $dN/dxd\mathbf{k}$ gluon distribution at intermediate orders in opacity. This core work of the thesis extended greatly the previous thesis work of Wicks by creating an open source code which meets the DOE JET Topical Collaboration milestone objective of 2015. Details about the radiation spectrum, the convergence of the opacity series expansion, or the choice of kinematic integration limits, were given in Chapter 3.

I extensively studied the effects of energy loss on heavy jets, noticing the substantial equivalence between charm and light quarks. Finally, in the context of flavor tomography, I observed that truncating the opacity series at first order is an acceptable approximation at the single inclusive nuclear modification level. Future applications to full jet shape analysis will require the power of CUJET to compute transverse momentum spectra up to 9^{th} order in opacity, which I begun to explore in this thesis.

Chapter 4 was dedicated to the improvements over the original DGLV model that CUJET added to the radiation kernel. The static scattering center approximation was replaced by a dynamical medium, where the interaction with the jets is computed in the framework of finite temperature QFT using HTL resummed gluon propagators. This approach results in an effective, dynamically screened potential which enhances the energy loss of light and heavy quarks in a mass dependent way. This feature was found

to be crucial in solving the heavy quark puzzle discovered at RHIC. I further developed a hybrid potential which interpolates between the static and dynamical medium, allowing the study of dynamical effects at intermediate opacity. At the same time, elastic contributions to the energy loss were taken into account.

A major advance made possible with the CUJET code over all previous semi-analytic attempts to compute the DGLV opacity series was the inclusion of the full jet path proper time integration over space-time dependent plasma densities. In addition, the running strong coupling constant with the multiple scales $q_\perp^2$ and $k_\perp^2/x(1-x)$ was included for the first time. Both the features were found to be decisive to achieve a consistent simultaneous account of the RHIC and LHC nuclear jet modification measurements. In particular, the running of the jet-medium coupling naturally solved the at-first puzzling 'transparency' of the LHC plasma relative to the lower density QGP produced at RHIC energies.

In Chapter 5, we progressively constructed the CUJET model, paying attention to all the phases of the plasma evolution. The medium density profile, as well as the high $p_\perp$ jet distribution, are set by Glauber initial conditions. The plasma expands longitudinally according to the Bjorken model (1D+1 evolution), while the partons propagate through the medium until the value of the Debye screening mass drops below Λ_{QCD}. Both elastic and radiative energy losses are taken into account, and the jets are assumed

to fragment in vacuum.

In Section 5.3, we computed the nuclear modification factor and performed an extensive study of the systematic uncertainties that affect CUJET. The theory relies only on one single free parameter, either the effective coupling α_s or the saturation value of the running coupling below $Q^2 \sim 1$ GeV^2, which is constrained by the fit to one reference $p_\perp$ point in central R_{AA}.

The main results of CUJET, to be compared to the latest RHIC and LHC data, were shown in Chapter 6, which is fully dedicated to the study of the nuclear modification factor. Because CUJET includes the dynamical magnetic enhancement, a moderate coupling $\alpha_s = 0.3$ is sufficient to account for the RHIC data with the initial rapidity density set to $dN/dy = 1000$. The fit of α_s was performed against the RHIC pion data at a given value of transverse momentum, $R^\pi_{AA}(p_\perp = 10\,\text{GeV}, \sqrt{s_{NN}} = 200\,\text{GeV}) = 0.2$, and the constrained-extrapolation was extended to different flavors, D and B mesons, collision energies, $\sqrt{s_{NN}} = (0.2, 2.76)$ TeV, and initial rapidity densities, $dN/dy = 1000, 2200$.

CUJET predicts a striking and novel level crossing pattern of flavor dependent R_{AA} both at RHIC and LHC, that we proposed as a clear new signature of pQCD based energy loss models. The conventionally expected hierarchy order $\pi < D < e < B$ was shown to be inverted at high values of the $p_\perp$ range. The importance of testing those predictions with future experimental data, relative to flavor tagged jet fragments at both RHIC and

LHC, was properly emphasized.

In our calculation, the splitting between pion and electron R_{AA} is significantly reduced with respect to older predictions (WHDG), and found to be compatible within the large uncertainties in current nonphotonic electron data. A satisfactory solution to the Heavy Quark Puzzle has thus been provided within our purely perturbative approach to jet quenching, without the need of new holographic or other non perturbative effects.

Switching our attention to the LHC results, CUJET also offers a compelling explanation for the relative plasma transparency observed at rapidity densities two times higher than at RHIC. The inclusion of the running coupling mechanism, in fact, dramatically improves the agreement between predictions and data and explains most of the features observed in the pion R_{AA} measurements, in particular the rapid rise in $p_\perp$ and the apparent slow saturation above $p_\perp \gtrsim 80$ GeV. The high quality of the LHC data motivated us to fit the coupling saturation value α_0 to a LHC point $R^\pi_{AA}(p_\perp = 40 \text{ GeV}, \sqrt{s_{NN}} = 2.76 \text{ TeV}) = 0.35$, and to use that calibration down to RHIC. We found remarkable parameter-free consistency with available data at both LHC and RHIC.

Future measurements across an extended range of energies, especially for heavy B mesons at RHIC and LHC, will test our predictions of the jet energy loss mass dependence in the weakly coupled QGP limit.

Looking beyond the present thesis, a wide range of other jet observables

needs systematic studies with the CUJET model. The next priority is to address the origin of the azimuthal asymmetry puzzle. This will require coupling CUJET to the state of the art viscous hydrodynamic and parton transport codes now being developed within the JET topical collaboration.

In addition, the heavy ion experimental frontier at LHC, with the ATLAS and CMS experiments, focuses on full jet measurements and the recently discovered dijet asymmetry. To address those observables, the higher order in opacity transverse spectra will need to be computed in much more detail than I did in the exploratory study reported in this thesis. Those future $k_\perp$ calculations will then have to be merged with a variety of jet finding algorithms that are being refined at this time.

Many key questions are left unanswered. The continued development of more powerful tools that will allow the model to extend its predictions to non-central, azimuthally-dependent observables, as well as jet observables, will soon open a new Chapter in the evolution of CUJET.

Bibliography

[1] Claudio Bonati, Philippe de Forcrand, Massimo D'Elia, Owe Philipsen, and Francesco Sanfilippo. Constraints on the two-flavor QCD phase diagram from imaginary chemical potential. *PoS*, LATTICE2011:189, 2011.

[2] Gunnar S. Bali. QCD forces and heavy quark bound states. *Phys.Rept.*, 343:1–136, 2001.

[3] M. Okamoto et al. Equation of state for pure SU(3) gauge theory with renormalization group improved action. *Phys.Rev.*, D60:094510, 1999.

[4] Frithjof Karsch. Lattice QCD at high temperature and density. *Lect.Notes Phys.*, 583:209–249, 2002.

[5] Larry McLerran. The CGC and the Glasma: Two Lectures at the Yukawa Insitute. *Prog.Theor.Phys.Suppl.*, 187:17–30, 2011.

[6] Javier L. Albacete. Particle multiplicities in Lead-Lead collisions at the LHC from non-linear evolution with running coupling. *Phys.Rev.Lett.*, 99:262301, 2007.

[7] Miklos Gyulassy and Larry McLerran. New forms of QCD matter discovered at RHIC. *Nucl.Phys.*, A750:30–63, 2005.

[8] A. Bazavov, T. Bhattacharya, M. Cheng, N.H. Christ, C. DeTar, et al. Equation of state and QCD transition at finite temperature. *Phys.Rev.*, D80:014504, 2009.

[9] John Adams et al. Particle type dependence of azimuthal anisotropy and nuclear modification of particle production in Au + Au collisions at s(NN)**(1/2) = 200-GeV. *Phys.Rev.Lett.*, 92:052302, 2004.

[10] Michele Arneodo. Nuclear effects in structure functions. *Phys.Rept.*, 240:301–393, 1994.

[11] K. Adcox et al. Formation of dense partonic matter in relativistic nucleus-nucleus collisions at RHIC: Experimental evaluation by the PHENIX collaboration. *Nucl.Phys.*, A757:184–283, 2005.

[12] S.S. Adler et al. Mid-rapidity neutral pion production in proton proton collisions at $\sqrt{s}$ = 200-GeV. *Phys.Rev.Lett.*, 91:241803, 2003.

[13] Ivan Vitev and Miklos Gyulassy. High p_T tomography of d + Au and Au+Au at SPS, RHIC, and LHC. *Phys.Rev.Lett.*, 89:252301, 2002.

[14] S.S. Adler et al. Suppressed π^0 production at large transverse momentum in central Au+ Au collisions at S(NN)**(1/2) = 200 GeV. *Phys.Rev.Lett.*, 91:072301, 2003.

[15] S.S. Adler et al. Centrality dependence of direct photon production in s(NN)**(1/ 2) = 200-GeV Au + Au collisions. *Phys.Rev.Lett.*, 94:232301, 2005.

[16] David d'Enterria and Barbara Betz. High-p(T) hadron suppression and jet quenching. *Lect.Notes Phys.*, 785:285–339, 2010.

[17] Simon Wicks, William Horowitz, Magdalena Djordjevic, and Miklos Gyulassy. Elastic, inelastic, and path length fluctuations in jet tomography. *Nucl.Phys.*, A784:426–442, 2007.

[18] Maya Shimomura. High-p(T) pi0, eta, identified and inclusive charged hadron spectra from PHENIX. *Nucl.Phys.*, A774:457–460, 2006.

[19] Steffen A. Bass, Charles Gale, Abhijit Majumder, Chiho Nonaka, Guang-You Qin, et al. Systematic Comparison of Jet Energy-Loss Schemes in a realistic hydrodynamic medium. *Phys.Rev.*, C79:024901, 2009.

[20] A. Adare et al. Heavy Quark Production in $p + p$ and Energy Loss and Flow of Heavy Quarks in Au+Au Collisions at $\sqrt{s_N N} = 200$ GeV. *Phys.Rev.*, C84:044905, 2011.

[21] Mustafa Mustafa. Measurements of Non-photonic Electron Production and Azimuthal Anisotropy in $\sqrt{s_{NN}} = 39$, 62.4 and 200 GeV Au+Au Collisions from STAR at RHIC. 2012.

[22] B Abelev et al. Charged-particle multiplicity density at mid-rapidity in central Pb-Pb collisions at $\sqrt{s_{NN}} = 2.76$ TeV. *Phys.Rev.Lett.*, 105:252301, 2010.

[23] Serguei Chatrchyan et al. Study of high-pT charged particle suppression in PbPb compared to *pp* collisions at $\sqrt{s_{NN}} = 2.76$ TeV. *Eur.Phys.J.*, C72:1945, 2012.

[24] Betty Abelev et al. Centrality Dependence of Charged Particle Production at Large Transverse Momentum in Pb–Pb Collisions at $\sqrt{s_{\rm NN}} =$ 2.76 TeV. *Phys.Lett.*, B720:52–62, 2013.

[25] Z. Conesa del Valle. Heavy-flavor suppression and azimuthal anisotropy in Pb-Pb collisions at $\sqrt{(}s_{NN}) = 2.76$ TeV with the ALICE detector. 2012.

[26] A. Adare et al. Azimuthal anisotropy of neutral pion production in Au+Au collisions at $\sqrt{(}s_N N) = 200$ GeV: Path-length dependence of jet quenching and the role of initial geometry. *Phys.Rev.Lett.*, 105:142301, 2010.

[27] Betty Abelev et al. Anisotropic flow of charged hadrons, pions and (anti-)protons measured at high transverse momentum in Pb-Pb collisions at $\sqrt{(}s_{NN}) = 2.76$ TeV. 2012.

[28] Gubser online repository. *www.princeton.edu/physics*.

[29] Jinfeng Liao. Non-perturbative Jet Quenching from Geometric Data. *AIP Conf.Proc.*, 1441:874–876, 2012.

[30] JET: Jet and Electromagnetic Tomography. Us-doe nuclear science topical collaboration. *http://jet.lbl.gov/overview*, Grants N. DE-FG02-93ER40764 and DE-AC02-05CH11231.

[31] Alessandro Buzzatti and Miklos Gyulassy. Jet Flavor Tomography of Quark Gluon Plasmas at RHIC and LHC. *Phys.Rev.Lett.*, 108:022301, 2012.

[32] Alessandro Buzzatti and Miklos Gyulassy. Dynamical magnetic enhancement of light and heavy quark jet quenching at RHIC. *Nucl.Phys.*, A855:307–310, 2011.

[33] Alessandro Buzzatti and Miklos Gyulassy. An overview of the CUJET model: Jet Flavor Tomography applied at RHIC and LHC. 2012.

[34] Alessandro Buzzatti and Miklos Gyulassy. A running coupling explanation of the surprising transparency of the QGP at LHC. *Nucl.Phys.A*, 2012.

[35] Donald A. Glaser. Some effects of ionizing radiation on the formation of bubbles in liquids. *Phys. Rev.*, 87:665–665, Aug 1952.

[36] Yuval Ne'eman. Derivation of strong interactions from a gauge invariance. *Nucl.Phys.*, 26:222–229, 1961.

[37] Murray Gell-Mann. Symmetries of baryons and mesons. *Phys.Rev.*, 125:1067–1084, 1962.

[38] V.E. Barnes, P.L. Connolly, D.J. Crennell, B.B. Culwick, W.C. Delaney, et al. Observation of a Hyperon with Strangeness -3. *Phys.Rev.Lett.*, 12:204–206, 1964.

[39] Murray Gell-Mann. A Schematic Model of Baryons and Mesons. *Phys.Lett.*, 8:214–215, 1964.

[40] G. Zweig. An SU(3) model for strong interaction symmetry and its breaking. 1964.

[41] M.Y. Han and Yoichiro Nambu. Three Triplet Model with Double SU(3) Symmetry. *Phys.Rev.*, 139:B1006–B1010, 1965.

[42] H. Fritzsch and M. Gell-Mann. Light cone current algebra. 1971.

[43] Harald Fritzsch and Murray Gell-Mann. Current algebra: Quarks and what else? *eConf*, C720906V2:135–165, 1972.

[44] Richard P. Feynman. Very high-energy collisions of hadrons. *Phys.Rev.Lett.*, 23:1415–1417, 1969.

[45] R.P. Feynman. The behavior of hadron collisions at extreme energies. *Conf.Proc.*, C690905:237–258, 1969.

[46] J.D. Bjorken. Asymptotic Sum Rules at Infinite Momentum. *Phys.Rev.*, 179:1547–1553, 1969.

[47] H. Fritzsch, Murray Gell-Mann, and H. Leutwyler. Advantages of the Color Octet Gluon Picture. *Phys.Lett.*, B47:365–368, 1973.

[48] D.J. Gross and Frank Wilczek. Ultraviolet Behavior of Nonabelian Gauge Theories. *Phys.Rev.Lett.*, 30:1343–1346, 1973.

[49] H. David Politzer. Reliable Perturbative Results for Strong Interactions? *Phys.Rev.Lett.*, 30:1346–1349, 1973.

[50] A. De Rujula, Howard Georgi, and S.L. Glashow. Hadron Masses in a Gauge Theory. *Phys.Rev.*, D12:147–162, 1975.

[51] Helmut Satz. Color deconfinement in nuclear collisions. *Rept.Prog.Phys.*, 63:1511, 2000.

[52] Yoichiro Nambu and G. Jona-Lasinio. Dynamical Model of Elementary Particles Based on an Analogy with Superconductivity. 1. *Phys.Rev.*, 122:345–358, 1961.

[53] Yoichiro Nambu and G. Jona-Lasinio. DYNAMICAL MODEL OF ELEMENTARY PARTICLES BASED ON AN ANALOGY WITH SUPERCONDUCTIVITY. II. *Phys.Rev.*, 124:246–254, 1961.

[54] Tetsuo Hatsuda and Teiji Kunihiro. QCD phenomenology based on a chiral effective Lagrangian. *Phys.Rept.*, 247:221–367, 1994.

[55] Steven Weinberg. Phenomenological Lagrangians. *Physica*, A96:327, 1979.

[56] J. Gasser and H. Leutwyler. Chiral Perturbation Theory to One Loop. *Annals Phys.*, 158:142, 1984.

[57] J. Gasser and H. Leutwyler. Chiral Perturbation Theory: Expansions in the Mass of the Strange Quark. *Nucl.Phys.*, B250:465, 1985.

[58] Mikhail A. Shifman, A.I. Vainshtein, and Valentin I. Zakharov. QCD and Resonance Physics. Sum Rules. *Nucl.Phys.*, B147:385–447, 1979.

[59] Pietro Colangelo and Alexander Khodjamirian. QCD sum rules, a modern perspective. 2000.

[60] Kenneth G. Wilson. Confinement of Quarks. *Phys.Rev.*, D10:2445–2459, 1974.

[61] A. Chodos, R.L. Jaffe, K. Johnson, Charles B. Thorn, and V.F. Weisskopf. A New Extended Model of Hadrons. *Phys.Rev.*, D9:3471–3495, 1974.

[62] A. Chodos, R.L. Jaffe, K. Johnson, and Charles B. Thorn. Baryon Structure in the Bag Theory. *Phys.Rev.*, D10:2599, 1974.

[63] Thomas A. DeGrand, R.L. Jaffe, K. Johnson, and J.E. Kiskis. Masses and Other Parameters of the Light Hadrons. *Phys.Rev.*, D12:2060, 1975.

[64] Edward V. Shuryak. The QCD vacuum, hadrons and the superdense matter. *World Sci.Lect.Notes Phys.*, 71:1–618, 2004.

[65] Edward V. Shuryak. TWO SCALES AND PHASE TRANSITIONS IN QUANTUM CHROMODYNAMICS. *Phys.Lett.*, B107:103, 1981.

[66] Robert D. Pisarski. Phenomenology of the Chiral Phase Transition. *Phys.Lett.*, B110:155, 1982.

[67] Alexander M. Polyakov. String Representations and Hidden Symmetries for Gauge Fields. *Phys.Lett.*, B82:247–250, 1979.

[68] Yoichiro Nambu. Axial vector current conservation in weak interactions. *Phys.Rev.Lett.*, 4:380–382, 1960.

[69] John Bardeen, L.N. Cooper, and J.R. Schrieffer. Theory of superconductivity. *Phys.Rev.*, 108:1175–1204, 1957.

[70] J. Goldstone. Field Theories with Superconductor Solutions. *Nuovo Cim.*, 19:154–164, 1961.

[71] I.J.R. Aitchison and A.J.G. Hey. Gauge theories in particle physics: A practical introduction. Vol. 2: Non-Abelian gauge theories: QCD and the electroweak theory. 2004.

[72] K. Yagi, T. Hatsuda, and Y. Miake. Quark-gluon plasma: From big bang to little bang. *Camb.Monogr.Part.Phys.Nucl.Phys.Cosmol.*, 23:1–446, 2005.

[73] Robert D. Pisarski and Frank Wilczek. Remarks on the Chiral Phase Transition in Chromodynamics. *Phys.Rev.*, D29:338–341, 1984.

[74] Rajan Gupta. Introduction to lattice QCD: Course. pages 83–219, 1997.

[75] Leonard Susskind. Lattice Fermions. *Phys.Rev.*, D16:3031–3039, 1977.

[76] Holger Bech Nielsen and M. Ninomiya. Absence of Neutrinos on a Lattice. 1. Proof by Homotopy Theory. *Nucl.Phys.*, B185:20, 1981.

[77] Holger Bech Nielsen and M. Ninomiya. Absence of Neutrinos on a Lattice. 2. Intuitive Topological Proof. *Nucl.Phys.*, B193:173, 1981.

[78] M. Creutz. QUARKS, GLUONS AND LATTICES. 1984.

[79] I. Montvay and G. Munster. Quantum fields on a lattice. 1994.

[80] M. Fukugita, M. Okawa, and A. Ukawa. ORDER OF THE DECONFINING PHASE TRANSITION IN SU(3) LATTICE GAUGE THEORY. *Phys.Rev.Lett.*, 63:1768, 1989.

[81] M. Cheng, N.H. Christ, S. Datta, J. van der Heide, C. Jung, et al. The Transition temperature in QCD. *Phys.Rev.*, D74:054507, 2006.

[82] M. Cheng, N.H. Christ, S. Datta, J. van der Heide, C. Jung, et al. The QCD equation of state with almost physical quark masses. *Phys.Rev.*, D77:014511, 2008.

[83] Pasi Huovinen and Pter Petreczky. QCD Equation of State and Hadron Resonance Gas. *Nucl.Phys.*, A837:26–53, 2010.

[84] Szabolcs Borsanyi et al. Transition temperature and the equation of state from lattice QCD, Wuppertal-Budapest results. *Acta Phys.Polon.Supp.*, 4:593–602, 2011.

[85] P. Hasenfratz and F. Karsch. Chemical Potential on the Lattice. *Phys.Lett.*, B125:308, 1983.

[86] M. Derrick et al. Extraction of the gluon density of the proton at small x. *Phys.Lett.*, B345:576–588, 1995.

[87] Marcel Froissart. Asymptotic behavior and subtractions in the Mandelstam representation. *Phys.Rev.*, 123:1053–1057, 1961.

[88] Larry D. McLerran and Raju Venugopalan. Gluon distribution functions for very large nuclei at small transverse momentum. *Phys.Rev.*, D49:3352–3355, 1994.

[89] Larry D. McLerran and Raju Venugopalan. Computing quark and gluon distribution functions for very large nuclei. *Phys.Rev.*, D49:2233–2241, 1994.

[90] L.V. Gribov, E.M. Levin, and M.G. Ryskin. Semihard Processes in QCD. *Phys.Rept.*, 100:1–150, 1983.

[91] Alfred H. Mueller and Jian-wei Qiu. Gluon Recombination and Shadowing at Small Values of x. *Nucl.Phys.*, B268:427, 1986.

[92] Edmond Iancu, Andrei Leonidov, and Larry D. McLerran. Nonlinear gluon evolution in the color glass condensate. 1. *Nucl.Phys.*, A692:583–645, 2001.

[93] Elena Ferreiro, Edmond Iancu, Andrei Leonidov, and Larry McLerran. Nonlinear gluon evolution in the color glass condensate. 2. *Nucl.Phys.*, A703:489–538, 2002.

[94] Edmond Iancu, Andrei Leonidov, and Larry D. McLerran. The Renormalization group equation for the color glass condensate. *Phys.Lett.*, B510:133–144, 2001.

[95] Alex Kovner, Larry D. McLerran, and Heribert Weigert. Gluon production at high transverse momentum in the McLerran-Venugopalan model of nuclear structure functions. *Phys.Rev.*, D52:3809–3814, 1995.

[96] T. Lappi and L. McLerran. Some features of the glasma. *Nucl.Phys.*, A772:200–212, 2006.

[97] Edmond Iancu, Kazunori Itakura, and Larry McLerran. Geometric scaling above the saturation scale. *Nucl.Phys.*, A708:327–352, 2002.

[98] A.H. Mueller and D.N. Triantafyllopoulos. The Energy dependence of the saturation momentum. *Nucl.Phys.*, B640:331–350, 2002.

[99] E. Iancu, K. Itakura, and S. Munier. Saturation and BFKL dynamics in the HERA data at small x. *Phys.Lett.*, B590:199–208, 2004.

[100] Dmitri Kharzeev, Eugene Levin, and Marzia Nardi. The Onset of classical QCD dynamics in relativistic heavy ion collisions. *Phys.Rev.*, C71:054903, 2005.

[101] Javier L. Albacete, Adrian Dumitru, and Yasushi Nara. CGC initial conditions at RHIC and LHC. *J.Phys.Conf.Ser.*, 316:012011, 2011.

[102] Dmitri Kharzeev, Yuri V. Kovchegov, and Kirill Tuchin. Cronin effect and high p(T) suppression in pA collisions. *Phys.Rev.*, D68:094013, 2003.

[103] Javier L. Albacete, Nestor Armesto, Alex Kovner, Carlos A. Salgado, and Urs Achim Wiedemann. Energy dependence of the Cronin effect from nonlinear QCD evolution. *Phys.Rev.Lett.*, 92:082001, 2004.

[104] Javier L. Albacete and Cyrille Marquet. Single Inclusive Hadron Production at RHIC and the LHC from the Color Glass Condensate. *Phys.Lett.*, B687:174–179, 2010.

[105] Dmitri Kharzeev, Eugene Levin, and Larry McLerran. Jet azimuthal correlations and parton saturation in the color glass condensate. *Nucl.Phys.*, A748:627–640, 2005.

[106] Javier L. Albacete and Cyrille Marquet. Azimuthal correlations of forward di-hadrons in d+Au collisions at RHIC in the Color Glass Condensate. *Phys.Rev.Lett.*, 105:162301, 2010.

[107] Adrian Dumitru, Kevin Dusling, Francois Gelis, Jamal Jalilian-Marian, Tuomas Lappi, et al. The Ridge in proton-proton collisions at the LHC. *Phys.Lett.*, B697:21–25, 2011.

[108] *Report of the workshop on BeV/nucleon collisions of heavy ions - how and why*, Bear Mountain, New York, Nov. 29 - Dec. 1, 1974 (BNL-AUI, 1975).

[109] T.D. Lee. A Possible New Form of Matter at High Density. (Talk). *Conf.Proc.*, C741017:65–81, 1974.

[110] T.D. Lee and G.C. Wick. Vacuum Stability and Vacuum Excitation in a Spin 0 Field Theory. *Phys.Rev.*, D9:2291, 1974.

[111] John C. Collins and M.J. Perry. Superdense Matter: Neutrons Or Asymptotically Free Quarks? *Phys.Rev.Lett.*, 34:1353, 1975.

[112] Gordon Baym. RHIC: From dreams to beams in two decades. *Nucl.Phys.*, A698:XXIII–XXXII, 2002.

[113] I. Arsene et al. Quark gluon plasma and color glass condensate at RHIC? The Perspective from the BRAHMS experiment. *Nucl.Phys.*, A757:1–27, 2005.

[114] B.B. Back, M.D. Baker, M. Ballintijn, D.S. Barton, B. Becker, et al. The PHOBOS perspective on discoveries at RHIC. *Nucl.Phys.*, A757:28–101, 2005.

[115] John Adams et al. Experimental and theoretical challenges in the search for the quark gluon plasma: The STAR Collaboration's critical assessment of the evidence from RHIC collisions. *Nucl.Phys.*, A757:102–183, 2005.

[116] Gordon Baym and David Mermin. Determination of Thermodynamic Green's Functions. *J.Math.Phys.*, 2:232, 1961.

[117] R.L. Mills. Propagators for Many-Particle Systems. *New York: Gordon and Breach*, 1969.

[118] Jean-Paul Blaizot and Edmond Iancu. The Quark gluon plasma: Collective dynamics and hard thermal loops. *Phys.Rept.*, 359:355–528, 2002.

[119] Peter Brockway Arnold, Guy D. Moore, and Laurence G. Yaffe. Transport coefficients in high temperature gauge theories. 1. Leading log results. *JHEP*, 0011:001, 2000.

[120] Peter Brockway Arnold, Guy D Moore, and Laurence G. Yaffe. Transport coefficients in high temperature gauge theories. 2. Beyond leading log. *JHEP*, 0305:051, 2003.

[121] x. x. *x*.

[122] R.J. Glauber and G. Matthiae. High-energy scattering of protons by nuclei. *Nucl.Phys.*, B21:135–157, 1970.

[123] P. Huovinen and P.V. Ruuskanen. Hydrodynamic Models for Heavy Ion Collisions. *Ann.Rev.Nucl.Part.Sci.*, 56:163–206, 2006.

[124] W. Reisdorf and H.G. Ritter. Collective flow in heavy-ion collisions. *Ann.Rev.Nucl.Part.Sci.*, 47:663–709, 1997.

[125] S. Voloshin and Y. Zhang. Flow study in relativistic nuclear collisions by Fourier expansion of Azimuthal particle distributions. *Z.Phys.*, C70:665–672, 1996.

[126] Pasi Huovinen. Hydrodynamical description of collective flow. Chapter 1. 2003.

[127] Peter F. Kolb and Ulrich W. Heinz. Hydrodynamic description of ultrarelativistic heavy ion collisions. 2003.

[128] Tetsufumi Hirano and Miklos Gyulassy. Perfect fluidity of the quark gluon plasma core as seen through its dissipative hadronic corona. *Nucl.Phys.*, A769:71–94, 2006.

[129] Derek Teaney. The Effects of viscosity on spectra, elliptic flow, and HBT radii. *Phys.Rev.*, C68:034913, 2003.

[130] Tetsufumi Hirano, Ulrich W. Heinz, Dmitri Kharzeev, Roy Lacey, and Yasushi Nara. Hadronic dissipative effects on elliptic flow in ultrarelativistic heavy-ion collisions. *Phys.Lett.*, B636:299–304, 2006.

[131] Tetsufumi Hirano and Yasushi Nara. Eccentricity Fluctuation in Initial Conditions of Hydrodynamics. *Nucl.Phys.*, A830:191C–194C, 2009.

[132] Matthew Luzum and Paul Romatschke. Conformal Relativistic Viscous Hydrodynamics: Applications to RHIC results at s(NN)**(1/2) = 200-GeV. *Phys.Rev.*, C78:034915, 2008.

[133] Tetsufumi Hirano and Keiichi Tsuda. Collective flow and two pion correlations from a relativistic hydrodynamic model with early chemical freezeout. *Phys.Rev.*, C66:054905, 2002.

[134] Huichao Song and Ulrich W. Heinz. Causal viscous hydrodynamics in 2+1 dimensions for relativistic heavy-ion collisions. *Phys.Rev.*, C77:064901, 2008.

[135] Bjorn Schenke, Sangyong Jeon, and Charles Gale. Elliptic and triangular flow in event-by-event (3+1)D viscous hydrodynamics. *Phys.Rev.Lett.*, 106:042301, 2011.

[136] A. Andronic, P. Braun-Munzinger, and J. Stachel. Hadron production in central nucleus-nucleus collisions at chemical freeze-out. *Nucl.Phys.*, A772:167–199, 2006.

[137] D. Zschiesche, S. Schramm, J. Schaffner-Bielich, Horst Stoecker, and W. Greiner. Particle ratios at RHIC: Effective hadron masses and chemical freezeout. *Phys.Lett.*, B547:7–14, 2002.

[138] Fred Cooper and Graham Frye. Comment on the Single Particle Distribution in the Hydrodynamic and Statistical Thermodynamic Models of Multiparticle Production. *Phys.Rev.*, D10:186, 1974.

[139] R.J. Fries, Berndt Muller, C. Nonaka, and S.A. Bass. Hadronization in heavy ion collisions: Recombination and fragmentation of partons. *Phys.Rev.Lett.*, 90:202303, 2003.

[140] V. Greco, C.M. Ko, and P. Levai. Parton coalescence and anti-proton / pion anomaly at RHIC. *Phys.Rev.Lett.*, 90:202302, 2003.

[141] Rudolph C. Hwa and C.B. Yang. Scaling distributions of quarks, mesons and proton for all p(T), energy and centrality. *Phys.Rev.*, C67:064902, 2003.

[142] Denes Molnar and Sergei A. Voloshin. Elliptic flow at large transverse momenta from quark coalescence. *Phys.Rev.Lett.*, 91:092301, 2003.

[143] Raymond Brock et al. Handbook of perturbative QCD: Version 1.0. *Rev.Mod.Phys.*, 67:157–248, 1995.

[144] R. Keith Ellis, W. James Stirling, and B.R. Webber. QCD and collider physics. *Camb.Monogr.Part.Phys.Nucl.Phys.Cosmol.*, 8:1–435, 1996.

[145] A. Adare et al. J/psi Production vs Centrality, Transverse Momentum, and Rapidity in Au+Au Collisions at s(NN)**(1/2) = 200-GeV. *Phys.Rev.Lett.*, 98:232301, 2007.

[146] Saumen Datta, Frithjof Karsch, Peter Petreczky, and Ines Wetzorke. Behavior of charmonium systems after deconfinement. *Phys.Rev.*, D69:094507, 2004.

[147] Helmut Satz. Colour deconfinement and quarkonium binding. *J.Phys.*, G32:R25, 2006.

[148] M. Cheng, P. Hendge, C. Jung, F. Karsch, O. Kaczmarek, et al. Baryon Number, Strangeness and Electric Charge Fluctuations in QCD at High Temperature. *Phys.Rev.*, D79:074505, 2009.

[149] Peter Petreczky, Prasad Hegde, and Alexander Velytsky. Quark number fluctuations at high temperatures. *PoS*, LAT2009:159, 2009.

[150] J.D. Bjorken. Energy Loss of Energetic Partons in Quark - Gluon Plasma: Possible Extinction of High p(t) Jets in Hadron - Hadron Collisions. 1982.

[151] John C. Collins, Davison E. Soper, and George F. Sterman. Factorization of Hard Processes in QCD. *Adv.Ser.Direct.High Energy Phys.*, 5:1–91, 1988.

[152] Guido Altarelli and G. Parisi. Asymptotic Freedom in Parton Language. *Nucl.Phys.*, B126:298, 1977.

[153] V.N. Gribov and L.N. Lipatov. Deep inelastic e p scattering in perturbation theory. *Sov.J.Nucl.Phys.*, 15:438–450, 1972.

[154] Yuri L. Dokshitzer. Calculation of the Structure Functions for Deep Inelastic Scattering and e+ e- Annihilation by Perturbation Theory in Quantum Chromodynamics. *Sov.Phys.JETP*, 46:641–653, 1977.

[155] Nestor Armesto. Nuclear shadowing. *J.Phys.*, G32:R367–R394, 2006.

[156] Xin-Nian Wang and Miklos Gyulassy. Gluon shadowing and jet quenching in A + A collisions at s**(1/2) = 200-GeV. *Phys.Rev.Lett.*, 68:1480–1483, 1992.

[157] Shi-yuan Li and Xin-Nian Wang. Gluon shadowing and hadron production at RHIC. *Phys.Lett.*, B527:85–91, 2002.

[158] M. Hirai, S. Kumano, and M. Miyama. Determination of nuclear parton distributions. *Phys.Rev.*, D64:034003, 2001.

[159] K.J. Eskola, V.J. Kolhinen, and P.V. Ruuskanen. Scale evolution of nuclear parton distributions. *Nucl.Phys.*, B535:351–371, 1998.

[160] I. Arsene et al. On the evolution of the nuclear modification factors with rapidity and centrality in d + Au collisions at s(NN)**(1/2) = 200-GeV. *Phys.Rev.Lett.*, 93:242303, 2004.

[161] J.W. Cronin, Henry J. Frisch, M.J. Shochet, J.P. Boymond, R. Mermod, et al. Production of Hadrons with Large Transverse Momentum at 200-GeV, 300-GeV, and 400-GeV. *Phys.Rev.*, D11:3105, 1975.

[162] M. Lev and B. Petersson. NUCLEAR EFFECTS AT LARGE TRANSVERSE MOMENTUM IN A QCD PARTON MODEL. *Z.Phys.*, C21:155, 1983.

[163] J.F. Gunion and G. Bertsch. HADRONIZATION BY COLOR BREMSSTRAHLUNG. *Phys.Rev.*, D25:746, 1982.

[164] Miklos Gyulassy, Ivan Vitev, Xin-Nian Wang, and Ben-Wei Zhang. Jet quenching and radiative energy loss in dense nuclear matter. *Quark Gluon Plasma 3*, pages 123–191, (World Scientific, Singapore), 2004.

[165] R. Baier, D. Schiff, and B.G. Zakharov. Energy loss in perturbative QCD. *Ann.Rev.Nucl.Part.Sci.*, 50:37–69, 2000.

[166] M. Gyulassy, P. Levai, and I. Vitev. Reaction operator approach to nonAbelian energy loss. *Nucl.Phys.*, B594:371–419, 2001.

[167] Markus H. Thoma. Collisional energy loss of high-energy jets in the quark gluon plasma. *Phys.Lett.*, B273:128–132, 1991.

[168] Munshi G. Mustafa and Markus H. Thoma. Quenching of hadron spectra due to the collisional energy loss of partons in the quark gluon plasma. *Acta Phys.Hung.*, A22:93–102, 2005.

[169] Munshi G. Mustafa. Energy loss of charm quarks in the quark-gluon plasma: Collisional versus radiative. *Phys.Rev.*, C72:014905, 2005.

[170] Simon Wicks. Fluctuations with small numbers: Developing the perturbative paradigm for jet physics in the QGP at RHIC and LHC. 2008.

[171] R. Baier, Yuri L. Dokshitzer, S. Peigne, and D. Schiff. Induced gluon radiation in a QCD medium. *Phys.Lett.*, B345:277–286, 1995.

[172] R. Baier, Yuri L. Dokshitzer, Alfred H. Mueller, S. Peigne, and D. Schiff. Radiative energy loss of high-energy quarks and gluons in a finite volume quark - gluon plasma. *Nucl.Phys.*, B483:291–320, 1997.

[173] R. Baier, Yuri L. Dokshitzer, Alfred H. Mueller, S. Peigne, and D. Schiff. Radiative energy loss and p(T) broadening of high-energy partons in nuclei. *Nucl.Phys.*, B484:265–282, 1997.

[174] R. Baier, Yuri L. Dokshitzer, Alfred H. Mueller, and D. Schiff. Radiative energy loss of high-energy partons traversing an expanding QCD plasma. *Phys.Rev.*, C58:1706–1713, 1998.

[175] R. Baier, Yuri L. Dokshitzer, Alfred H. Mueller, and D. Schiff. Quenching of hadron spectra in media. *JHEP*, 0109:033, 2001.

[176] B.G. Zakharov. Fully quantum treatment of the Landau-Pomeranchuk-Migdal effect in QED and QCD. *JETP Lett.*, 63:952–957, 1996.

[177] B.G. Zakharov. Radiative energy loss of high-energy quarks in finite size nuclear matter and quark - gluon plasma. *JETP Lett.*, 65:615–620, 1997.

[178] B.G. Zakharov. Light cone path integral approach to the Landau-Pomeranchuk-Migdal effect. *Phys.Atom.Nucl.*, 61:838–854, 1998.

[179] B.G. Zakharov. Transverse spectra of radiation processes in-medium. *JETP Lett.*, 70:176–182, 1999.

[180] R. Baier, Yuri L. Dokshitzer, Alfred H. Mueller, and D. Schiff. Medium induced radiative energy loss: Equivalence between the BDMPS and Zakharov formalisms. *Nucl.Phys.*, B531:403–425, 1998.

[181] Urs Achim Wiedemann. Gluon radiation off hard quarks in a nuclear environment: Opacity expansion. *Nucl.Phys.*, B588:303–344, 2000.

[182] Carlos A. Salgado and Urs Achim Wiedemann. A Dynamical scaling law for jet tomography. *Phys.Rev.Lett.*, 89:092303, 2002.

[183] Carlos A. Salgado and Urs Achim Wiedemann. Calculating quenching weights. *Phys.Rev.*, D68:014008, 2003.

[184] Miklos Gyulassy and Xin-nian Wang. Multiple collisions and induced gluon Bremsstrahlung in QCD. *Nucl.Phys.*, B420:583–614, 1994.

[185] Miklos Gyulassy, Peter Levai, and Ivan Vitev. Jet quenching in thin quark gluon plasmas. 1. Formalism. *Nucl.Phys.*, B571:197–233, 2000.

[186] M. Gyulassy, P. Levai, and I. Vitev. NonAbelian energy loss at finite opacity. *Phys.Rev.Lett.*, 85:5535–5538, 2000.

[187] Magdalena Djordjevic and Miklos Gyulassy. Heavy quark radiative energy loss in QCD matter. *Nucl.Phys.*, A733:265–298, 2004.

[188] M. Gyulassy, P. Levai, and I. Vitev. Jet tomography of Au+Au reactions including multigluon fluctuations. *Phys.Lett.*, B538:282–288, 2002.

[189] Miklos Gyulassy. Theory of high-energy A+A at RHIC. *Lect.Notes Phys.*, 583:37–79, 2002.

[190] Xiao-feng Guo and Xin-Nian Wang. Multiple scattering, parton energy loss and modified fragmentation functions in deeply inelastic e A scattering. *Phys.Rev.Lett.*, 85:3591–3594, 2000.

[191] Xin-Nian Wang and Xiao-feng Guo. Multiple parton scattering in nuclei: Parton energy loss. *Nucl.Phys.*, A696:788–832, 2001.

[192] A. Majumder, C. Nonaka, and S.A. Bass. Jet modification in three dimensional fluid dynamics at next-to-leading twist. *Phys.Rev.*, C76:041902, 2007.

[193] Peter Brockway Arnold, Guy D. Moore, and Laurence G. Yaffe. Photon and gluon emission in relativistic plasmas. *JHEP*, 0206:030, 2002.

[194] Peter Brockway Arnold, Guy D. Moore, and Laurence G. Yaffe. Effective kinetic theory for high temperature gauge theories. *JHEP*, 0301:030, 2003.

[195] Sangyong Jeon and Guy D. Moore. Energy loss of leading partons in a thermal QCD medium. *Phys.Rev.*, C71:034901, 2005.

[196] Simon Turbide, Charles Gale, Sangyong Jeon, and Guy D. Moore. Energy loss of leading hadrons and direct photon production in evolving quark-gluon plasma. *Phys.Rev.*, C72:014906, 2005.

[197] Guang-You Qin, Jorg Ruppert, Simon Turbide, Charles Gale, Chiho Nonaka, et al. Radiative jet energy loss in a three-dimensional hydrodynamical medium and high pT azimuthal asymmetry of pi0 suppression at mid and forward rapidity in Au+Au collisions at sNN=200 GeV. *Phys.Rev.*, C76:064907, 2007.

[198] Guang-You Qin, Jorg Ruppert, Charles Gale, Sangyong Jeon, Guy D. Moore, et al. Radiative and collisional jet energy loss in the quark-gluon plasma at RHIC. *Phys.Rev.Lett.*, 100:072301, 2008.

[199] David d'Enterria. Jet quenching. 2009.

[200] Urs Achim Wiedemann. Jet Quenching in Heavy Ion Collisions. 2009.

[201] A. Majumder and M. Van Leeuwen. The Theory and Phenomenology of Perturbative QCD Based Jet Quenching. *Prog.Part.Nucl.Phys.*, A66:41–92, 2011.

[202] Nestor Armesto, Brian Cole, Charles Gale, William A. Horowitz, Peter Jacobs, et al. Comparison of Jet Quenching Formalisms for a Quark-Gluon Plasma 'Brick'. *Phys.Rev.*, C86:064904, 2012.

[203] Xin-Nian Wang, Miklos Gyulassy, and Michael Plumer. The LPM effect in QCD and radiative energy loss in a quark gluon plasma. *Phys.Rev.*, D51:3436–3446, 1995.

[204] W.A. Horowitz and B.A. Cole. Systematic theoretical uncertainties in jet quenching due to gluon kinematics. *Phys.Rev.*, C81:024909, 2010.

[205] H. Bethe and W. Heitler. On the Stopping of fast particles and on the creation of positive electrons. *Proc.Roy.Soc.Lond.*, A146:83–112, 1934.

[206] Peter Brockway Arnold. Simple Formula for High-Energy Gluon Bremsstrahlung in a Finite, Expanding Medium. *Phys.Rev.*, D79:065025, 2009.

[207] Alessandro Buzzatti, Andrej Ficnar, and Miklos Gyulassy. Radiative energy loss at intermediate opacity. *unpublished*.

[208] Nestor Armesto, Carlos A. Salgado, and Urs Achim Wiedemann. Medium induced gluon radiation off massive quarks fills the dead cone. *Phys.Rev.*, D69:114003, 2004.

[209] James E. Gentle. Random Number Generation and Monte Carlo Methods. *Springer*, 2003.

[210] George Marsaglia and Wai Wan Tsang. The ziggurat method for generating random variables. *Journal of Statistical Software*, 5(8), 2000.

[211] http://people.sc.fsu.edu/jburkardt/f77src/zigguratopenmp.html.

[212] Magdalena Djordjevic and Ulrich Heinz. Radiative heavy quark energy loss in a dynamical QCD medium. *Phys.Rev.*, C77:024905, 2008.

[213] Magdalena Djordjevic and Ulrich W. Heinz. Radiative energy loss in a finite dynamical QCD medium. *Phys.Rev.Lett.*, 101:022302, 2008.

[214] Magdalena Djordjevic. Theoretical formalism of radiative jet energy loss in a finite size dynamical QCD medium. *Phys.Rev.*, C80:064909, 2009.

[215] Markus H. Thoma and Miklos Gyulassy. QUARK DAMPING AND ENERGY LOSS IN THE HIGH TEMPERATURE QCD. *Nucl.Phys.*, B351:491–506, 1991.

[216] Eric Braaten and Markus H. Thoma. Energy loss of a heavy fermion in a hot plasma. *Phys.Rev.*, D44:1298–1310, 1991.

[217] Eric Braaten and Markus H. Thoma. Energy loss of a heavy quark in the quark - gluon plasma. *Phys.Rev.*, D44:2625–2630, 1991.

[218] B.G. Zakharov. Jet quenching with running coupling including radiative and collisional energy losses. *JETP Lett.*, 88:781–786, 2008.

[219] B.G. Zakharov. Parton energy loss in an expanding quark-gluon plasma: Radiative versus collisional. *JETP Lett.*, 86:444–450, 2007.

[220] Yuri L. Dokshitzer, Valery A. Khoze, and S.I. Troian. Specific features of heavy quark production. LPHD approach to heavy particle spectra. *Phys.Rev.*, D53:89–119, 1996.

[221] O. Kaczmarek, F. Karsch, F. Zantow, and P. Petreczky. Static quark anti-quark free energy and the running coupling at finite temperature. *Phys.Rev.*, D70:074505, 2004.

[222] Richard D. Field. *Applications of perturbative QCD*. Frontiers in physics. Addison-Wesley, The Advanced Book Program, 1989.

[223] W.A. Horowitz and Miklos Gyulassy. The Surprising Transparency of the sQGP at LHC. *Nucl.Phys.*, A872:265–285, 2011.

[224] Stephane Peigne and Andre Peshier. Collisional energy loss of a fast heavy quark in a quark-gluon plasma. *Phys.Rev.*, D77:114017, 2008.

[225] Barbara Betz, Miklos Gyulassy, and Giorgio Torrieri. Fourier Harmonics of High-pT Particles Probing the Fluctuating Intitial Condition Geometries in Heavy-Ion Collisions. *Phys.Rev.*, C84:024913, 2011.

[226] Xin Nian Wang. *Private communication*.

[227] Michelangelo L. Mangano, Paolo Nason, and Giovanni Ridolfi. Heavy quark correlations in hadron collisions at next-to-leading order. *Nucl.Phys.*, B373:295–345, 1992.

[228] Matteo Cacciari, Mario Greco, and Paolo Nason. The P(T) spectrum in heavy flavor hadroproduction. *JHEP*, 9805:007, 1998.

[229] Matteo Cacciari, Stefano Frixione, and Paolo Nason. The p(T) spectrum in heavy flavor photoproduction. *JHEP*, 0103:006, 2001.

[230] P. Nason, S. Dawson, and R. Keith Ellis. The Total Cross-Section for the Production of Heavy Quarks in Hadronic Collisions. *Nucl.Phys.*, B303:607, 1988.

[231] P. Nason, S. Dawson, and R. Keith Ellis. The One Particle Inclusive Differential Cross-Section for Heavy Quark Production in Hadronic Collisions. *Nucl.Phys.*, B327:49–92, 1989.

[232] W. Beenakker, W.L. van Neerven, R. Meng, G.A. Schuler, and J. Smith. QCD corrections to heavy quark production in hadron hadron collisions. *Nucl.Phys.*, B351:507–560, 1991.

[233] Matteo Cacciari and Mario Greco. Large p_T hadroproduction of heavy quarks. *Nucl.Phys.*, B421:530–544, 1994.

[234] Matteo Cacciari, Paolo Nason, and Ramona Vogt. QCD predictions for charm and bottom production at RHIC. *Phys.Rev.Lett.*, 95:122001, 2005.

[235] Azfar Adil and Ivan Vitev. Collisional dissociation of heavy mesons in dense QCD matter. *Phys.Lett.*, B649:139–146, 2007.

[236] Ivan Vitev, Azfar Adil, and Hendrik van Hees. Novel heavy flavor suppression mechanisms in the QGP. *J.Phys.*, G34:S769–774, 2007.

[237] Cheuk-Yin Wong. Heavy quarkonia in quark-gluon plasma. *Phys.Rev.*, C72:034906, 2005.

[238] Bernd A. Kniehl, G. Kramer, and B. Potter. Fragmentation functions for pions, kaons, and protons at next-to-leading order. *Nucl.Phys.*, B582:514–536, 2000.

[239] C. Peterson, D. Schlatter, I. Schmitt, and Peter M. Zerwas. Scaling Violations in Inclusive e+ e- Annihilation Spectra. *Phys.Rev.*, D27:105, 1983.

[240] Magdalena Djordjevic, Miklos Gyulassy, Ramona Vogt, and Simon Wicks. Influence of bottom quark jet quenching on single electron tomography of Au + Au. *Phys.Lett.*, B632:81–86, 2006.

[241] K. Adcox et al. Suppression of hadrons with large transverse momentum in central Au+Au collisions at $\sqrt{s_{NN}} = 130$-GeV. *Phys.Rev.Lett.*, 88:022301, 2002.

[242] C. Adler et al. Centrality dependence of high p_T hadron suppression in Au+Au collisions at $\sqrt{s}_{NN} = 130$-GeV. *Phys.Rev.Lett.*, 89:202301, 2002.

[243] J. Adams et al. Transverse momentum and collision energy dependence of high p(T) hadron suppression in Au+Au collisions at ultrarelativistic energies. *Phys.Rev.Lett.*, 91:172302, 2003.

[244] I. Arsene et al. Transverse momentum spectra in Au+Au and d+Au collisions at s**(1/2) = 200-GeV and the pseudorapidity dependence of high p(T) suppression. *Phys.Rev.Lett.*, 91:072305, 2003.

[245] Xin-Nian Wang. Systematic study of high p_T hadron spectra in pp, p A and A A collisions from SPS to RHIC energies. *Phys.Rev.*, C61:064910, 2000.

[246] Miklos Gyulassy and Michael Plumer. JET QUENCHING IN DENSE MATTER. *Phys.Lett.*, B243:432–438, 1990.

[247] Xin-Nian Wang. Effect of jet quenching on high p_T hadron spectra in high-energy nuclear collisions. *Phys.Rev.*, C58:2321, 1998.

[248] A. Bialas, M. Bleszynski, and W. Czyz. Multiplicity Distributions in Nucleus-Nucleus Collisions at High-Energies. *Nucl.Phys.*, B111:461, 1976.

[249] David G. d'Enterria. Relevance of baseline hard p + p spectra for high-energy nucleus-nucleus physics. *J.Phys.*, G31:S491–S512, 2005.

[250] M.M. Aggarwal et al. Transverse mass distributions of neutral pions from Pb-208 induced reactions at 158-A-GeV. *Eur.Phys.J.*, C23:225–236, 2002.

[251] S.S. Adler et al. Absence of suppression in particle production at large transverse momentum in S(NN)**(1/2) = 200-GeV d + Au collisions. *Phys.Rev.Lett.*, 91:072303, 2003.

[252] B.B. Back et al. Centrality dependence of charged hadron transverse momentum spectra in d + Au collisions at S(NN)**1/2 = 200 GeV. *Phys.Rev.Lett.*, 91:072302, 2003.

[253] Ivan Vitev. Testing the mechanism of QGP-induced energy loss. *Phys.Lett.*, B639:38–45, 2006.

[254] A. Adare et al. Neutral pion production with respect to centrality and reaction plane in Au+Au collisions at $\sqrt{s_{NN}}$=200 GeV. 2012.

[255] K.J. Eskola, H. Honkanen, C.A. Salgado, and U.A. Wiedemann. The Fragility of high-p(T) hadron spectra as a hard probe. *Nucl.Phys.*, A747:511–529, 2005.

[256] A. Dainese, C. Loizides, and G. Paic. Leading-particle suppression in high energy nucleus-nucleus collisions. *Eur.Phys.J.*, C38:461–474, 2005.

[257] Thorsten Renk, Jorg Ruppert, Chiho Nonaka, and Steffen A. Bass. Jet-quenching in a 3D hydrodynamic medium. *Phys.Rev.*, C75:031902, 2007.

[258] R. Baier. Jet quenching. *Nucl.Phys.*, A715:209–218, 2003.

[259] S.S. Adler et al. Nuclear modification of electron spectra and implications for heavy quark energy loss in Au+Au collisions at s(NN)**(1/2) - 200-GeV. *Phys.Rev.Lett.*, 96:032301, 2006.

[260] B.I. Abelev et al. Erratum: Transverse momentum and centrality dependence of high-p(T) non-photonic electron suppression in Au+Au collisions at $\sqrt{s_{NN}} = 200$ GeV. *Phys.Rev.Lett.*, 98:192301, 2007.

[261] A. Adare et al. Measurement of high-p(T) single electrons from heavy-flavor decays in p+p collisions at s**(1/2) = 200-GeV. *Phys.Rev.Lett.*, 97:252002, 2006.

[262] J. Bielcik. Centrality dependence of heavy flavor production from single electron measurement in s(NN)**(1/2) = 200-GeV Au + Au collisions. *Nucl.Phys.*, A774:697–700, 2006.

[263] A. Adare et al. Energy Loss and Flow of Heavy Quarks in Au+Au Collisions at s(NN)**(1/2) = 200-GeV. *Phys.Rev.Lett.*, 98:172301, 2007.

[264] M. Gyulassy. Getting to the bottom of the heavy quark jet puzzle. *Physics*, 2:107, Dec 2009.

[265] Yuri L. Dokshitzer and D.E. Kharzeev. Heavy quark colorimetry of QCD matter. *Phys.Lett.*, B519:199–206, 2001.

[266] P. Aurenche and B.G. Zakharov. Anomalous mass dependence of radiative quark energy loss in a finite-size quark-gluon plasma. *JETP Lett.*, 90:237–243, 2009.

[267] K. Aamodt et al. Suppression of Charged Particle Production at Large Transverse Momentum in Central Pb–Pb Collisions at $\sqrt{s_{NN}} = 2.76$ TeV. *Phys.Lett.*, B696:30–39, 2011.

[268] Jacek Otwinowski. Charged Particle Production at Large Transverse Momentum in Pb−Pb Collisions at $\sqrt{s_{NN}} = 2.76$ TeV Measured with ALICE at the LHC. *J.Phys.*, G38:124112, 2011.

[269] Betty Abelev et al. Centrality Dependence of Charged Particle Production at Large Transverse Momentum in Pb–Pb Collisions at $\sqrt{s_{\rm NN}} =$ 2.76 TeV. *Phys.Lett.B*, 2012.

[270] Report No. CMS-PAS-HIN-10-005. Nuclear modification factor for charged particle production at high pt in pbpb collisions at sqrt(snn)=2.76 tev. 2011.

[271] (ed.) Armesto, N., (ed.) Borghini, N., (ed.) Jeon, S., (ed.) Wiedemann, U.A., S. Abreu, et al. Heavy Ion Collisions at the LHC - Last Call for Predictions. *J.Phys.*, G35:054001, 2008.

[272] Serguei Chatrchyan et al. Dependence on pseudorapidity and centrality of charged hadron production in PbPb collisions at a nucleon-nucleon centre-of-mass energy of 2.76 TeV. *JHEP*, 1108:141, 2011.

[273] Georges Aad et al. Measurement of the centrality dependence of the charged particle pseudorapidity distribution in lead-lead collisions at $\sqrt{s_{NN}} = 2.76$ TeV with the ATLAS detector. *Phys.Lett.*, B710:363–382, 2012.

[274] Xiao-Fang Chen, Tetsufumi Hirano, Enke Wang, Xin-Nian Wang, and Hanzhong Zhang. Suppression of high p_T hadrons in $Pb+Pb$ Collisions at LHC. *Phys.Rev.*, C84:034902, 2011.

[275] B.G. Zakharov. Variation of jet quenching from RHIC to LHC and thermal suppression of QCD coupling constant. *JETP Lett.*, 93:683–687, 2011.

[276] Barbara Betz and Miklos Gyulassy. Examining a reduced jet-medium coupling in Pb+Pb collisions at the Large Hadron Collider. *Phys.Rev.*, C86:024903, 2012.

[277] Betty Abelev et al. Suppression of high transverse momentum D mesons in central Pb-Pb collisions at $\sqrt{s_{NN}} = 2.76$ TeV. *JHEP*, 1209:112, 2012.

[278] M. Gyulassy, I. Vitev, and X.N. Wang. High p(T) azimuthal asymmetry in noncentral A+A at RHIC. *Phys.Rev.Lett.*, 86:2537–2540, 2001.

[279] W.A. Horowitz and M. Gyulassy. Quenching and Tomography from RHIC to LHC. *J.Phys.*, G38:124114, 2011.

[280] Denes Molnar and Deke Sun. Realistic medium-averaging in radiative energy loss. 2012.

[281] Miklos Gyulassy, Ivan Vitev, Xin-Nian Wang, and Pasi Huovinen. Transverse expansion and high p(T) azimuthal asymmetry at RHIC. *Phys.Lett.*, B526:301–308, 2002.

[282] Juan Martin Maldacena. The Large N limit of superconformal field theories and supergravity. *Adv.Theor.Math.Phys.*, 2:231–252, 1998.

[283] S.S. Gubser, Igor R. Klebanov, and Alexander M. Polyakov. Gauge theory correlators from noncritical string theory. *Phys.Lett.*, B428:105–114, 1998.

[284] Edward Witten. Anti-de Sitter space and holography. *Adv.Theor.Math.Phys.*, 2:253–291, 1998.

[285] Steven S. Gubser. Drag force in AdS/CFT. *Phys.Rev.*, D74:126005, 2006.

[286] C.P. Herzog, A. Karch, P. Kovtun, C. Kozcaz, and L.G. Yaffe. Energy loss of a heavy quark moving through N=4 supersymmetric Yang-Mills plasma. *JHEP*, 0607:013, 2006.

[287] Paul M. Chesler, Kristan Jensen, Andreas Karch, and Laurence G. Yaffe. Light quark energy loss in strongly-coupled N = 4 supersymmetric Yang-Mills plasma. *Phys.Rev.*, D79:125015, 2009.

[288] Steven S. Gubser, Daniel R. Gulotta, Silviu S. Pufu, and Fabio D. Rocha. Gluon energy loss in the gauge-string duality. *JHEP*, 0810:052, 2008.

[289] Jorge Noronha, Miklos Gyulassy, and Giorgio Torrieri. Conformal Holography of Bulk Elliptic Flow and Heavy Quark Quenching in Relativistic Heavy Ion Collisions. *Phys.Rev.*, C82:054903, 2010.

[290] Andrej Ficnar. AdS/CFT Energy Loss in Time-Dependent String Configurations. *Phys.Rev.*, D86:046010, 2012.

[291] Andrej Ficnar, Jorge Noronha, and Miklos Gyulassy. Falling Strings and Light Quark Jet Quenching at LHC. 2012.

[292] Jinfeng Liao and Edward Shuryak. Strongly coupled plasma with electric and magnetic charges. *Phys.Rev.*, C75:054907, 2007.

[293] Jinfeng Liao and Edward Shuryak. Magnetic Component of Quark-Gluon Plasma is also a Liquid! *Phys.Rev.Lett.*, 101:162302, 2008.

[294] Jinfeng Liao and Edward Shuryak. Angular Dependence of Jet Quenching Indicates Its Strong Enhancement Near the QCD Phase Transition. *Phys.Rev.Lett.*, 102:202302, 2009.